Quantum Corrals on Cu(111): Tailoring Electronic Lifetimes and Characterizing the Decay Lengths of Interatomic Forces



Dissertation zur Erlangung des Doktorgrades der Naturwissenschaften (Dr. rer. nat.) der Fakultät für Physik der Universität Regensburg

vorgelegt von

Marco Weiß

aus Schwandorf

im Jahr 2026

Das Promotionsgesuch wurde am 21.04.2026 eingereicht.
Die Arbeit wurde von Prof. Dr. Franz Josef Giessibl angeleitet.

Prüfungsausschuss:

Vorsitzender:	apl. Prof. Dr. Juan Diego Urbina
Erstgutachter:	Prof. Dr. Franz Josef Giessibl
Zweitgutachter:	Prof. Dr. Isabella Gierz
weiterer Prüfer:	Prof. Dr. Jörg Wunderlich

Contents

1. Introduction **1**

2. Fundamentals of atomic force and scanning tunneling microscopy **5**

2.1. Frequency-modulation atomic force microscopy 5

2.2. Scanning tunneling microscopy 8

2.2.1. The tunneling current and its variables 8

2.2.2. Scanning tunneling spectroscopy 10

2.3. Application of simultaneous atomic force and scanning tunneling microscopy 13

2.3.1. Imaging modes 14

2.3.2. Determination of the tip-sample distance 15

3. Fundamentals of the quantum corral **17**

3.1. The Shockley surface state 17

3.2. Quantum corral 18

3.2.1. Building a quantum corral 20

3.2.2. Hard wall model 21

3.2.3. Connection to STM and AFM measurements 23

3.2.4. From hard wall model to experimental spectra 25

4. Sample and tip preparation **27**

4.1. Sample preparation 27

4.2. Tip preparation 29

4.2.1. Tips for scanning tunneling spectroscopy measurements . . . 30

4.2.2. Tips for atomic force microscopy measurements 31

5. Tailoring electronic lifetimes of corral states **35**

5.1. Spectral line shape analysis 35

5.1.1. General analysis 36

5.1.2. Details and quality assessment of the analysis 42

5.2. The spectral width in a single parameter – average path length . . . 47
5.3. Variation of the wall density . . . 50
5.4. Discussion . . . 56
5.4.1. Relating spectral width and wall density . . . 56
5.4.2. Gaussian spectral line shape . . . 58
5.5. Summary and Outlook . . . 62

6. Characterizing the decay lengths of interatomic forces 65
6.1. AFM measurements inside quantum corrals . . . 65
6.1.1. Constant-height AFM images and the total surface charge density . . . 66
6.1.2. Distance dependence of attractive and repulsive interactions 70
6.2. Model descriptions of tip-corral interactions . . . 76
6.2.1. Model description of Pauli repulsion for CO-tips . . . 77
6.2.2. Model description of chemical attraction for metal-tips . . . 80
6.2.3. Estimated Pauli repulsion for metal-tips and validation of the model . . . 82
6.3. Decay length ratios and the Morse potential . . . 85
6.4. Comparison of a quantum corral to a natural atom . . . 88
6.5. Summary and Outlook . . . 92

7. General conclusions and perspective 95
7.1. Decoupling lifetime, confinement, and interaction range . . . 96
7.2. Towards designer interactions . . . 97
7.3. Concluding remarks . . . 98

A. Appendix 101

List of Publications 127

Bibliography 129

Acknowledgments 149

1. Introduction

The ability to arrange and manipulate matter at the atomic scale is one of the central achievements of modern nanoscience. Direct control over individual atoms and molecules on surfaces became possible through the development of scanning probe microscopy, most prominently scanning tunneling microscopy (STM) and atomic force microscopy (AFM). In STM, a sharp metallic tip is scanned across a conducting surface while measuring the tunneling current, providing access to the electronic structure of the sample. AFM, in contrast, measures the force between the probe tip and the surface, making it possible to directly investigate tip-sample interactions. A landmark demonstration of atomic manipulation was the construction of the "IBM" logo from individual Xe atoms on a Ni surface by Eigler and Schweizer [1]. Since then, atomic manipulation has evolved into a powerful approach for creating artificial structures with designed electronic properties. This has enabled the exploration of fundamental quantum states within Dirac systems, such as artificial graphene [2] and Lieb lattices [3, 4], as well as structures exhibiting nontrivial topological behavior [5–7]. Beyond these fundamental studies, atomic manipulation has also been successfully directed toward practical applications, ranging from the control and readout of spin states in engineered atomic structures [8–10] to the implementation of logic operations [11, 12] and ultra-dense, atomic-scale data storage [13, 14].

Quantum corrals are one particularly important class of such human-built structures. A quantum corral typically has a size of a few nanometers and is formed by arranging atoms or molecules on a surface such that surface-state electrons are laterally confined. The first quantum corral, built by Crommie *et al.* [15] from 48 individual Fe adatoms on Cu(111), had a radius of 7.13 nm and revealed standing wave patterns of the Shockley surface state within the circular boundary. In this system, the corral wall acts as a scattering boundary for the quasi-free two-dimensional electron gas present at the Cu(111) surface. The lateral confinement gives rise to a set of corral resonances with characteristic energies, finite spectral widths, and distinct spatial patterns within the corral.

Kastner introduced the term artificial atom for systems in which electrons are

confined to a small region and exhibit discrete electronic states [16]. Quantum corrals on noble metal surfaces such as Cu(111) realize this concept by laterally confining the Shockley surface state into discrete corral resonances. However, the discretization of electronic states is only one aspect of the artificial atom analogy. Natural atoms also interact with their environment via attractive and repulsive forces, for example through chemical bonding and Pauli repulsion. Recent AFM experiments have shown that quantum corrals exhibit such atom-like interaction properties as well: Confined Shockley surface states can interact attractively with metal-terminated tips and repulsively with CO-terminated tips [17]. This extends the artificial atom analogy beyond the existence of discrete electronic states, because the confined states also give rise to measurable force interactions with an atomic-scale probe.

At the same time, quantum corrals are not simply enlarged versions of natural atoms. In a natural atom, electronic states are formed via the attractive potential of the nucleus, with electron-electron interactions further shaping the resulting orbital structure. In a quantum corral, by contrast, the relevant electronic states are not atomic orbitals formed by a central nuclear potential. Instead, they result from the lateral confinement of the Cu(111) Shockley surface state by a corral wall made from individually positioned surface adsorbates. Both systems localize electronic states, but the confinement is realized in different ways. Together with their nanometer size, this boundary-defined confinement makes quantum corrals particularly useful as artificial atoms, because the confining boundary can be engineered directly by changing the arrangement, density, or chemical identity of the wall atoms or molecules.

These considerations lead to the central question of this thesis: How do confined surface state electrons in quantum corrals interact with their surrounding environment? This question is approached from two complementary directions. The first follows the confined states along the surface, where scattering at the corral wall, lateral transmission, and coupling into bulk states each play a central role in determining their lifetime and, consequently, their spectral width. By modifying the corral size and wall density, these electronic lifetimes can be tailored via the confining boundary. The second direction follows their decay into the vacuum, where the spatial extent of the wave function governs the force interaction between the artificial atom and the atom or molecule at the AFM tip apex.

The first of these directions concerns the lifetime of confined electronic states, which is a key property of artificial quantum structures. It describes how long an electron remains in a given corral state before it is scattered out of it, transmitted through the wall, or coupled to other states. Experimentally, this lifetime is reflected in the spectral widths and corresponding line shapes measured by scanning tunneling spectroscopy. In natural atoms, electronically excited states often decay exponentially with time, resulting in Lorentzian spectral line shapes. Similar Lorentzian line shapes are commonly used to describe resonances in other types of artificial atoms such as quantum dots [16, 18–20]. For the quantum corrals studied in this thesis, the observed spectral widths cannot be attributed to a single mechanism. The lifetime of a corral state can be limited by intrinsic scattering processes, such as electron-electron and electron-phonon scattering, but also by the interaction of the confined electrons with the corral wall [21–23]. The wall can transmit electrons, reflect them, couple them to bulk states [24], and may also contribute to spectral broadening via the motion of the adsorbates.

Understanding these lifetime-limiting mechanisms is essential for creating artificial quantum structures with engineered properties. For example, long-lived confined states are desirable for applications in quantum sensing, quantum information processing, as well as artificial quantum simulators [25–28]. More fundamentally, the spectral width of a corral state provides direct information about how strongly the artificial atom is coupled to its environment along the surface. In this thesis, the lifetimes of quantum corral states are investigated by scanning tunneling spectroscopy. By analyzing the energy distributions of individual corral states in corrals of different sizes and wall densities, the role of the corral boundary in limiting the lifetime of confined surface-state electrons is examined.

The second direction concerns the distance dependence of the force acting between quantum corral states and an AFM probe. While scanning tunneling microscopy probes the electronic structure via the tunneling current, AFM measures the force between tip and sample. In this case, the external probe is the front atom or molecule at the AFM tip apex. Previous AFM measurements on quantum corrals demonstrated that confined Shockley surface states can interact with AFM tips on the femtonewton scale [17]. CO-terminated tips were found to probe a repulsive interaction, attributed to Pauli repulsion, while metal-terminated tips revealed an attractive interaction, interpreted as chemical attraction [17].

In this thesis, the force interaction between the artificial atom formed by the quantum corral and the atom or molecule at the AFM tip apex can therefore be regarded as an interatomic force, and its spatial decay length is investigated. The measurements show that the attractive interaction measured with a metal-terminated tip has a larger characteristic decay length than the repulsive interaction measured with a CO-terminated tip. This qualitative behavior resembles the interaction between natural atoms, where chemical attraction is generally longer ranged than Pauli repulsion. However, the absolute decay lengths measured in quantum corrals are significantly larger than those known from natural atom-atom interactions. This difference reflects the electronic structure of the artificial atom: The occupied corral states originate from the Shockley surface state and span only a narrow energy window near the Fermi level, while natural atoms contain deeper, more localized orbitals that contribute shorter-ranged components to the interaction.
Together, these two approaches characterize quantum corrals as artificial atoms whose electronic lifetimes and interatomic force interactions can be investigated experimentally.
This thesis is organized as follows. Chapter 2 introduces the principles of frequency-modulation atomic force microscopy, scanning tunneling microscopy, and scanning tunneling spectroscopy, and discusses the advantages and challenges associated with simultaneous STM/AFM operation. Chapter 3 explains the fundamentals of quantum corrals, including the Shockley surface state on Cu(111), the construction of quantum corrals, the hard wall model, and the connection between corral states and STM/AFM measurements. Chapter 4 describes the preparation of the Cu(111) sample, the preparation of metal- and CO-terminated tips, and the experimental conditions used throughout this work. The first experimental part of this thesis is presented in Chapter 5, focusing on the spectral line shapes, spectral widths, and lifetimes of quantum corral states, as well as their dependence on corral size and wall density. Chapter 6 presents the second experimental part, in which the decay lengths of attractive and repulsive interatomic forces between quantum corral states and AFM tips are measured and discussed. Finally, Chapter 7 summarizes the central conclusions and discusses the broader perspective of quantum corrals as artificial quantum systems in which confinement, lifetime, and interaction with external probes can be studied in a controlled way.

2. Fundamentals of atomic force and scanning tunneling microscopy

This thesis is based on experiments performed using a combined scanning tunneling microscope and frequency-modulation atomic force microscope, which simultaneously provides access to the tunneling current I and the frequency shift Δf. These two signals probe complementary properties of the system: While scanning tunneling microscopy and the closely related technique of scanning tunneling spectroscopy can provide information about the electronic structure of the surface, atomic force microscopy gives access to the tip-sample interaction.
This chapter introduces the fundamental principles of frequency-modulation atomic force microscopy in Section 2.1 and scanning tunneling microscopy in Section 2.2, with particular focus on scanning tunneling spectroscopy in Subsection 2.2.2. The focus is placed on those aspects that are directly relevant for this work, in particular the relation between the measured signals and the underlying physical quantities such as the local density of states and the tip-sample force. Section 2.3 will then address the simultaneous operation of atomic force and scanning tunneling microscopy, discussing various imaging modes in Subsection 2.3.1 and explaining the determination of the tip-sample distance in Subsection 2.3.2.

2.1. Frequency-modulation atomic force microscopy

Atomic force microscopy (AFM)[1] was introduced in 1986 by Binnig, Quate, and Gerber [29]. Based on the forces acting between a sharp probe tip and a surface, AFM is able to measure images with atomic and even subatomic resolution [30–32]. The basic configuration of an AFM consists of a sharp tip attached to a cantilever, which acts as a force sensor.
In contrast to scanning tunneling microscopy, AFM does not rely on measuring an electrical current and can therefore also be used on insulating surfaces. Due to its

[1] In this work, the abbreviation AFM refers both to the method of atomic force microscopy and to the atomic force microscope itself.

wider range of applications, AFM has become an established tool in fields ranging from surface science to industrial applications.

The general principles of AFM have been described in various publications and books [33–38]. The section follows Ref. [34] and provides a brief overview of the concepts relevant to this thesis. Since all AFM measurements presented in this work were performed in the frequency-modulation mode (FM-AFM) [39], only this mode of operation is discussed in more detail.

In FM-AFM, the cantilever (with the attached tip) is driven to oscillate at a constant amplitude A at its resonance frequency. In the absence of tip-sample interaction (free oscillation), the resonance frequency is given by

$$f_0 = \frac{1}{2\pi}\sqrt{\frac{k}{m^*}}, \tag{2.1}$$

where k is the stiffness and m^* the effective mass of the cantilever [34].

When the tip is brought closer to the surface, a distance-dependent force $F_{\mathrm{ts}}(z)$ acts between tip and sample. The corresponding tip-sample force gradient is given by $k_{\mathrm{ts}}(z) = -\partial F_{\mathrm{ts}}(z)/\partial z$. For very small oscillation amplitudes A, the force gradient changes negligibly over the trajectory of one oscillation cycle and can therefore be approximated as constant. Under this gradient approximation, the tip-sample interaction can be treated as an additional spring, such that the effective spring constant is given by $k_{\mathrm{eff}} = k + k_{\mathrm{ts}}$. This modified spring constant shifts the resonance frequency of the cantilever from f_0 to f. For weak tip-sample interactions, the resulting frequency shift $\Delta f = f - f_0$ can be expressed as [34]

$$\Delta f(z) = \frac{f_0}{2k} k_{\mathrm{ts}}(z) = -\frac{f_0}{2k}\frac{\partial F_{\mathrm{ts}}(z)}{\partial z}. \tag{2.2}$$

This relation shows that, within the gradient approximation, the frequency shift Δf is directly related to the force gradient rather than the force itself. In typical experiments, the condition of a constant force gradient over the range of an oscillation cycle is usually not met. For arbitrary oscillation amplitudes, the general expression for the frequency shift is given by [40, 41]

$$\Delta f(z) = \frac{f_0}{2k}\frac{2}{\pi A^2}\int_{-A}^{A} F_{\mathrm{ts}}(z + A - q)\frac{q}{\sqrt{A^2 - q^2}}\,\mathrm{d}q. \tag{2.3}$$

Equation (2.3) shows that the measured frequency shift corresponds to a convolution of the tip-sample force with the weighting function $q/\sqrt{A^2 - q^2}$.

If the tip-sample force follows an exponential distance dependence, $F_{\mathrm{ts}}(z) = F_0 \exp(-z/\lambda)$, Eq. (2.3) simplifies to [35]

$$\Delta f(z) = \frac{f_0}{kA} F_0 \exp\left(-\frac{z+A}{\lambda}\right) \cdot J_1\left(\frac{A}{\lambda}\right), \tag{2.4}$$

where J_1 denotes the Bessel function of the first kind. This shows that an exponential force-distance dependence leads to an exponential frequency shift with the same decay length λ. Conversely, if a measured $\Delta f(z)$ curve is well described by an exponential function over the measured distance range, the corresponding tip-sample force follows the same exponential distance dependence. The measured frequency shift curve is therefore first fitted with an exponential function to determine the decay length λ, and this fitted representation is then used to obtain the corresponding force:

$$F_{\mathrm{ts}}(z) = \frac{kA}{f_0} \cdot \frac{\exp\left(\frac{A}{\lambda}\right)}{J_1\left(\frac{A}{\lambda}\right)} \cdot \Delta f(z). \tag{2.5}$$

Equation (2.5) is used in Chapter 6 to determine the corresponding force-distance curves from exponential fits to the measured $\Delta f(z)$ curves. In this work, the oscillation amplitude A was kept constant at $A = 50\,\mathrm{pm}$. The signal-to-noise ratio is best when the oscillation amplitude corresponds to the decay length of the interaction [42]. For the systems investigated here, the relevant decay lengths are on the order of 50 pm (see Chapter 6).

While AFM provides information about the interaction between tip and sample, scanning tunneling microscopy offers complementary insight into the electronic structure of the system. In the following section, the fundamental principles of scanning tunneling microscopy and scanning tunneling spectroscopy are introduced.

2.2. Scanning tunneling microscopy

In 1982, four years before the AFM was introduced, Binnig *et al.* presented the scanning tunneling microscope (STM)[1] [43]. Owing to its ability to resolve electrically conducting surfaces with atomic resolution, the STM has become one of the most important instruments in surface science.
This section introduces the fundamental physical principles of STM, with an emphasis on the concepts relevant for this thesis. More detailed descriptions of the underlying physics, operational aspects, and technical implementations can be found in the books by Chen [44] and Wiesendanger [45]. The summary given here follows the main concepts presented in Ref. [44].

2.2.1. The tunneling current and its variables

The fundamental mechanism underlying STM is the concept of quantum tunneling: Quantum mechanics allows electrons to tunnel through a potential barrier even when classical mechanics forbids it. In STM, a sharp metallic tip is positioned a few hundred picometers above a conducting surface. The tip-sample distance is small enough that electrons can tunnel across the vacuum gap. When a bias voltage is applied between tip and sample, this tunneling results in a measurable current, even though the two electrodes remain spatially separated.
The high spatial resolution of STM arises from the exponential distance dependence of the tunneling current, which can be captured by a simple one-dimensional model. For this, the vacuum gap between tip and sample is modeled as a potential barrier of width z, corresponding to the tip-sample separation. The effective barrier height Φ is approximated by $\Phi = (\Phi_\mathrm{T} + \Phi_\mathrm{S})/2$, where Φ_T and Φ_S are the work functions of tip and sample, respectively [46].
Classically, an electron with an energy less than Φ cannot overcome the potential barrier. However, solving the Schrödinger equation for this situation reveals a finite probability for an electron to be found inside or even beyond the barrier. For small bias voltages $eV \ll \Phi$, the tunneling current as a function of distance is given by

$$I_\mathrm{t}(z) = I_0 \exp(-2\kappa z) \quad \text{with} \quad \kappa = \sqrt{2m_\mathrm{e}\Phi}/\hbar. \tag{2.6}$$

[1] In this work, the abbreviation STM refers both to the method of scanning tunneling microscopy and to the scanning tunneling microscope itself.

Here, I_0 denotes the current at $z = 0$, m_e is the electron mass, e the elementary charge[1], and κ the decay constant [44]. For copper, which has a work function of $\Phi_S = 4.94\,\mathrm{eV}$ for the (111) plane [47], one obtains[2] $\kappa \approx 10\,\mathrm{nm}^{-1}$. Thus, decreasing the tip-sample distance by only 100 pm increases the tunneling current by approximately one order of magnitude.

Although this simple model is very successful in capturing the strong distance dependence of the tunneling current, it fails to include other important dependencies. A more complete description follows Bardeen's tunneling approach [48], which accounts for the energy-dependent electronic states of tip and sample as well as the applied bias voltage. Expressed in terms of the corresponding densities of states, the tunneling current can be written as [44]

$$I(V) \propto \int_{-\infty}^{\infty} \rho_S(E_F + eV + \epsilon)\rho_T(E_F + \epsilon)\Big[f(E_F + eV + \epsilon) - f(E_F + \epsilon)\Big]|M|^2 \,\mathrm{d}\epsilon, \quad (2.7)$$

where $f(E) = [1 + \exp(E/k_B T)]^{-1}$ is the Fermi-Dirac distribution and E_F is the Fermi energy. The sample density of states below the tip is ρ_S and the tip density of states is ρ_T. The bias voltage V is applied to the sample. The tunneling matrix element M describes the overlap between the participating tip and sample states and determines the tunneling probability.

In the limit of low temperatures and assuming an energy-independent tunneling matrix element [48], Eq. (2.7) simplifies to the widely used STM expression [44]

$$I(V) \propto \int_{0}^{-eV} \rho_S(E_F + eV + \epsilon)\rho_T(E_F + \epsilon) \,\mathrm{d}\epsilon. \quad (2.8)$$

Equation (2.8) shows that the tunneling current is proportional to the convolution of the local density of states of the sample and the tip over the energy window defined by the applied bias voltage.

[1] In this work, the elementary charge is defined to be positive.
[2] It was assumed here that the work functions of tip and sample are the same: $\Phi_S = \Phi_T = \Phi$.

2.2.2. Scanning tunneling spectroscopy

A central technique employed in this work (primarily in Chapter 5) is scanning tunneling spectroscopy (STS), which is closely related to the fundamental principles of STM. In contrast to topographic imaging, which provides information about height variations of the surface, STS is primarily used to probe the electronic structure of the sample.

As discussed in Subsection 2.2.1, the tunneling current depends on the electronic density of states of the sample and the tip [see Eq. (2.8)]. If the density of states of the tip can be assumed to be constant, which is experimentally achievable (see Section 4.2), then taking the derivative of Eq. (2.8) with respect to the bias voltage yields [44]

$$\frac{\mathrm{d}I}{\mathrm{d}V} \propto \rho_{\mathrm{S}}(E_{\mathrm{F}} + eV). \tag{2.9}$$

Thus, the differential conductance ($\mathrm{d}I/\mathrm{d}V$) is proportional to the local density of states of the sample below the tip position. The electronic structure of the sample can therefore be probed by sweeping the bias voltage and recording an $I(V)$ curve. The derivative may be obtained numerically, or more commonly, via a lock-in detection technique. Alternatively, $\mathrm{d}I/\mathrm{d}V$ images can be measured to spatially resolve the local density of states of the sample.

Influence of the lock-in measurement technique

Numerically differentiating a measured $I(V)$ curve amplifies noise and generally leads to a reduced signal-to-noise ratio in the resulting $\mathrm{d}I/\mathrm{d}V$ spectrum. For this reason, a lock-in method is used in most STS measurements, including this work. With this technique, the bias voltage is modulated by a small sinusoidal voltage with amplitude V_{mod}. This leads to a modulation of the detected tunneling current with the same frequency.

The lock-in amplifier acts as a band-pass filter and extracts the amplitude of the current modulation at the reference frequency. The signal obtained in this way is referred to as the $\mathrm{d}I/\mathrm{d}V$ signal, which is proportional to the voltage derivative of the current signal [49].

Using a lock-in significantly improves the signal-to-noise ratio, but it also introduces broadening of spectroscopic features along the energy axis. If the intrinsic width

of the features is much larger than eV_{mod}, the broadening is negligible [50]. If not, the measured differential conductance no longer reflects the local density of states directly, but rather a broadened version of it. Within this framework, the lock-in measurement can be described as a convolution of the sample density of states ρ_{S} with a modulation-broadening kernel χ_{mod} [50]:

$$\frac{\mathrm{d}I}{\mathrm{d}V} \propto (\rho_{\mathrm{S}} * \chi_{\mathrm{mod}})(V) = \int_{-V_{\mathrm{mod}}}^{V_{\mathrm{mod}}} \rho_{\mathrm{S}}\Big(E_{\mathrm{F}} + e(V+\epsilon)\Big) \underbrace{\frac{2}{\pi V_{\mathrm{mod}}}\sqrt{V_{\mathrm{mod}}^2 - \epsilon^2}}_{\chi_{\mathrm{mod}}} \,\mathrm{d}\epsilon. \quad (2.10)$$

The modulation-broadening kernel χ_{mod} is a semicircle with a diameter of $2eV_{\mathrm{mod}}$. For all measurements presented in Chapter 5, a modulation amplitude of $V_{\mathrm{mod}} = 5\,\mathrm{mV}$ was used. The spectral features investigated in the quantum corrals exhibit typical widths of approximately 50 meV. Although modulation-broadening is therefore not a dominant contribution, it must be taken into account for a quantitative line shape analysis.

Influence of finite temperatures

Since the measurements presented in this work were performed at a temperature of $T \approx 5.7\,\mathrm{K}$, the temperature-dependent smearing of the electron occupation of the tip and sample, i.e., the broadening of the Fermi-Dirac distribution, is not neglected. In the following, this effect is referred to as Fermi-broadening.
Taking a finite temperature into account, the tunneling current is no longer determined by the density of states at a single energy, as in Eq. (2.9), but by an energy-weighted integral over the sample density of states. Starting from Eq. (2.7) and differentiating with respect to the bias voltage, the influence of a finite temperature on the differential conductance can be expressed as [50]

$$\frac{\mathrm{d}I}{\mathrm{d}V} \propto \int_{-\infty}^{\infty} \rho_{\mathrm{S}}\Big(E_{\mathrm{F}} + eV + \epsilon\Big) \underbrace{\frac{\exp\Big((E_{\mathrm{F}}+\epsilon)/k_{\mathrm{B}}T\Big)}{\Big[1 + \exp\Big((E_{\mathrm{F}}+\epsilon)/k_{\mathrm{B}}T\Big)\Big]^2}}_{\approx G_{\mathrm{Fermi}}} \,\mathrm{d}\epsilon. \quad (2.11)$$

Equation (2.11) represents the exact mathematical expression for the temperature-induced broadening of spectroscopic features and shows that the measured differential

conductance corresponds to a convolution of the sample density of states with a kernel given by the derivative of the Fermi-Dirac distribution. For practical purposes, this thermal broadening kernel can be very well approximated by a Gaussian function [50]. With this approximation, Eq. (2.11) can be written as

$$\frac{\mathrm{d}I}{\mathrm{d}V} \propto \int_{-\infty}^{\infty} \rho_{\mathrm{S}}\big(E_{\mathrm{F}} + eV + \epsilon\big) \underbrace{\frac{1}{4} \exp\left(-\frac{1}{2}\frac{(E_{\mathrm{F}}+\epsilon)^2}{\sigma_{\mathrm{Fermi}}^2}\right)}_{G_{\mathrm{Fermi}}} \mathrm{d}\epsilon = (\rho_{\mathrm{S}} * G_{\mathrm{Fermi}})(V). \quad (2.12)$$

The Gaussian approximation is introduced here as a deliberate simplification for the subsequent quantitative analysis of spectroscopic line shapes. While the exact thermal broadening kernel in Eq. (2.11) is known analytically, its replacement by the Gaussian function G_{Fermi} greatly simplifies numerical convolution, reduces computational overhead, and minimizes potential sources of systematic error in the fitting procedure. In addition, the Gaussian form allows different broadening mechanisms of similar shape to be combined in a transparent and intuitive way, which will be discussed in more detail below.

The width parameter σ_{Fermi} is related to the full width at half maximum (FWHM) of the Gaussian by $\Gamma_{\mathrm{Fermi}} = 2\sqrt{2\ln 2}\,\sigma_{\mathrm{Fermi}}$. From the exact expression in Eq. (2.11), the temperature-induced energy broadening is given by $\Gamma_{\mathrm{Fermi}} \approx 3.5\,k_{\mathrm{B}}T$. At room temperature ($T \approx 300\,\mathrm{K}$), this results in an energy broadening of $\Gamma_{\mathrm{Fermi}}^{300\,\mathrm{K}} \approx 90\,\mathrm{meV}$. At the base temperature of the microscope used in this work ($T \approx 5.7\,\mathrm{K}$), the corresponding thermal broadening is reduced to $\Gamma_{\mathrm{Fermi}}^{5.7\,\mathrm{K}} \approx 2\,\mathrm{meV}$.

Radio frequency noise

In addition to modulation- and Fermi-broadening, fluctuations of the applied bias voltage caused by radio frequency (RF) noise [51–54] also contribute to the broadening of measured spectroscopic features. One important source of such noise is, for example, Johnson noise [55], originating from the thermal motion of charge carriers in electrical circuits [54]. In low-temperature STM and AFM setups, the microscope head operated at cryogenic temperatures is electrically connected to room-temperature electronics via wiring, which introduces RF noise from the 300 K environment [54].

These RF disturbances do not directly affect the detection of the tunneling current.

Instead, they effectively smear out the applied bias voltage, resulting in an additional energy broadening of measured spectroscopic features [54].
Analogous to modulation and temperature broadening, the influence of RF noise on the measured differential conductance can be described by a convolution of the sample density of states ρ_S with an RF-broadening kernel G_{RF}:

$$\frac{dI}{dV} \propto (\rho_S * G_{RF})(V). \tag{2.13}$$

The RF-broadening kernel G_{RF} is given by a Gaussian function [56–58], characterized by a FWHM of $\Gamma_{RF} \approx 9\,\text{meV}$ as determined experimentally in a comparable low-temperature STM system [54].

Combined spectral broadening

Since all spectral broadening mechanisms have to be taken into account for a high-precision line shape analysis of spectral features, the total broadening can be combined mathematically as follows [50]:

$$\frac{dI}{dV} \propto (\rho_S * \chi_{mod} * \underbrace{G_{Fermi} * G_{RF}}_{G_{Fermi,RF}})(V). \tag{2.14}$$

Since both Fermi- and RF-broadening lead to a Gaussian-shaped broadening of spectral features, they can be combined into a single broadening function $G_{Fermi,RF}$[1]. Together, these two mechanisms result in a Gaussian broadening of spectroscopic peaks with a full width at half maximum of $\Gamma_{Fermi,RF} = \sqrt{(\Gamma_{Fermi})^2 + (\Gamma_{RF})^2} = \sqrt{(2\,\text{meV})^2 + (9\,\text{meV})^2} \approx 9.2\,\text{meV}$.

2.3. Application of simultaneous atomic force and scanning tunneling microscopy

The microscope used in this work is based on a qPlus sensor [59], which enables the simultaneous detection of the AFM signal and the tunneling current. This allows atomic force microscopy and scanning tunneling microscopy to be operated within

[1]The convolution of two Gaussian functions is again a Gaussian function: $G_{Fermi} * G_{RF} = G_{Fermi,RF}$.

the same experimental setup and, if desired, at the same time. In the following, the imaging modes used in this thesis are described in Subsection 2.3.1 and the determination of the tip-sample distance is explained in Subsection 2.3.2.

2.3.1. Imaging modes

Constant-Current Mode

Due to its monotonic dependence on the tip-sample separation, the tunneling current $I(z)$ serves as a reliable feedback parameter [44]. In constant-current mode, a feedback loop continuously adjusts the tip-sample distance to maintain a current setpoint. Throughout this thesis, the terms constant-current mode and STM feedback mode are used interchangeably for this mode of operation, in which the STM feedback loop keeps the tunneling current at the chosen setpoint.
By scanning the tip laterally while recording the vertical displacement required to keep the current constant, a topographic image $z(x, y)$ is obtained. However, since the tunneling current depends not only on the distance but also on the local density of states (LDOS), STM images generally contain both geometric (e.g., a step edge) and electronic contributions.
As a result, apparent height variations in STM images must be interpreted with care, as they may reflect changes in the LDOS rather than true topography.
In simultaneous AFM measurements, the feedback-induced changes in tip-sample distance also affect the frequency shift signal. For example, if the tip moves closer to the surface in response to a locally reduced density of states, the magnitude of the attractive force gradient increases, leading to a more negative frequency shift [32].

Constant-Height Mode

In constant-height mode, the feedback loop is disabled and the tip is scanned laterally at a fixed vertical position ($z = \text{const.}$). This allows the tunneling current $I(x, y)$ and the frequency shift $\Delta f(x, y)$ to be measured independently of feedback-induced distance changes. In this mode, variations in Δf directly reflect changes in the tip-sample interaction.
As discussed in Section 2.2.2, the differential conductance $\mathrm{d}I/\mathrm{d}V$ is proportional to the local density of states of the sample at the energy defined by the applied bias

voltage. In contrast, the tunneling current I is, to first approximation, proportional to the integral of the LDOS over the energy window between the Fermi level and the applied bias voltage [see Eq. (2.8)]. Consequently, spatial variations in the tunneling current do not directly correspond to LDOS variations at a specific energy. The current-based tip-distance control in constant-current mode therefore couples to the measured $\mathrm{d}I/\mathrm{d}V$ signal. Constant-height measurements avoid this coupling, allowing spatially resolved $\mathrm{d}I/\mathrm{d}V$ maps to directly reflect the spatial variation of the LDOS. This effect is particularly relevant for the interpretation of spatially resolved $\mathrm{d}I/\mathrm{d}V$ data. However, constant-height measurements require sufficiently flat surfaces and a stable tip-sample separation throughout the scan, because surface protrusions or uncontrolled changes in the relative tip-sample position increase the risk of a tip crash.

Throughout this thesis, all AFM measurements and spatially resolved $\mathrm{d}I/\mathrm{d}V$ images were acquired in constant-height mode.

In combined STM/AFM measurements using a qPlus sensor, crosstalk between the tunneling current and the cantilever oscillation can occur. The tunneling current flowing through the sensor electrodes can excite or damp the oscillation [60], thereby influencing the AFM measurement. Since this crosstalk depends linearly on the tunneling current [60], all AFM measurements in this work were performed at a bias voltage of 0 mV.

2.3.2. Determination of the tip-sample distance

Although the measurements in this thesis, especially in Chapter 6, could be described using a purely relative tip-sample distance scale, it is more instructive to relate them to an estimated absolute tip-sample distance. The distance determination based on the tunneling current is briefly outlined, following Ref. [61].

In a qPlus-based setup, the tip oscillates with a constant amplitude A, causing a periodic modulation of the tip-sample distance and, consequently, of the tunneling current. The measured current corresponds to the time-averaged tunneling current over one oscillation cycle and is given by [34]

$$\langle I(z_{\mathrm{PC}})\rangle = I_0 \exp(-2\kappa z_{\mathrm{PC}}) \exp(-2\kappa A) \mathfrak{T}_0^{\mathrm{Bessel}}(2\kappa A), \tag{2.15}$$

where $\mathfrak{T}_0^{\text{Bessel}}$ is the modified Bessel function of the first kind (zeroth order), and z_{PC} denotes the distance of the lower turning point of the oscillation relative to point contact. Using the conductance at point contact $G_0 = I_0/V$, Eq. (2.15) can be rewritten as

$$z_{\text{PC}}(\langle I\rangle, V, A) = -\frac{1}{2\kappa}\ln\left(\frac{\langle I\rangle}{G_0 V}\frac{\exp(2\kappa A)}{\mathfrak{T}_0^{\text{Bessel}}(2\kappa A)}\right), \tag{2.16}$$

which provides the distance of the lower turning point of the oscillation relative to point contact. For monoatomic metal-tips[1], the conductance at point contact is $G_0 = 2e^2/h = (12\,906\,\Omega)^{-1}$ [37, 62], where e is the elementary charge and h is the Planck constant. For a CO-terminated tip[2], $G_0^{\text{CO}} = (404\,497\,\Omega)^{-1}$ [63], which was determined experimentally.

To obtain an intuitive measure, the tip-sample distance is defined as the core-core distance between the frontmost atom of the tip and the atoms in the first surface layer. This distance is greater than the distance at point contact by the two radii of the respective atoms. The covalent radius of a copper atom is $r_{\text{Cu}} = 132\,\text{pm}$ and for an oxygen atom it is $r_{\text{O}} = 66\,\text{pm}$ [64]. Measurements by Huber [32] showed that the point-contact conductance is reached 48 pm before the covalent radii of tip and sample touch. This offset holds for both a metal-tip and a CO-terminated tip and has to be taken into account. For a copper-terminated tip, the distance is given by

$$z_{\text{metal}} = z_{\text{PC}} + 2r_{\text{Cu}} + 48\,\text{pm} = z_{\text{PC}} + 312\,\text{pm}, \tag{2.17}$$

while for a CO-terminated tip it becomes

$$z_{\text{CO}} = z_{\text{PC}} + r_{\text{Cu}} + r_{\text{O}} + 48\,\text{pm} = z_{\text{PC}} + 246\,\text{pm}. \tag{2.18}$$

Using typical experimental parameters ($\kappa = 10^{10}\,\text{m}^{-1}$, $V = 10\,\text{mV}$, $\langle I\rangle = 100\,\text{pA}$), this yields approximate distances of $z_{\text{metal}} = 555\,\text{pm}$ and $z_{\text{CO}} = 444\,\text{pm}$.

For notational simplicity, the measured tunneling current is denoted as I throughout this thesis, although it formally corresponds to the time-averaged current $\langle I\rangle$ defined in Eq. (2.15).

[1] A monoatomic metal-tip ends in a single metal atom at the tip apex.
[2] A CO-terminated tip is a monoatomic metal-tip with a single CO attached at the tip apex.

3. Fundamentals of the quantum corral

This chapter summarizes the physical concepts underlying the quantum corrals investigated in this work. It first introduces the Shockley surface state on Cu(111) in Section 3.1, which forms the electronic basis of the confined states. Section 3.2 then describes the construction of CO-based quantum corrals, followed by the introduction of the hard wall model as a simple framework to understand their eigenstates and energy spectrum. Finally, this chapter concludes with a discussion of the relationship between this idealized description and the experimentally observed spectroscopic behavior.

3.1. The Shockley surface state

At the surface of a metal, the periodic potential of the crystal is interrupted and the translational symmetry that exists in the bulk is broken. Electrons that would otherwise propagate through the lattice can no longer propagate freely in the direction normal to the surface. As a consequence, new electronic states can form that are bound to the surface and decay exponentially into both the crystal and the vacuum. These are known as Shockley surface states [65].

On Cu(111), such a surface state appears close to the Fermi level, within the Γ-L projected bulk band gap [15, 47, 66, 67]. In contrast to bulk states, the surface-localized wave functions of the Shockley surface state are confined perpendicular to the surface but remain free to move parallel to it. This confinement in the z-direction gives rise to a quasi-free two-dimensional (2D) electron gas on the surface.

This two-dimensional electron gas is highly sensitive to scattering from steps, defects, and surface adsorbates [15, 68]. Such scattering leads to standing wave patterns that can be directly visualized by scanning tunneling microscopy, which provides the physical basis for the quantum confinement effects in corrals.

The Shockley surface state on Cu(111) is a two-dimensional electron gas with a

nearly free-electron-like dispersion that follows a parabolic relation [15, 69]:

$$E(k_{||}) = E_{\mathrm{BE}} + \frac{\hbar^2 k_{||}^2}{2m_{\mathrm{e}}^*}. \tag{3.1}$$

Here, $k_{||}$ is the magnitude of the in-plane wave vector, E_{BE} the onset (band edge) of the surface state, and m_{e}^* the effective electron mass. For Cu(111), the onset energy lies 440 meV below the Fermi level and the effective mass is $m_{\mathrm{e}}^* = (0.405 \pm 0.025) \cdot m_{\mathrm{e}}$, with m_{e} being the mass of a free electron [15, 47, 69–73].
Because of its two-dimensional character, the Shockley surface state exhibits a step-like density of states at E_{BE} [50, 74, 75]. For a tip with a flat density of states (see Section 4.2), this step can be observed in $\mathrm{d}I/\mathrm{d}V$ spectra recorded on bare Cu(111). Due to its otherwise featureless density of states, the Shockley surface state provides a convenient reference in spectroscopic measurements (see Section 4.2).
The surface-state wave function decays exponentially into both the bulk and the vacuum. For $z > 0$ (towards the vacuum), it is described by [17]

$$\psi_z(z) \propto \exp\left(-\frac{z}{\lambda_{\mathrm{S}}^{\psi}}\right), \tag{3.2}$$

where $\lambda_{\mathrm{S}}^{\psi}$ is the decay length. The decay length is determined by the energy difference between E_{BE} and the vacuum level, which is $\Phi + 440\,\mathrm{meV} = 5.38\,\mathrm{eV}$, where $\Phi = 4.94\,\mathrm{eV}$ is the work function of Cu(111) [47]. This yields [17]

$$\lambda_{\mathrm{S}}^{\psi} = \sqrt{\frac{\hbar^2}{2m_{\mathrm{e}}(\Phi + 440\,\mathrm{meV})}} = 84\,\mathrm{pm}. \tag{3.3}$$

Towards the vacuum, the corresponding electron density ($\rho \propto |\psi|^2$) decays with half this length, $\lambda_{\mathrm{S}}^{\rho} = \lambda_{\mathrm{S}}^{\psi}/2 = 42\,\mathrm{pm}$ [17].

3.2. Quantum corral

Around the mid-1970s, the first conclusive experimental measurements confirming the existence of the Shockley surface state were reported using angle-resolved photoemission spectroscopy (ARPES) [47]. Years later, with the advent of the scanning tunneling microscope, the first spatially resolved images of the Shockley

surface state were obtained (e.g., Refs. [76, 77]). These early STM studies also suggested that the surface state is reflected at substrate step edges [76]. Davis *et al.* later developed the theoretical description and predicted standing wave patterns at such step edges [78].

A few years later, in 1993, Crommie *et al.* [15] and Hasegawa *et al.* [68] independently reported standing wave patterns on Cu(111) and Au(111), from which they extracted the dispersion relation of the Shockley surface state using the wavelength of the interference pattern. Crommie *et al.* also observed a standing wave pattern around point defects. Building on these insights, Crommie, Lutz, and Eigler [79] used atomic manipulation [1] to construct the first quantum corral. In their experiment, 48 individual Fe adatoms on Cu(111) were arranged in a circle with a radius of 7.13 nm.

This geometry effectively confined the two-dimensional electron gas in the xy-plane, resulting in a set of resonant eigenstates inside the corral. Consequently, in $\mathrm{d}I/\mathrm{d}V$ spectroscopy measurements, these resonant eigenstates appear as peak-like features, highlighting the effectively zero-dimensional nature of these corral states. The corresponding standing wave patterns were investigated using STM imaging and scanning tunneling spectroscopy. Despite the groundbreaking demonstration of confining an electron gas within a human-made atomic structure, the use of Fe adatoms as the corral wall had a major drawback. During $\mathrm{d}I/\mathrm{d}V$ spectroscopy, approximately 20% of the wall atoms were observed to move [79]. This bias-induced rearrangement changed the corral geometry, preventing a detailed and stable spectroscopic characterization of the confined states. Nevertheless, the Fe corral of Crommie *et al.* [79] clearly exhibited discrete energy levels.

The movement of Fe atoms during these measurements can be attributed to the weak bonding of Fe on Cu(111). On Cu(111), a lateral force of (27 ± 6) pN is sufficient to manipulate Fe adatoms [80]. Using a more stable wall material than Fe allows the investigation of corral states far from the Fermi level and enables detailed studies of their spectral widths and line shapes. For carbon monoxide (CO) on Cu(111), a lateral force of (160 ± 30) pN is required to move a molecule, which is roughly six times as large as the force required for Fe [81]. Spectroscopic measurements of other CO-based structures show the desired voltage stability (e.g., Refs. [2, 3, 82, 83]) and therefore allow for a detailed analysis of the corral's energy levels.

3.2.1. Building a quantum corral

In this work, circular and square quantum corrals are realized on Cu(111) using CO molecules as the confining boundary. Chapter 5 presents circular corrals with radii of 7.13 nm and 3.57 nm, while Chapter 6 focuses on square corrals with side lengths of $L_x = 6.13$ nm and $L_y = 6.20$ nm. For both geometries, the wall density ρ_{wall} (the number of CO molecules forming the boundary divided by the circumference of the structure) was systematically varied to study its effect on the electronic structure and the measured forces. The geometric shape and size of the constructed corrals define the confinement discussed in the hard wall description below.

The construction procedure of quantum corrals, described in detail in Ref. [84], is summarized here. First, a flat and defect-free region of the Cu(111) surface must be located, since most defects scatter the corral states. Such regions are identified using STM imaging. Typical imaging parameters of 10 mV sample bias and 10 pA are sufficient to detect most defects. An example of a suitable area is the central region of the image shown in Fig. 3.1(a). The procedure to obtain a defect-free Cu(111) surface is described in detail in Chapter 4.

Once an appropriate site is found, CO molecules from the surrounding area are gathered via lateral atomic manipulation [85]. To move a CO, the tip is positioned over a suitable molecule in STM feedback mode at 1 mV and a tunneling current setpoint between 1 nA and 2 nA (depending on the exact tip geometry). At this small tip-sample distance, attractive forces allow the CO molecule to be dragged along the surface. After positioning the tip with the CO molecule beneath it at the desired site, the tip is retracted by lowering the tunneling current setpoint. The most precise manipulation is achieved with monoatomic metal-tips. The gathering procedure is illustrated in Figs. 3.1(b) and (c), where 27 and 47 CO molecules, respectively, were arranged in an approximate circle.

After collecting all required CO molecules, they are positioned according to a predefined construction plan. Because CO on Cu(111) adsorbs exclusively on top of Cu surface atoms, the target geometry can be realized with atomic precision. Details about the adsorption site of CO on Cu(111) are given in Chapter 4. Construction plans for all corrals constructed in this work are provided in Appendix A.1 and will be described in more detail in Chapters 5 and 6. Figure 3.1(d) shows a completed circular CO corral with a radius of 7.13 nm comprising 48 molecules.

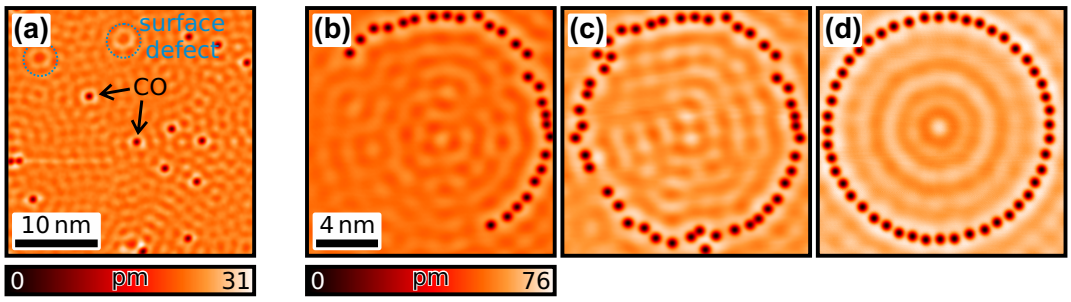


Figure 3.1: (a): STM feedback image of a clean Cu(111) region with adsorbed CO molecules. Two surface defects are visible at the top of the image. Imaging parameters: $V = -10\,\mathrm{mV}$, $I = 10\,\mathrm{pA}$. The corral was built in the central area of this region. (b) to (d): STM images illustrating the construction of a CO corral. All images share the same color scale. Imaging parameters: $V = -1\,\mathrm{mV}$, $I = 100\,\mathrm{pA}$. (b): Arrangement of 27 CO molecules in an approximately circular shape. (c): Arrangement of 47 CO molecules in an approximately circular shape. (d): Fully assembled circular corral with a radius of 7.13 nm consisting of 48 precisely positioned CO molecules. For all images (a) to (d), the lowest point of the color scale is set to zero.

Inside the finished structure, STM images reveal standing wave patterns originating from the confined Shockley surface state. These patterns reflect the discrete eigenstates of the quantum corral system. Their spatial structure and energetic positions can be understood within the hard wall model introduced in the following subsection.

3.2.2. Hard wall model

To describe the behavior of the confined Shockley surface state inside a quantum corral, a simple model of a particle in a two-dimensional box can be used. An infinitely high potential in the surface plane captures the essential features of a corral, such as the spatial shape of the eigenstates and their approximate energetic positions [17, 79]. This approach is often referred to as the *hard wall model*.

In this work, two corral geometries were investigated: circular and square. The spectroscopic properties of the circular corrals are discussed in Chapter 5, and the force between an AFM tip and the confined states in square corrals is analyzed in Chapter 6.

Below, the basic hard wall description for both geometries is briefly summarized. More detailed derivations can be found in the supplemental material of Ref. [17].

Circular quantum corral

Solving the Schrödinger equation for a cylindrical potential well gives the in-plane wave functions [17, 79]:

$$\Psi_{n,l}(r,\phi) = \psi_{n,l}(r) \cdot \psi_l(\phi), \tag{3.4}$$

where n is the main quantum number and l is the angular momentum quantum number. Here $n \in \mathbb{N}$ and $l \in \mathbb{Z}$. The radial distance from the center of the corral is given by r and ϕ denotes the azimuthal angle.

The angular part of the wave function is

$$\psi_l(\phi) \propto \exp(\mathrm{i}l\phi). \tag{3.5}$$

The radial component of the wave function is

$$\psi_{n,l}(r) \propto J_l\left(r\frac{r_{n,l}}{R_\mathrm{C}}\right), \tag{3.6}$$

where $r_{n,l}$ is the n-th zero of the Bessel function J_l of the first kind and order l. The radius of the corral is R_C, which is 7.13 nm and 3.57 nm for the circular corrals investigated in Chapter 5.

The z-component of the Shockley surface state is not affected by the lateral confining potential and decays exponentially into the vacuum [17]. It is therefore still described by $\psi_z(z) \propto \exp(-z/\lambda_\mathrm{S}^\psi)$ [see Eq. (3.2) in Section 3.1]. Each corral state is therefore characterized by the quantum numbers n and l.

The discrete eigenenergies of the circular corral relative to the Fermi level are

$$E_{n,l}^\mathrm{circ} = \frac{\hbar^2 r_{n,l}^2}{2m_\mathrm{e}^* R_\mathrm{C}^2} - 440\,\mathrm{meV}. \tag{3.7}$$

This expression demonstrates that for every combination of n and l, the corresponding corral state $\Psi_{n,l}$ is located at a specific energy. Equation (3.7) also shows that the corral states $\Psi_{n,+l}$ and $\Psi_{n,-l}$ are degenerate. The resulting energy spectra for circular corrals with radii of 7.13 nm and 3.57 nm are presented in Fig. 3.2(a).

Square-shaped quantum corral

Solving the Schrödinger equation for a rectangular quantum well in the surface plane yields sinusoidal wave functions in both the x and y directions:

$$\Psi_{n_x,n_y}(x,y) \propto \sin\left(\frac{\pi n_x x}{L_x}\right) \cdot \sin\left(\frac{\pi n_y y}{L_y}\right), \tag{3.8}$$

where Ψ_{n_x,n_y} is characterized by the quantum numbers n_x and n_y, with n_x, $n_y \in \mathbb{N}$. For the square corrals analyzed in Chapter 6, the side lengths are $L_x = 6.13\,\text{nm}$ and $L_y = 6.20\,\text{nm}$. The eigenenergies of the square corral relative to the Fermi energy are given by

$$E^{\text{square}}_{n_\text{x},n_\text{y}} = \frac{\hbar^2\pi^2}{2m^*_\text{e}}\left(\frac{n_x^2}{L_x^2} + \frac{n_y^2}{L_y^2}\right) - 440\,\text{meV}. \tag{3.9}$$

The corresponding energy spectrum is displayed in Fig. 3.2(b).

3.2.3. Connection to STM and AFM measurements

To relate the hard wall model to experimentally accessible quantities, the connection between the calculated eigenstates and the measured signals in STM and AFM must be considered. For clarity, the expressions below are written for the geometries mainly used in the corresponding measurements in this thesis, namely circular corrals for STM and square corrals for AFM, but the same relations apply analogously to other corral geometries.

In STM measurements, the tunneling current is proportional to the local surface charge density below the tip position, integrated over the energy interval between 0 and eV, where zero is defined as the Fermi energy. Within the framework of the hard wall model, the lateral variation of the tunneling current can therefore be expressed as a linear combination of all states that fall into this energy window [17, 79]

$$I \propto \sum_{E^{\text{circ}}_{n,l} \in [0,eV]} \left|\Psi_{n,l}\right|^2. \tag{3.10}$$

This relation connects the discrete eigenstates of the corral to the standing wave patterns observed in STM measurements.

In AFM measurements, the interaction between the tip and the confined surface

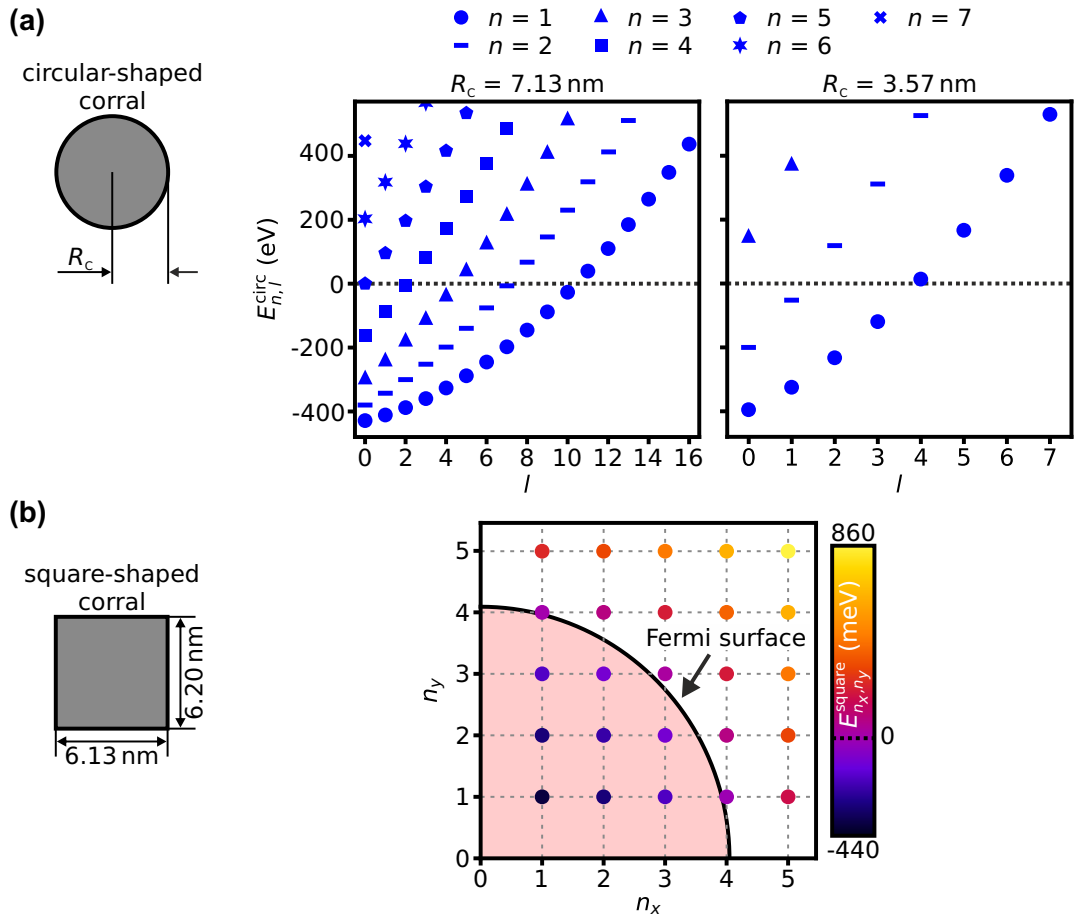


Figure 3.2: (a): Energy spectra according to the hard wall model of two circular-shaped quantum corrals with different sizes. Every marker represents the eigenenergy of a corral state, characterized by the main quantum number n and the angular momentum quantum number l. The energies are relative to the Fermi energy, which is marked with a black dashed line. (b): Model spectrum of the square-shaped corral in n-space, characterized by the main quantum numbers n_x and n_y. Corral states below the Fermi level (within the red shaded region) are occupied by electrons. The color of the marker represents the energy $E^{\text{square}}_{n_x,n_y}$ of the corresponding state. The lowest energy in the color code is defined by the onset of the Shockley surface state (-440 meV), while the maximum is given by the state with the quantum numbers $n_x = n_y = 5$. The energy scale is given with respect to the Fermi energy, which is marked by the black dashed line in the color bar.

state is governed by the total surface charge density. As shown by Stilp *et al.* [17], the measured forces scale with the total charge density σ_{tot}, which is given by the sum over all occupied corral states

$$\sigma_{\mathrm{tot}} \propto \sum_{E^{\mathrm{square}}_{n_x,n_y} \leq 0} \left| \Psi_{n_x,n_y} \right|^2. \tag{3.11}$$

Metal-terminated tips exhibit stronger attraction toward regions of increased σ_{tot}, whereas CO-terminated tips experience repulsive forces in regions with enhanced charge density. This repulsive interaction was attributed to Pauli repulsion [17].

3.2.4. From hard wall model to experimental spectra

Within the hard wall model, the confined electron states are characterized by discrete eigenenergies. Because the confining potential is assumed to be infinitely high, the electrons remain perfectly confined inside the potential well. In this idealized framework, each corral state therefore has an infinite lifetime and is represented spectroscopically by a delta-like peak at its corresponding energy.

In reality, the experimentally observed spectral features of a quantum corral exhibit a finite linewidth, as already demonstrated in the measurements by Crommie *et al.* [79]. This finite width reflects the finite lifetime of the confined corral states via the energy-time uncertainty principle. A more realistic confining potential that accounts for finite wall height and spatial extent would already lead to a spectroscopically finite width of the corral states, reflecting the fact that electrons are only partially confined and can leak out of the corral boundary.

In general, for the free Shockley surface state, several mechanisms can influence the lifetime of electrons, including electron-electron, electron-phonon, and electron-defect scattering (e.g., Refs. [21–23, 86–96]). Both electron-electron and electron-phonon scattering provide a temporally constant and spatially homogeneous scattering background for surface-state electrons [23, 87]. This leads to an exponentially decreasing survival probability in the time domain, which corresponds to a characteristic Lorentzian line shape in the energy domain [95].

Electron-defect scattering can also reduce the lifetime of surface-state electrons via several channels, for example by coupling to bulk states or through inelastic scattering processes (e.g., Refs. [22, 79, 95, 97]). For randomly distributed defects,

this type of scattering is commonly treated as a Lorentzian lifetime broadening [95]. In a quantum corral, electron-defect scattering corresponds to scattering at the corral wall (CO molecules). In contrast to a stochastic defect distribution, the defects forming the corral wall are arranged in a well-defined, non-random geometry. This ordered boundary not only gives rise to the usual defect-related loss channels, but also introduces an additional loss mechanism due to lateral transmission through the wall.

For the corrals studied in this thesis, particularly in Chapter 5, interactions of the confined electrons with the corral wall provide the dominant lifetime-limiting contribution. A more detailed discussion of the relevant loss channels and the resulting spectral line shape is given in Chapter 5, especially in Section 5.2 and Subsection 5.4.2.

Despite these limitations, the hard wall model provides an accurate description of the spatial structure and approximate energy positions of the corral states. A quantitative description of the experimentally observed spectra therefore requires extending the hard wall model to account for finite lifetimes and spectral broadening. The implementation of such an extended description and its comparison with experimental data are discussed in detail in Section 5.1.

4. Sample and tip preparation

4.1. Sample preparation

All measurements presented in this work were performed on a Cu(111) surface. Since copper is electrically conductive, simultaneous STM and AFM measurements can be carried out. To obtain an atomically flat and clean Cu(111) surface, several sputtering and annealing cycles were performed [98]. Each preparation cycle starts with sputtering the copper sample using Ar^+ ions. Argon gas is introduced into the preparation chamber through a leak valve until a pressure of approximately 2×10^{-6} mbar is reached. The Ar atoms are ionized and accelerated to a kinetic energy of 1.2 keV, and the sample is sputtered for 20 min, during which a sputter current of roughly 6 µA is measured. This treatment removes contaminants as well as several atomic layers of the copper crystal, leaving a rough surface [99, 100]. After closing the Ar valve and evacuating the remaining gas, the sample is annealed at $\approx$ 570 °C for 20 min. During annealing, the surface restructures itself and forms atomically flat terraces with typical sizes of several hundred nm^2. Since the Cu(111) sample had already been in use for several years and had undergone multiple preparations in the past, two to three sputtering and annealing cycles were sufficient per experimental session. This preparation process takes place in a chamber within the system designed specifically for this purpose, known as the preparation chamber. A detailed description of the microscope and its design can be found in Refs. [101, 102].

Tip preparation, tip characterization, and the construction of artificial quantum structures on the surface require carbon monoxide molecules on the clean Cu(111) surface. For this purpose, the freshly prepared sample is transferred into the microscope head, which is located in the so-called analysis chamber, and then cooled down to approximately 4.5 K. Because the microscope head is mechanically coupled to the helium cryostat during this step, the temperature is slightly lower than during normal (decoupled) operation ($\approx$ 5.7 K). After opening the gate valve between the analysis and preparation chambers and opening the cryostat's thermal shields,

CO gas is introduced into the preparation chamber until a constant pressure of $\approx 3 \times 10^{-9}$ mbar is reached in the analysis chamber. The thermal shields and the CO valve remain open for about 2 min.
Individual CO molecules adsorb on the Cu(111) surface as well as on other cold surfaces, such as the microscope head and cryostat. Experience shows that the CO dosing behavior depends strongly on how long the microscope has been kept at low temperature and how often CO was dosed during that time period. Because the microscope head and cryostat are made of copper and stainless steel, most CO molecules have desorbed by the time the system returns to room temperature. When CO is first introduced after the microscope has been freshly cooled down, many molecules adsorb onto the cryostat and microscope head, leaving only a small fraction to reach the sample. In this case, the dosing time must often be increased to about 3 min, sometimes requiring two consecutive dosing steps. After the microscope has remained cold for several months and has undergone many CO dosing cycles, the cold surfaces become saturated with CO, and the dosing time can be reduced to about 1.5 min. In rare cases, after roughly a year of continuous low temperature operation and multiple CO dosing steps, no active CO dosing is necessary. The thermal energy of the room-temperature sample and friction during insertion are sufficient to transfer CO from the microscope head onto the sample surface.
A coverage of roughly 20 CO molecules per 100 nm^2 was found to be most practical. Since CO-based quantum corrals were constructed in the course of this thesis, each consisting of 12 to 96 individually positioned CO molecules, a relatively high coverage was desirable. At the same time, enough free surface area must remain available to assemble the corrals, which are approximately 15 nm in diameter. While nanostructures can also be built at lower coverages, it is essential to ensure that a sufficient number of CO molecules are available on a single Cu terrace.
Figure 4.1(a) shows an STM image of CO molecules adsorbed on a clean Cu(111) surface. Individual molecules appear as dark spots when imaged with a metallic tip at low bias voltages. Their adsorption locally modifies the surface electron density, leading to a reduced density of states at the adsorption site [103]. As a result, the tunneling current decreases above the CO molecules, forcing the STM tip to approach the surface to maintain a constant current. In Fig. 4.1(a), three additional surface defects of unknown origin (marked in blue) are visible.
As discussed in Section 3.1, the Cu(111) surface hosts a quasi-free, two-dimensional

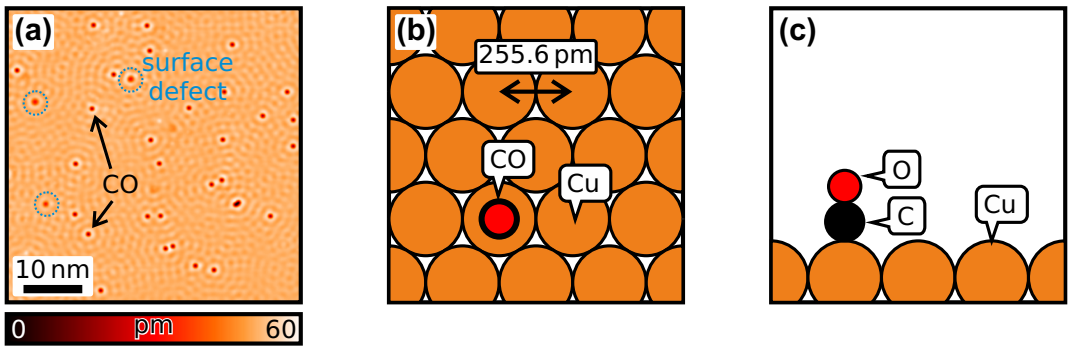


Figure 4.1: (a): STM feedback image of a clean Cu(111) surface with adsorbed CO molecules appearing as dark spots. Three additional surface defects (highlighted by blue circles) are also visible. Imaging parameters: $V = -10\,\mathrm{mV}$, $I = 10\,\mathrm{pA}$. Scattering of the Shockley surface state at CO molecules and defects leads to the observed standing wave pattern. (b): Schematic top view of the Cu(111) surface with a CO molecule adsorbed on top of a Cu atom. The nearest-neighbor distance between Cu atoms is 255.6 pm. (c): Schematic side view of the Cu(111) surface with an adsorbed CO molecule. CO binds perpendicular to the surface with the carbon atom pointing towards the sample.

electron gas near the Fermi level, namely the Shockley surface state [65]. Scattering of this state at CO molecules, other adsorbates, defects, or step edges produces the characteristic standing wave pattern observed on the bare Cu(111) surface [15]; see, e.g., Fig. 4.1(a). Such scattering also leads to the confined standing wave patterns inside quantum corrals, a concept that was discussed in detail in Chapter 3.
Individual CO molecules adsorb perpendicular to the surface, on top of copper atoms, with the carbon atom pointing downward towards the surface [104, 105]. Schematic illustrations of this adsorption geometry are shown in Fig. 4.1(b) and (c). Copper crystallizes in a face-centered cubic (fcc) structure with a lattice constant of $a_0 = 361.5\,\mathrm{pm}$ [106]. In the (111) plane, this results in a hexagonal lattice with a nearest-neighbor distance of $d_{\mathrm{nn}} = a_0/\sqrt{2} = 255.6\,\mathrm{pm}$. The distance between two copper atoms on the Cu(111) surface is indicated in Fig. 4.1(b).

4.2. Tip preparation

Depending on the type of measurement, the tip must meet specific requirements. In general, a sharp tip is essential for high-resolution imaging, such as in STM, AFM, or spatially resolved STS measurements. For AFM, achieving optimal spatial resolution

requires a monoatomic tip apex, that is, an apex terminating in a single atom. This prevents image blurring caused by multiple atoms at the apex and improves reproducibility by enhancing sensitivity to short-range, atom-specific interactions while reducing long-range contributions. For STM and STS measurements, a sharp tip likewise improves spatial resolution. However, especially for STS, an additional condition must be fulfilled: The density of states of the tip should be flat. As shown in Eq. (2.8), the tunneling current, and consequently its derivative ($\mathrm{d}I/\mathrm{d}V$), depends on the density of states of both the sample and the tip. Only for a flat tip DOS does the measured tunneling spectrum reflect the electronic structure of the sample.

The qPlus sensor used in this work was equipped with an electrochemically etched tungsten wire, yielding an already sharp tip [107]. To further sharpen the tip on a microscopic level and to remove the non-conducting oxide layer formed during and after etching, field emission cleaning was performed [44].

Regardless of the desired tip property, microscopic shaping of the tip apex is achieved through controlled indentations of the tip into the clean Cu(111) surface, commonly referred to as poking [107]. This process allows for fine-tuning of the tip properties until the desired behavior (see the following subsections) is reached.

4.2.1. Tips for scanning tunneling spectroscopy measurements

For STS measurements, the microscopic tip engineering described above is used to primarily fine-tune the electronic properties of the tip. The sharpness of the tip usually remains stable once achieved. Shallow pokes ($\approx 700\,\mathrm{pm}$ deep) only slightly affect the geometric apex structure. The density of states of the tip is more sensitive and can change significantly even after small pokes.

To verify that the tip DOS is sufficiently flat, test measurements are performed on the bare Cu(111) surface. As explained in Section 3.1, the unconfined Shockley surface state of Cu(111) produces an almost flat DOS, except for a small step at about $-440\,\mathrm{mV}$, marking the onset of the surface state. Therefore, any additional features or corrugations in the measured $\mathrm{d}I/\mathrm{d}V$ spectrum must originate from the tip itself.

If such unwanted features are observed [see Fig. 4.2(a)], the tip DOS has to be altered by a shallow poke. The tip DOS is repeatedly checked and refined until

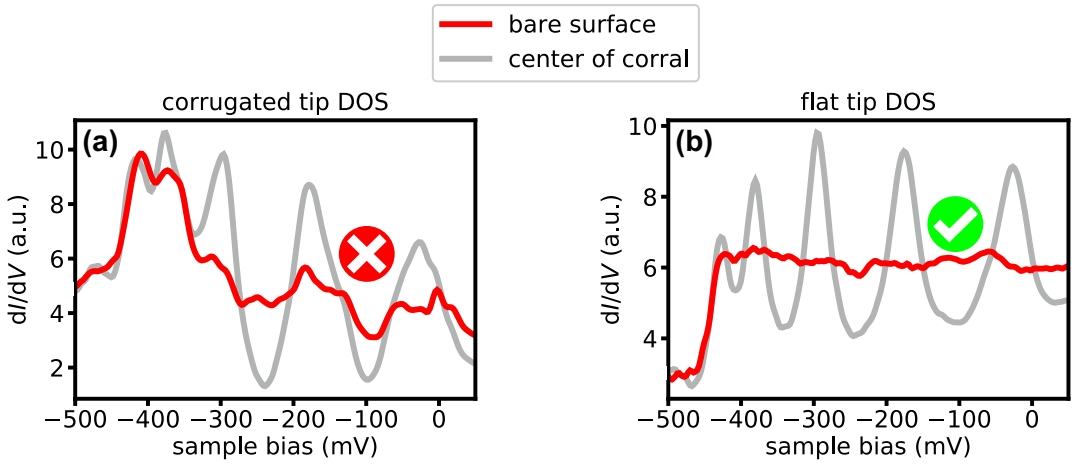


Figure 4.2: (a) red: $\mathrm{d}I/\mathrm{d}V$ spectrum measured over the bare Cu(111) surface with a tip that features a corrugated density of states (DOS). (b) red: $\mathrm{d}I/\mathrm{d}V$ spectrum measured over the bare Cu(111) surface with a tip that features a flat density of states. For reproducible and meaningful $\mathrm{d}I/\mathrm{d}V$ measurements, it is important to employ a tip that features a flat DOS, such as the one in (b). In (a) and (b) the gray lines represent $\mathrm{d}I/\mathrm{d}V$ measurements in the center of a circular quantum corral with a radius of $R_\mathrm{C} = 7.13\,\mathrm{nm}$. When using a tip with a corrugated DOS, the spectral features of interest (in this case the spectral features of the corral) are distorted, preventing a detailed analysis. When using a tip with a flat DOS, the spectral features of the measured object retain their original shape, allowing for further analysis.

a flat spectrum is obtained [see Fig. 4.2(b)]. Once achieved, the resulting tip provides reproducible and reliable STS measurements, where the measured $\mathrm{d}I/\mathrm{d}V$ signal directly reflects the electronic structure of the sample. The influence of a corrugated tip DOS on $\mathrm{d}I/\mathrm{d}V$ measurements can be seen by comparing the gray lines in Fig. 4.2(a) and (b), which represent spectra recorded over the center of a circular quantum corral of radius $R_\mathrm{C} = 7.13\,\mathrm{nm}$. While a non-flat tip DOS results in distorted spectral features [see Fig. 4.2(a)], a flat tip DOS preserves the intrinsic shape of the spectral features [see Fig. 4.2(b)].

4.2.2. Tips for atomic force microscopy measurements

Monoatomic metal-tips

The preparation and characterization of monoatomic metal-tips are described in detail in Refs. [32, 108]. Here, only the basic procedure is summarized.
Whether a tip is monoatomic can be checked in two steps. First, an STM scan of a

single CO molecule approximately reveals the sharpness of the tip. The apparent depth of a CO molecule in STM imaging correlates with the number of atoms at the tip apex [32]: A depth of about 60 pm at $V = 10\,\mathrm{mV}$ and $I = 100\,\mathrm{pA}$ typically indicates a monoatomic tip, while shallower depths suggest multiple front atoms. Figure 4.1(a) was scanned with a monoatomic metal-tip. If STM scans suggest a monoatomic tip, the CO front atom identification (COFI) method can be used for a precise apex characterization [30, 109, 110].

The COFI technique exploits the upright adsorption geometry of CO molecules. The oxygen atom at the top of the CO acts as a nanoscale probe for the tip apex [109, 110]. During a COFI measurement, the tip is scanned in constant height over a single CO molecule. The distance between tip and sample must be chosen large enough that the CO molecule is just not manipulated, in order to obtain the highest possible contrast in the Δf image. Typically, this is achieved with an STM setpoint of between 500 pA and 1 nA at 1 mV sample bias over bare copper and an oscillation amplitude of 50 pm. The resulting image reveals the number of atoms on the apex: Each dark (attractive) dip corresponds to one atom at the tip apex.

A COFI image obtained with a monoatomic metal-tip is shown in Fig. 4.3(a). The bright (repulsive) ring arises from Pauli repulsion between the apex atom and the CO molecule, while the central dark (attractive) area indicates a weak chemical interaction combined with van der Waals attraction. This weak interaction is directional and only appears when the apex atom is directly above the CO. A COFI image of a monoatomic metal-tip closely resembles the image of a single adatom scanned with a CO-tip [30, 31].

CO-tips

Once a monoatomic metal-tip has been prepared and verified, it can be further functionalized with a single CO molecule. This transforms the metal-tip into a CO-tip, which is widely used in high-resolution STM and AFM experiments. Terminating the tip with CO effectively reduces the chemical reactivity of the tip compared to a pure metal-tip [111, 112] while enhancing spatial resolution. The use of CO-tips has enabled numerous breakthroughs in high-resolution imaging of, for example, organic molecules [111, 113, 114], small metal clusters [30], and even the discrimination of bond orders [115]. In most cases, the enhanced spatial

resolution of CO-tips originates from the short-ranged Pauli repulsion between the CO and the charge density of the sample [112, 116]. This repulsive interaction of CO-tips with the sample contrasts with the mostly attractive interaction that metal-tips show. Sample systems have also been found in which the usually inert CO-tip forms a weak chemical interaction. For individual Fe and Cu adatoms on Cu(111), a weak chemical interaction leads to an attraction when the CO-tip is positioned directly above the adatom. This weak, directional interaction is the reason for a ring shape that appears in AFM images of this sample system [30, 31]. In the course of this thesis, CO-tips are used because their interaction with the corral states is dominated by short-range repulsion, providing a well-defined contrast mechanism that complements the predominantly attractive interaction observed with metal-terminated tips [17].

The CO pickup process follows a modified version of the procedure reported by Bartels *et al.* [117] and is further detailed in Refs. [32, 61]. The monoatomic metal-tip is positioned above the center of a CO molecule on the Cu(111) surface in STM feedback mode at a tunneling current of 2 nA and a sample bias of 10 mV. The sample bias is then slowly increased to 2.4 V while keeping the feedback loop active, causing the tip to retract. After the target voltage has been reached, the feedback loop is switched off and the tip is carefully approached toward the CO molecule in 10 pm steps while monitoring the detected tunneling current. A sudden increase indicates that the CO molecule has moved laterally, requiring the procedure to be restarted, while a sudden decrease in tunneling current suggests a CO pickup. The successful attachment of CO can then be verified using the COFI method, as shown in Fig. 4.3(b).

COFI images of CO-tips appear almost inverted compared to those of monoatomic metal-tips [see Fig. 4.3(a)]. The bright (repulsive) feature in the center originates from short-range Pauli repulsion between the two CO molecules, while the dark (attractive) ring surrounding it results from long-range van der Waals interactions.

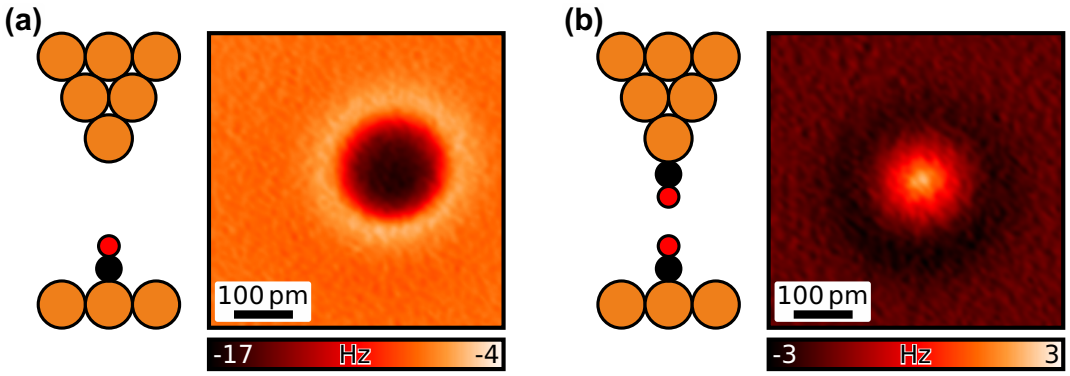


Figure 4.3: Tip characterization via the COFI method. (a) left: Schematic of a monoatomic metal-tip above a CO molecule adsorbed on Cu(111). (a) right: COFI image showing a dark central feature with a bright ring due to Pauli repulsion. (b) left: Schematic of a CO-tip above a CO molecule. (b) right: COFI image of a CO-tip showing a bright central spot with a surrounding dark ring. Both images were recorded in constant-height mode with an oscillation amplitude of 50 pm.

5. Tailoring electronic lifetimes of corral states

Most of the work presented in this chapter has been published in Physical Review B [118]. Parts of the text and figures presented below are reproduced from this publication. The experiments presented in Section 5.1 were carried out by the author. The measurements presented in Section 5.3 were performed with support from Michael Schelchshorn[1]. The first version of the methodology and initial results of the spectral line shape analysis are presented in the author's master's thesis [120].
This chapter reports on the characterization of the energy distributions of quantum corral states by means of scanning tunneling spectroscopy. Section 5.1 compares corrals of different sizes and shows that the spectral widths are strongly influenced by the confinement, i.e., by the corral wall. In addition, the measured energy distributions are found to exhibit a Gaussian rather than a Lorentzian line shape, contrary to what was previously reported [79].
To interpret these observations, a classical model is introduced in Section 5.2, relating the lifetime of a confined surface-state electron to its average path length inside the corral. The influence of the wall density is then examined in Section 5.3, where corrals with different CO wall densities are compared and denser corrals are found to host states with narrower energy distributions. Finally, the results are discussed in Section 5.4, including the relation between spectral width and wall density and possible mechanisms responsible for the Gaussian line shape, before the chapter concludes with a summary and outlook in Section 5.5.

5.1. Spectral line shape analysis

To perform a general spectroscopic characterization with a line shape analysis, two circular CO quantum corrals of different sizes were constructed: one with a radius of $R_{48,\mathrm{big}} = 7.13\,\mathrm{nm}$ (48 CO molecules) and another with a radius of $R_{24,\mathrm{small}} = 3.57\,\mathrm{nm}$

[1]Michael Schelchshorn did his master's thesis [119] in the group of Prof. Dr. Franz J. Giessibl under the supervision of the author.

(24 CO molecules). Both corrals share the same wall density, characterized by an average intermolecular CO distance of 938 pm. The construction plans of both corrals, including the exact adsorption positions of the CO molecules, are provided in Appendix A.1. STM images of the two structures are shown in Fig. 5.1(a) and (b).

5.1.1. General analysis

The spectral line shapes of the corral states are best studied by scanning tunneling spectroscopy. However, stationary $\mathrm{d}I/\mathrm{d}V$ measurements, where the tip position is fixed and the sample bias is swept, restrict the line shape analysis of energy distributions to states with $l = 0$, drastically limiting the number of analyzed distributions. The reason is that no lateral tip position can be found at which a state with $l \neq 0$ is both energetically and spatially isolated. This limitation is illustrated in Fig. 5.1(c). The red curve shows a stationary $\mathrm{d}I/\mathrm{d}V$ spectrum measured over the center of the big 48-CO corral. Only $l = 0$ states are probed at this position, as only these states possess a finite amplitude at the corral center. Each peak corresponds to an energy distribution of a corral state; from low to high bias, the peaks represent the states with $(n, l) = (1, 0)$ to $(n, l) = (7, 0)$.
The green curve in Fig. 5.1(c) was recorded 900 pm off center. At this position, states with $l = 0$ and $l = 1$ contribute to the measurement, leading to additional spectral features. Due to the overlap of multiple energy distributions, only the uppermost parts of the individual peaks remain visible. Access to only the peak maxima is insufficient for a detailed line shape analysis. Consequently, stationary $\mathrm{d}I/\mathrm{d}V$ spectroscopy is not suitable for a comprehensive investigation of energy distributions of states with $l \neq 0$.
A complete characterization of corral states requires simultaneous access to their spatial and energetic properties. This is achieved by recording constant-height $\mathrm{d}I/\mathrm{d}V$ line scans across the full diameter of the corral. In such measurements, the local density of states of the sample is probed as a function of position at a fixed energy defined by the applied bias voltage. To map the LDOS over a broad energy range, line scans were acquired across both corrals for bias voltages between -450 mV and 400 mV in steps of 5 mV.
Stacking the individual line scans along the energy axis yields the spatially and energetically resolved LDOS shown in Fig. 5.2. The horizontal axis corresponds to

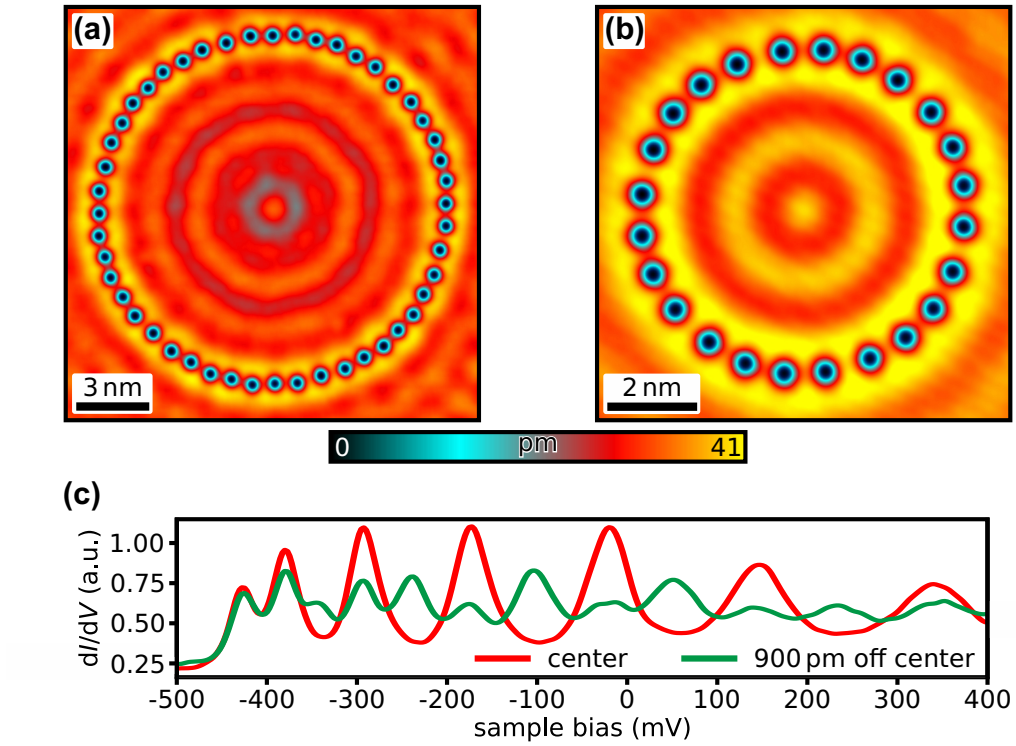


Figure 5.1: (a): Constant-current STM image of the big 48-CO quantum corral with a radius of $R_{48,\mathrm{big}} = 7.13\,\mathrm{nm}$, measured at a sample bias of 10 mV and a tunneling current setpoint of 10 pA. (b): Constant-current STM image of the small 24-CO quantum corral with a radius of $R_{24,\mathrm{small}} = 3.57\,\mathrm{nm}$, measured at a sample bias of 50 mV and a tunneling current setpoint of 100 pA. Both corrals share an identical average intermolecular CO distance of 938 pm. (c): Two stationary differential conductance ($\mathrm{d}I/\mathrm{d}V$) spectra measured inside the big 48-CO corral [see (a)] at different lateral positions. The red curve was acquired at the center of the corral and is sensitive exclusively to states with $l = 0$. The green curve was measured 900 pm off center and contains contributions from states with $l = 0$ and $l = 1$.

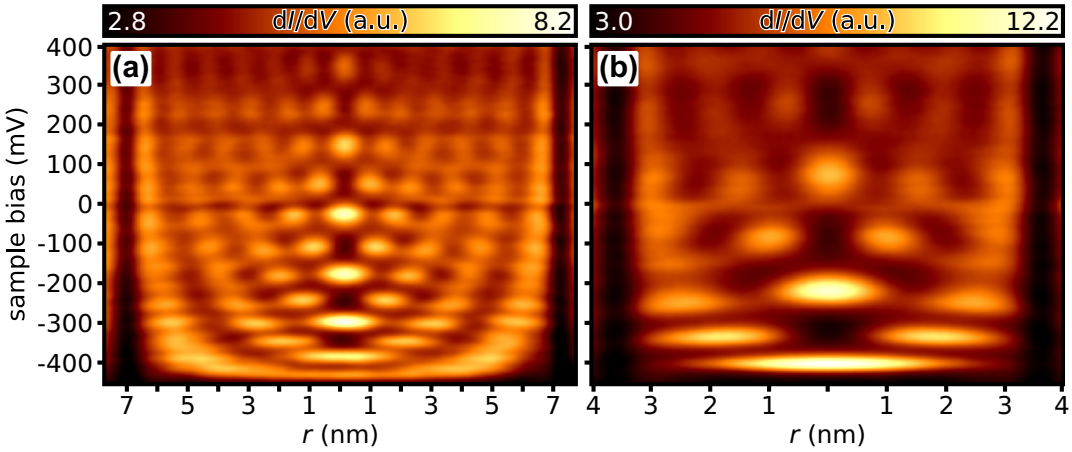


Figure 5.2: $\mathrm{d}I/\mathrm{d}V$ measurements as a function of radial distance r from the center of the quantum corrals and sample bias for the (a) big 48-CO corral and the (b) small 24-CO corral. In both panels, the two outermost vertical black lines indicate the positions of the corral walls formed by CO molecules. The bright features between these lines originate from the quantum corral states.

the radial position, the vertical axis to the sample bias, and the color scale encodes the differential conductance. Thus, each panel in Fig. 5.2 represents a complete LDOS map of the respective quantum corral.

To ensure a sufficient signal-to-noise ratio, each line scan was obtained by averaging seven individual constant-height scans acquired at a scan speed of 2 nm/s with 1024 pixels per line. For the big 48-CO corral, a setpoint of −170 mV and 170 pA was used, with the tip positioned above the corral center before disabling the feedback loop. This procedure ensured the same tip-sample distance for all scans. For the small 24-CO corral, a setpoint of 100 mV with 100 pA was chosen (again over the center of the corral). Differential conductance was measured using a modulation amplitude of $V_{\mathrm{mod}} = 5\,\mathrm{mV}$ at a frequency of 600 Hz.

Each horizontal slice of Fig. 5.2 represents a $\mathrm{d}I/\mathrm{d}V$ line scan that contains contributions from multiple corral states. Due to the energetic overlap of corral states, each state contributes with a different weight to the local density of states. As discussed in Subsection 3.2.2, the standing wave patterns observed in STM images of quantum corrals can be effectively described as linear combinations of corral states. This

concept can be extended to $\mathrm{d}I/\mathrm{d}V$ line scans recorded at different energies:

$$\frac{\mathrm{d}I}{\mathrm{d}V}(r, eV) \propto \sum_{n,l} \alpha_{n,l}(eV) \cdot |\Psi_{n,l}(r, \phi)|^2. \tag{5.1}$$

Here, the prefactor $\alpha_{n,l}(eV)$ quantifies the contribution of the probability density $|\Psi_{n,l}(r, \phi)|^2$ of a specific corral state to the measured LDOS at the energy eV. Accordingly, $\alpha_{n,l}(eV)$ represents the energy distribution of the corresponding corral state. A similar definition of the LDOS of a quantum corral has been used in the literature before, for example in Refs. [121, 122].

By fitting[1] Eq. (5.1) to the experimental data at each bias voltage, the energy distributions of a large number of corral states, including those with $l \neq 0$, can be extracted. Figure 5.3(a) shows a representative $\mathrm{d}I/\mathrm{d}V$ line scan recorded at $-170\,\mathrm{mV}$ across the big corral together with the corresponding fit. An excellent agreement between experiment and fit is observed not only for this example, but across the entire investigated bias range ($-450\,\mathrm{mV}$ to $400\,\mathrm{mV}$) for both corrals. This again confirms that the LDOS of a quantum corral is well described by a linear combination of states obtained from the hard wall model [17, 79] multiplied by the weighting function $\alpha_{n,l}(eV)$. A comparison between experimental data and fitted curves over the entire measured bias range is shown in Appendix A.2.

As a representative example, the extracted energy distribution $\alpha_{4,1}$ ($n = 4$, $l = 1$) of the big 48-CO corral is shown in Fig. 5.3(b). The full set of energy distributions $\alpha_{n,l}(eV)$, obtained with this analysis, is given in Appendix A.3.

To characterize the spectral properties of the corral states, the extracted energy distributions were analyzed in more detail. As a first approach, the distributions were fitted with a Lorentzian line shape L characterized by a full width at half maximum Γ_L, as originally proposed by Crommie *et al.* [79]. In addition to the intrinsic line shape, systematic broadening mechanisms inherent to $\mathrm{d}I/\mathrm{d}V$ measurements must be considered. These include the temperature-dependent broadening of the Fermi-Dirac distribution, radio-frequency broadening, and modulation broadening, as discussed in Subsection 2.2.2. Accounting for these effects, the energy distributions were fitted using

$$\alpha_{n,l} \propto L * G_\mathrm{Fermi,RF} * \chi_\mathrm{mod}. \tag{5.2}$$

[1] All of the curve fitting and parameter optimization shown in this thesis were performed using the LMFIT package (version 1.0.1) in Python [123].

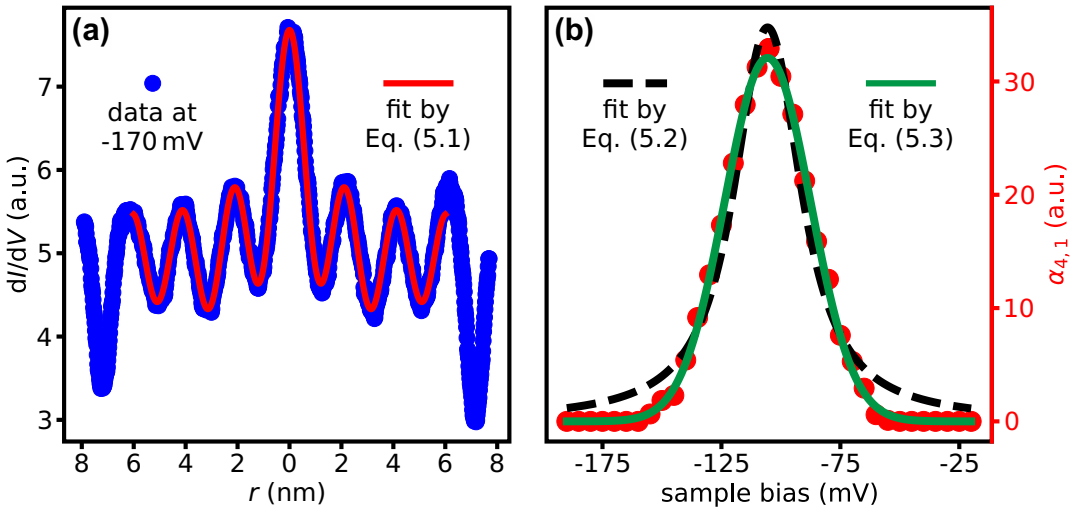


Figure 5.3: (a) Blue: Experimental $\mathrm{d}I/\mathrm{d}V$ line scan, measured at a sample bias of $-170\,\mathrm{mV}$ across the big 48-CO corral. Red: Fit of Eq. (5.1) to the measured curve. (b): Energy distribution $\alpha_{4,1}$ of the big 48-CO corral (red markers). The black dashed line shows a fit using Eq. (5.2), consisting of a Lorentzian line shape and instrumental broadening terms, which yields poor agreement. The solid green line shows the fit obtained with Eq. (5.3), including both a Lorentzian contribution with associated width Γ_L and a Gaussian contribution with associated width Γ_wall as well as instrumental broadening, and provides excellent agreement with the data. The fit reveals a purely Gaussian energy distribution with $\Gamma_\mathrm{L} = 0\,\mathrm{meV}$ and $\Gamma_\mathrm{wall} = 41\,\mathrm{meV}$.

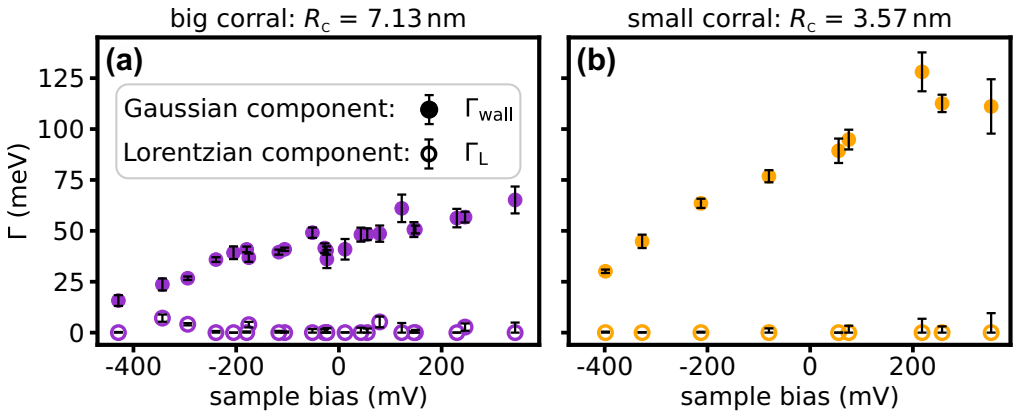


Figure 5.4: Comparison of the Gaussian and Lorentzian full widths at half maximum, Γ_{wall} (filled symbols) and Γ_{L} (open symbols), extracted from the energy distributions of the (a) big 48-CO corral and the (b) small 24-CO corral. Within the fit uncertainty, the Gaussian contribution dominates the spectral line shape, while the Lorentzian contribution is negligible.

However, fits based on a purely Lorentzian line shape result in a poor description of the energy distributions, as illustrated by the black dashed curve in Fig. 5.3(b). To improve the agreement, an additional Gaussian contribution G_{wall} with associated width Γ_{wall} was introduced

$$\alpha_{n,l} \propto L * G_{\text{wall}} * G_{\text{Fermi,RF}} * \chi_{\text{mod}}. \tag{5.3}$$

Including the Gaussian term leads to a substantial improvement of the fits, as demonstrated by the solid green curve in Fig. 5.3(b). For the representative energy distribution $\alpha_{4,1}$, the extracted widths are $\Gamma_{\text{L}} = \left(0^{+}_{(-)}2\right)$ meV and $\Gamma_{\text{wall}} = (41 \pm 1)$ meV, indicating that the energy distribution is entirely dominated by the Gaussian component. The uncertainty corresponds to twice the standard deviation obtained from the fit.

Applying this analysis to all reliably extracted energy distributions yields a consistent result: In all cases, the Lorentzian contribution is negligible within the uncertainty, whereas the Gaussian shape with associated width Γ_{wall} dominates the line shape. Figure 5.4 summarizes the extracted Gaussian and Lorentzian widths for both corrals.

From the analysis of the energy distributions $\alpha_{n,l}(eV)$, several key conclusions can be drawn. First, the spectral line shapes of the corral states are not well described

by a Lorentzian function. This is in contrast to existing literature, which proposed that the energy distributions are described by a Lorentzian line shape [79]. Second, all analyzed energy distributions exhibit a pronounced Gaussian line shape. Third, as presented in Fig. 5.4, the width of the distributions, Γ_{wall}, shows a monotonic energy dependence. Fourth, the overall magnitude of Γ_{wall} depends on the size of the corral.
Before discussing the physical origin of these observations, it is essential to assess the reliability and robustness of the extraction procedure used to obtain the energy distributions from the $\mathrm{d}I/\mathrm{d}V$ line scans. This assessment is presented in the following subsection.

5.1.2. Details and quality assessment of the analysis

Since the quality of the fits of Eq. (5.1) to the experimental $\mathrm{d}I/\mathrm{d}V$ line scans directly determines the reliability of the extracted energy distributions $\alpha_{n,l}(eV)$, several measures were implemented to ensure the robustness and accuracy of the fitting procedure. These measures address the choice of fitting parameters and the consistency of the extracted line shapes.

Fitting routine Fitting Eq. (5.1) to experimental $\mathrm{d}I/\mathrm{d}V$ line scans involves a large number of free parameters, as one coefficient $\alpha_{n,l}$ is, in principle, required for every corral state at every energy. Allowing all possible states to contribute simultaneously would lead to an impractical and unstable fitting problem. To obtain reliable results, a compromise was therefore sought between capturing the physically relevant contributions and minimizing the number of free parameters.
For each line scan, only a subset of corral states was included in the fit function. This subset was chosen based on the estimated energy widths and the proximity of the expected state energies to the bias voltage of the respective line scan. When the bias voltage of the line scan approached the energy of a given state, a test fit was performed including this additional state. If the corresponding coefficient $\alpha_{n,l}$ converged to a finite value above the imposed lower bound ($\alpha_{n,l} > 0$), the state was retained in the fitting function. If the coefficient vanished within numerical accuracy ($\alpha_{n,l} = 0$), the state was excluded and the fit was repeated.
A similar criterion was applied to remove states from the fit function. Once

the coefficient $\alpha_{n,l}$ of a state remained zero over several consecutive line scans, corresponding to an energy interval of approximately 10 meV to 15 meV, the state was excluded from further fits. Following this procedure ensured that each fit involved only a manageable number of parameters (< 13) while maintaining a high fit accuracy. With this approach, the relative uncertainties of the extracted $\alpha_{n,l}$ values were typically limited to single-digit percentages.

Quality factor and selection of reliable energy distributions Despite the overall stability of the fitting procedure, not all extracted energy distributions are equally reliable. This is particularly relevant for states with identical main quantum number n and large angular momentum quantum number l, since such states exhibit a highly similar spatial behavior. Because the method relies on extracting energy distributions from experimental $\mathrm{d}I/\mathrm{d}V$ line scans, the application of the fitting algorithm via Eq. (5.1) is limited by its ability to distinguish between these highly similar states.
To quantify the reliability of each extracted energy distribution, a quality factor ξ was introduced. This factor is based on the relative quadratic deviation (RQD) between the extracted distribution $\alpha_{n,l}(eV)$ and its corresponding line shape fit. The RQD is defined as

$$\mathrm{RQD} = \frac{\sum_{i=0}^{N}\left[\alpha_{n,l}\left(V^{(i)}\right) - \mathrm{F}\left(V^{(i)}\right)\right]^2}{\sum_{i=0}^{N}\left[\mathrm{F}\left(V^{(i)}\right)\right]^2}. \tag{5.4}$$

In this expression, $\alpha_{n,l}\left(V^{(i)}\right)$ describes the value of the energy distribution at the sample voltage $V^{(i)}$, while $\mathrm{F}\left(V^{(i)}\right)$ is given by the value of the fit of Eq. (5.3) at the same bias voltage. The total number of values per energy distribution $\alpha_{n,l}$ is given by N. The quality factor is then defined as

$$\xi = 1 - \mathrm{RQD}. \tag{5.5}$$

In order to maximize the overall accuracy of the line shape analysis, further analysis was constrained to energy distributions with $\xi > 0.8$. Within the measured bias range of -450 mV to 400 mV, a total of 61 and 15 energy distributions were extracted

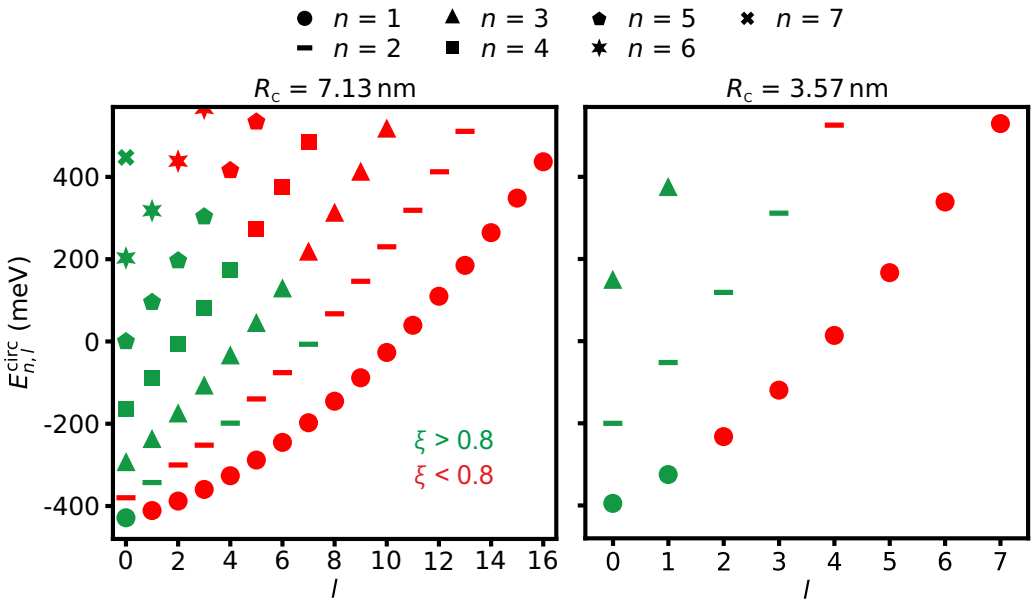


Figure 5.5: Overview of the extracted energy distributions for the big 48-CO (left) and small 24-CO (right) corral. Energy distributions shown in green fulfill the quality criterion $\xi > 0.8$ [see Eq. (5.5)] and were included in the line shape analysis (see Subsection 5.1.1 and Section 5.2). Distributions marked in red do not meet the quality criterion and were excluded from further analysis.

for the big and small corral, respectively, with distributions of degenerate states ($\pm l$) counting as one. Applying the quality criterion reduced this set to 23 distributions for the big corral and 8 distributions for the small corral. An overview of the accepted and rejected distributions is shown in Fig. 5.5.

It is important to emphasize that the line scan fitting approach significantly increases the number of analyzable energy distributions compared to conventional stationary $\mathrm{d}I/\mathrm{d}V$ spectroscopy. A stationary spectrum from $-450\,\mathrm{mV}$ to $400\,\mathrm{mV}$, acquired over the center of the corral, would allow a reliable line shape analysis only for states with $l = 0$, corresponding to 7 and 3 states for the big and small corrals, respectively. The present line scan fitting method increased the number of analyzed states by factors of ≈ 3.3 for the big corral and ≈ 2.7 for the small corral.

The representative energy distribution $\alpha_{4,1}$ shown in Fig. 5.3(b) has a quality factor of $\xi = 0.96$.

Comparing line shapes determined by line scan fitting and static tunneling spectroscopy To further assess the consistency of the results obtained with the line

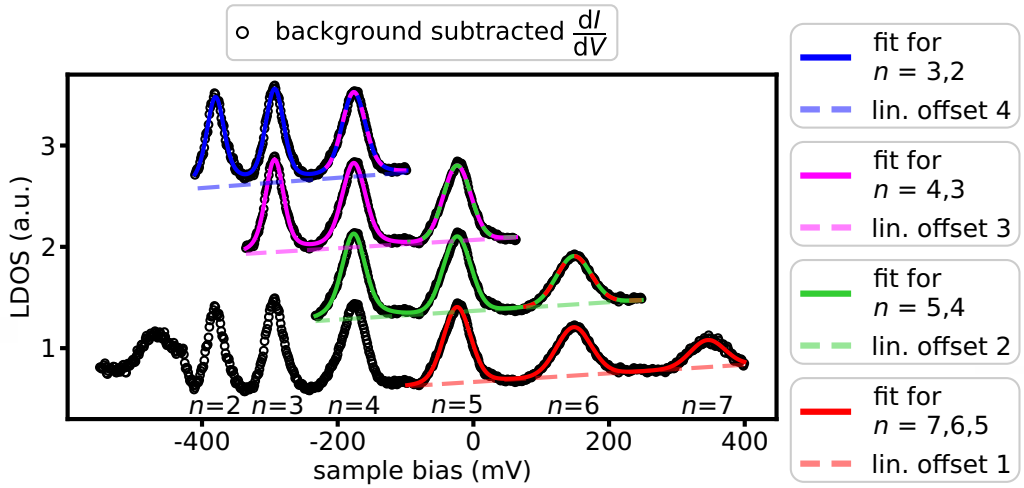


Figure 5.6: $\mathrm{d}I/\mathrm{d}V$ spectrum measured over the center of the big 48-CO corral after application of the background removal procedure developed by Wahl *et al.* [124], shown as open black markers. The spectrum is normalized at a sample bias of 0 mV. Each peak corresponds to an $l = 0$ corral state. The corresponding main quantum number n is given below each peak. Due to the background removal procedure, the peak for $n = 1$ merges with the band edge of the Shockley surface state. At higher energies ($n = 5, 6, 7$), the peaks are well separated. The segmented fitting approach described in the text is illustrated by the colored lines, with the corresponding linear background offsets shown as dashed lines.

scan fitting method, the full widths at half maximum of the reconstructed energy distributions are compared to widths extracted from static $\mathrm{d}I/\mathrm{d}V$ measurements acquired over the center of the corral. As already discussed, such static tunneling spectroscopy measurements are particularly sensitive to states with the angular momentum quantum number $l = 0$. A background-removed $\mathrm{d}I/\mathrm{d}V$ spectrum[1] taken over the center of the big 48-CO corral is shown as open black markers in Fig. 5.6. Upon closer inspection of the spectrum in Fig. 5.6, a clear separation of peaks is observed at higher energies, particularly for the states with $n = 5, 6$, and 7, which is characterized by flat regions between neighboring maxima. The individual peaks appear on top of a smooth background that increases in intensity with increasing energy.

[1] As discussed in Section 2.2, a $\mathrm{d}I/\mathrm{d}V$ spectrum is sensitive to the density of states of both the sample and the tip. To minimize the influence of the tip, tips exhibiting a flat density of states were used (see Section 4.2). To further reduce residual effects of a non-ideal tip DOS, the full deconvolution background removal algorithm developed by Wahl *et al.* [124] was applied. In addition, the background removal normalizes all spectra at a sample bias of 0 mV.

To account for this slowly varying offset, a dedicated fitting strategy is required. Since the precise energy dependence of this background is not known a priori, the spectrum is analyzed sequentially in overlapping energy windows. Fitting individual peaks in isolation is insufficient due to the influence of neighboring peaks. Therefore, each fitting step includes three spectral peaks. The first fitting step comprises the three highest-energy peaks ($n = 7, 6, 5$), using a fitting function consisting of a linear offset and three individual peaks described by Eq. (5.3). The resulting fit is shown by the solid red line in Fig. 5.6, while the corresponding linear offset is indicated by the red dashed line.

In the next step, the subsequent set of peaks ($n = 6, 5, 4$) is analyzed. The parameters of the $n = 6$ state obtained in the previous fitting step (namely Γ_{wall}, Γ_{L}, amplitude, and energy position) are fixed, leaving only the remaining two peaks and the linear offset as free parameters. This fit is illustrated by the green solid line in Fig. 5.6, with the fixed contribution of the $n = 6$ state indicated by the red-green dashed segment.

The same procedure is subsequently applied to the $n = 5, 4, 3$ set, fixing the parameters of the $n = 5$ state. This fitting step is shown by the magenta solid line, with the fixed contribution depicted by the green-magenta dashed segment. The sequential fitting routine is continued until the $n = 4, 3, 2$ set is reached.

Due to the merging of the $n = 1$ state with the band edge of the Shockley surface state during the background removal procedure, the $n = 1$ state could not be included in this analysis.

Figure 5.7(a) shows the Gaussian width parameter Γ_{wall} extracted from the static $\mathrm{d}I/\mathrm{d}V$ spectrum (red markers). These values closely match those obtained from the line scan fitting method (purple markers) within the experimental uncertainty[1]. A consistent trend is also observed for the Lorentzian components within the experimental uncertainty, as shown in Fig. 5.7(b).

The close agreement between the widths obtained from static spectroscopy and line scan fitting, as shown in Fig. 5.7, supports the validity and robustness of the line scan fitting approach and shows that both methods consistently yield predominantly Gaussian-shaped energy distributions for the corral states.

Note that the energy distribution of the state with $n = 2$ and $l = 0$ did not meet the

[1] As in the line scan fitting approach, the error bars of the static measurements correspond to twice the standard deviation obtained from the fit.

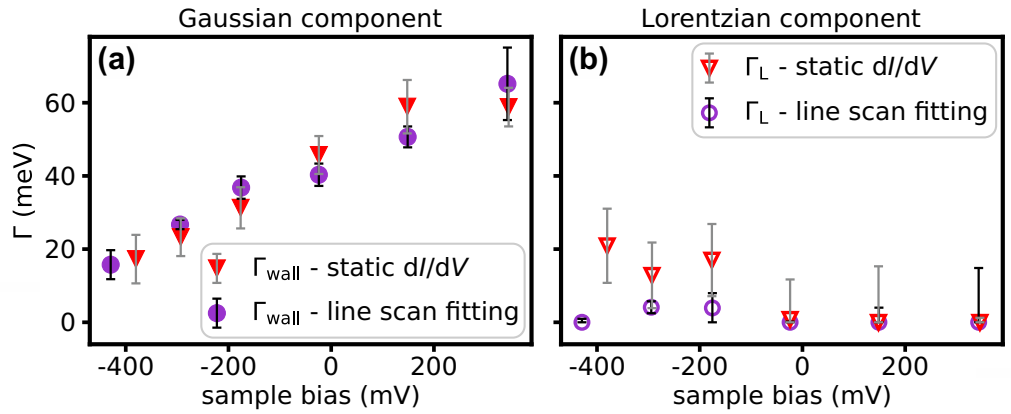


Figure 5.7: Comparison of the Gaussian and Lorentzian width parameters (Γ_{wall} and Γ_{L}) obtained from line scan fitting (purple markers) and from a static $\mathrm{d}I/\mathrm{d}V$ spectrum measured over the center of the big 48-CO corral (red markers) for states with $l = 0$. (a): Gaussian component Γ_{wall}. (b): Lorentzian component Γ_{L}. Both analysis methods yield consistent width parameters within the experimental uncertainty and indicate that the energy distributions of the corral states are predominantly Gaussian-shaped.

quality criterion of the line scan fitting approach (see Fig. 5.5) and was not further analyzed. Therefore, no data point is provided for this state in Fig. 5.7, whereas the static $\mathrm{d}I/\mathrm{d}V$ analysis does provide a data point for this state. Additionally, due to the background removal procedure the state with $n = 1$ and $l = 0$ was not analyzed in the static $\mathrm{d}I/\mathrm{d}V$ measurement. Consequently, only the data point from the line scan fitting approach is shown for this state.

5.2. The spectral width in a single parameter – average path length

As discussed in Subsection 3.2.4, several mechanisms limit the lifetime of confined surface-state electrons, including electron-phonon scattering, electron-electron scattering, and electron-defect scattering. As shown in the previous section, the spectral widths of the energy distributions exhibit a monotonic energy dependence. In addition, the widths depend on the corral size (see Fig. 5.4). This experimentally observed behavior is in agreement with previous theoretical calculations by Crampin *et al.* [23]. Similar to their interpretation, the results presented here indicate that

the dominant limitation of the corral state lifetime[1] originates from the interaction of surface-state electrons with the corral wall, i.e., electron-defect scattering.
Due to its spatial homogeneity, electron-phonon scattering is not sensitive to the size of the quantum structure [21, 22]. Moreover, this scattering mechanism leads to Lorentzian line shapes. Therefore, it does not correlate with the experimentally observed strong size dependence of the spectral widths or with the predominantly Gaussian line shapes.
Calculations by Stilp *et al.* [17] revealed that the total electron density in the big and small corrals investigated here is identical ($\approx 0.64\ \mathrm{e}^-/\mathrm{nm}^2$). Since electron-electron scattering scales with the total electron density [96, 125–127], this mechanism is likewise expected to be independent of the corral size. Furthermore, electron-electron scattering would also result in Lorentzian line shapes.
Previous studies on vacancy islands on Ag(111) [128], which have sizes comparable to the corrals investigated in this work, also reported a negligible influence of both electron-electron and electron-phonon scattering on the lifetime (i.e., inverse spectral width) of confined surface states in quantum structures.
Since neither the observed Gaussian line shape nor the size-dependent widths Γ_{wall} can be explained by electron-electron or electron-phonon scattering, it can be concluded that the dominant limitation of the lifetime is mainly given by the interaction of surface-state electrons with the corral wall. This interaction includes lateral transmission through the corral wall (e.g., tunneling) as well as, for example, scattering into bulk states (absorption). A more detailed discussion of these mechanisms is provided in Subsection 5.4.1.
In the following, a classical model is introduced to describe and quantify the energy dependence of the spectral widths Γ_{wall}. The central idea of this model is to relate Γ_{wall} to the average path length x traveled by a surface-state electron during its lifetime. The model is purely phenomenological and does not attempt to describe the microscopic scattering processes in the corral. Instead, it provides a compact parameterization of the experimentally observed energy dependence of the spectral widths.
The average path length x covered by an electron moving with velocity v_{e} during its lifetime T_{life} can be written as $x = v_{\mathrm{e}} \cdot T_{\mathrm{life}}$. Using a classical expression for the

[1] The width Γ of a spectral feature and the lifetime T_{life} of electrons occupying the corresponding corral state are inversely proportional: $T_{\mathrm{life}} = \hbar/\Gamma$.

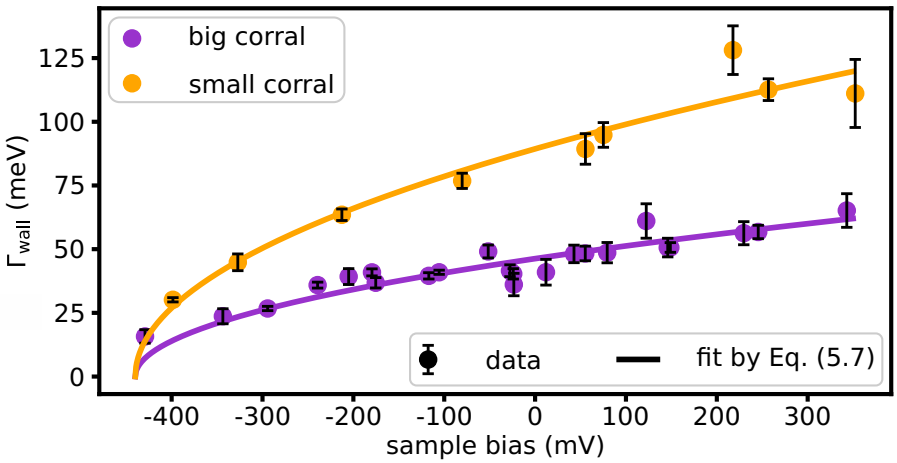


Figure 5.8: Experimentally determined Gaussian spectral widths Γ_{wall} as a function of energy for the big 48-CO corral ($R_{48,\text{big}} = 7.13\,\text{nm}$, purple markers) and the small 24-CO corral ($R_{24,\text{small}} = 3.57\,\text{nm}$, orange markers). Solid lines show fits using the average path length model, Eq. (5.7), which relates the measured spectral width to the electron energy. The fits yield average path lengths of $x_{48,\text{big}} = (9.1 \pm 0.4)$ nm and $x_{24,\text{small}} = (4.7 \pm 0.3)$ nm.

electron velocity as a function of its energy E relative to the surface-state band onset, where $E = eV + 440\,\text{meV}$, one obtains

$$x = \sqrt{\frac{2(eV + 440\text{ meV})}{m_e^*}} \cdot T_{\text{life}}. \tag{5.6}$$

For the effective mass m_e^* of surface-state electrons on Cu(111), the value determined by Crommie *et al.* [15] is used, which is 0.38 times the mass of a free electron: $m_e^* = 0.38 \cdot m_e$. By relating the lifetime to the spectral width via $T_{\text{life}} = \hbar/\Gamma$, the spectral width can be written as

$$\Gamma = \frac{\hbar\sqrt{\frac{2(eV+440\text{ meV})}{m_e^*}}}{x}. \tag{5.7}$$

Within this framework, the average path length x is an energy-independent parameter that can be determined for each corral by fitting Eq. (5.7) to the experimentally determined widths Γ_{wall} (see Fig. 5.4). The resulting fits for the big and small corral are shown in Fig. 5.8, yielding values of $x_{48,\text{big}} = (9.1 \pm 0.4)\,\text{nm}$ and $x_{24,\text{small}} = (4.7 \pm 0.3)\,\text{nm}$.

The average path length model offers three key advantages. First, it provides a very good description of the experimentally observed energy dependence of the spectral widths Γ_{wall}. Second, the extracted values of $x_{48,\text{big}}$ and $x_{24,\text{small}}$ differ by a factor of 1.9 ± 0.3, which closely matches the ratio of the corral radii ($R_{48,\text{big}}/R_{24,\text{small}} = 2$). This indicates that, for a fixed wall density, the average path length scales with the corral radius, further supporting the conclusion that the dominant lifetime limitation arises from interactions with the corral wall. Third, the model allows the lifetimes of corral states (which are a function of energy) to be characterized by a single parameter, the average path length x.

In the following sections, the average path length model will be used to analyze how modifications of the corral wall, in particular variations in the wall density, affect the average path length and thereby the spectral widths (proportional to the inverse lifetime) of the confined states.

5.3. Variation of the wall density

The results presented so far demonstrate that the lifetime of corral states is related to the interaction of confined surface-state electrons with the corral wall. This interpretation is also supported by theoretical work by Crampin *et al.* [23], which employed an interaction mechanism similar to that introduced by Heller *et al.* [24] to calculate the lifetimes of corral states, explicitly accounting for lossy scattering at the corral boundary. In theoretical considerations, this loss term is commonly associated with coupling to bulk states (e.g., Refs. [24, 97, 129]). Furthermore, recent experimental findings indicate that scattering at corral boundaries enables coupling of corral states to bulk states in a superconducting substrate [130].

While the theoretical work by Crampin *et al.* [23] correctly reproduces the trend that smaller quantum corrals host broader energy distributions (see Fig. 5.4), the calculated energy dependence of the spectral widths exhibits a steeper slope than observed experimentally. As a consequence, the widths of higher-energy states are overestimated, whereas those of lower-energy states are underestimated. This discrepancy likely arises because the calculations of Crampin *et al.* rely on Heller's "black-dot" model [24], characterized by a purely absorbing δ-function potential, which was developed for Fe-based corrals and may not adequately describe CO-based

quantum corrals. To further investigate the role of the electron-wall interaction in quantum corrals on Cu(111), the spectral widths of corral states were studied as a function of the wall density (ρ_{wall}). The wall density is defined as the ratio of the number of CO molecules forming the wall to the circumference of the corral.

The starting point of this investigation is the big 48-CO corral [see Figs. 5.1(a) and 5.9(c)]. Corrals with lower and higher wall densities were constructed while keeping the radius fixed (7.13 nm), using 96, 48, 24, 16, and 12 CO molecules in the wall, respectively. STM images of the resulting corrals are shown in Fig. 5.9. For the 96-CO corral, two distinct configurations, denoted 96_1 and 96_2, are possible. They differ in the adsorption sites of 24 of the 96 CO molecules, for each of which the two possible sites are neighboring positions on the Cu lattice. Both configurations were obtained by starting from the 48-CO corral construction plan and inserting additional CO molecules at possible adsorption sites. Conversely, corrals with reduced wall density were created by selectively omitting CO molecules. The detailed construction plans for all corrals with varying wall densities are provided in Appendix A.1. The average intermolecular distances (i.e., the inverse wall densities) are 3719 pm, 2792 pm, 1876 pm, 938 pm, and 477 pm for the 12-, 16-, 24-, 48-, and both 96-CO corrals, respectively. Notably, the two 96-CO corral variants have the maximum achievable wall density for CO on Cu(111). Heinrich *et al.* [11] investigated the stability of CO nanostructures on Cu(111) and demonstrated that more densely packed CO assemblies undergo structural rearrangements on timescales shorter than 1 min. Such unstable configurations would be required to realize corrals with even higher wall densities.

To characterize the influence of the wall density on the spectral width (and thus the inverse lifetime) of corral states, static $\mathrm{d}I/\mathrm{d}V$ spectra were acquired at the center of each corral. The background-removed spectra [124] are shown in Fig. 5.10.

A first qualitative comparison of the spectra in Fig. 5.10 shows that the most pronounced difference between the spectra is the width of the spectral peaks. The widths decrease monotonically with increasing wall density: The 96-CO corrals exhibit the narrowest peaks, while the 12-CO corral shows the broadest ones.

For both 96-CO configurations, additional spectral features appear between the main $l = 0$ peaks. These weaker peaks can be attributed to states with $l \neq 0$. One possible contributing factor is the finite lateral extent of the tip apex. For the measurements shown in Fig. 5.10, a tip terminating in three metal atoms was

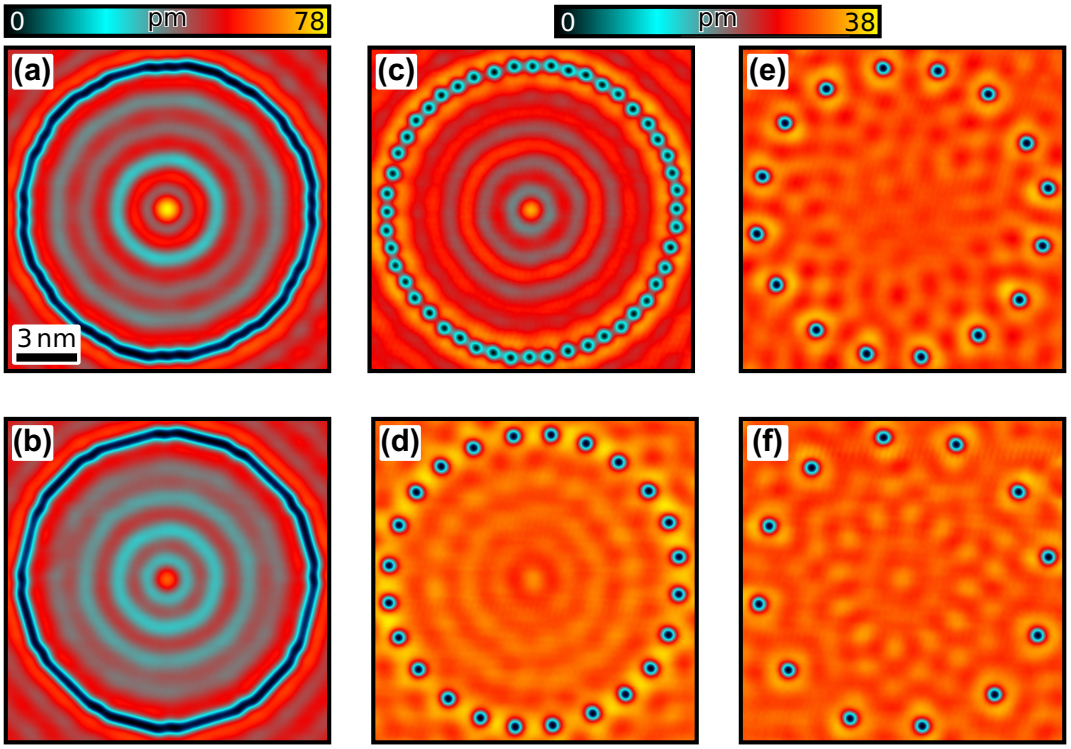


Figure 5.9: Constant-current STM images (−10 mV, 100 pA) of quantum corrals with different wall densities: 96_1-CO in (a), 96_2-CO in (b), 48-CO in (c), 24-CO in (d), 16-CO in (e), and 12-CO in (f). The 12-, 16-, and 24-CO corrals were constructed using subsets of the adsorption sites occupied in the 48-CO corral, whereas both 96-CO configurations contain all 48 of these sites together with 48 additional CO molecules. Images (a) and (b) share a common color scale, as do images (c) to (f).

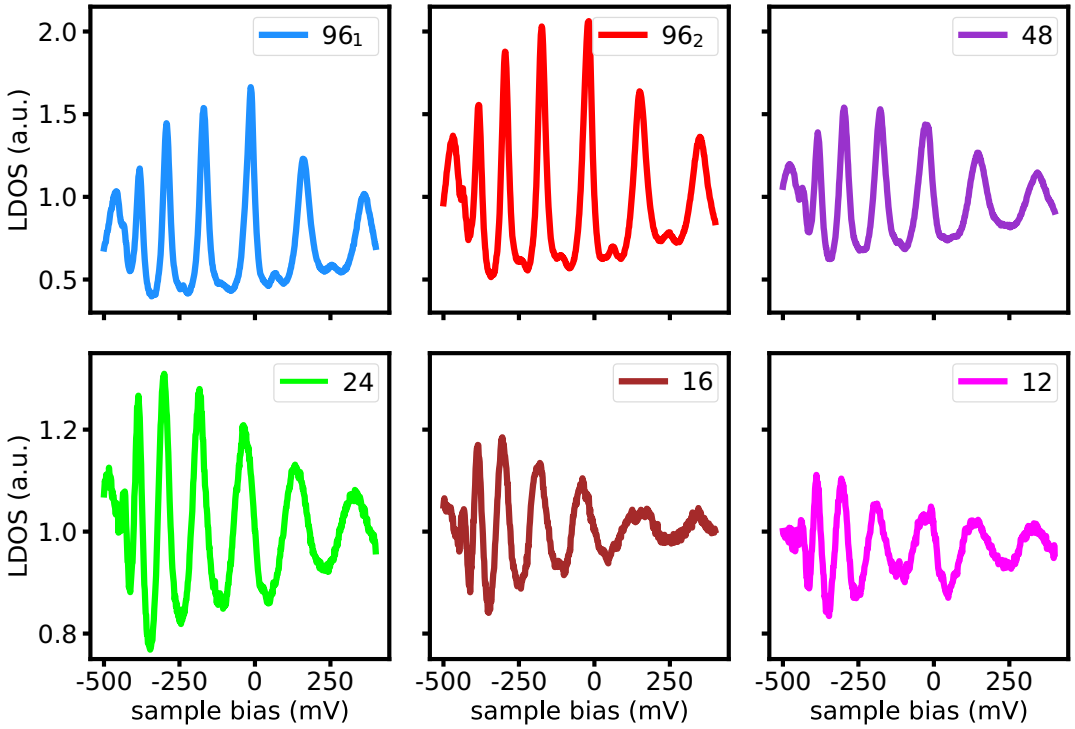


Figure 5.10: Background-removed $\mathrm{d}I/\mathrm{d}V$ spectra [124] measured over the center of CO quantum corrals with different wall densities. All corrals have the same radius (7.13 nm) but differ in the number of CO molecules forming the wall. Two distinct configurations exist for the 96-CO corral.

used, as verified by the COFI method (see Section 4.2). The enhanced sensitivity to $l \neq 0$ states in spectra acquired at the center of the 96-CO corrals is further aided by the comparatively narrow spectral widths of all corral states. Consequently, neighboring resonances overlap less strongly, allowing the weaker $l \neq 0$ peaks to remain distinguishable from the dominant $l = 0$ peaks.

The full widths at half maximum Γ_{wall} of the spectral peaks[1] are summarized in Fig. 5.11(a), where a pronounced energy dependence is again observed. This dependence is well captured by the average path length model introduced in Section 5.2 [Eq. (5.7)], as indicated by the solid lines in Fig. 5.11(a). Despite the overall good agreement between the average path length model and the data, outliers are observed in the cases of the 16-CO corral and the 12-CO corral. For the 16-CO corral, the state with $n = 6$ and $l = 0$ at approximately 150 mV stands out, while for the 12-CO corral, the outliers include the $n = 4$, $l = 0$ state at approximately -200 mV and the $n = 6$, $l = 0$ state at around 150 mV. One possible origin of these anomalies is the lower wall density of the 16- and 12-CO corrals. The sparse walls may allow surface-state waves scattered by nearby adsorbates, defects, or step edges to penetrate more strongly into the corral and interfere with the confined standing wave patterns, thereby modifying the measured energy distributions of the corral states. In addition, the larger gaps between neighboring CO molecules may produce stronger variations in the confinement potential along the corral wall, potentially shifting the energies of individual corral states or inducing mixing between states with similar energies. In general, the average deviation of the data points from the fit, including the outliers, is 5%.

The corresponding fitted average path lengths for the different corrals are shown in Fig. 5.11(b). As the corral walls become more densely packed with CO molecules, the extracted average path length of the confined surface-state electrons increases. This behavior is qualitatively consistent with the theoretical considerations of Crampin *et al.* [23]. An empirical fit further reveals that the average path length x scales as $\sqrt{\rho_{\text{wall}}}$. This is indicated by the solid red line in Fig. 5.11(b).

[1] For this analysis, the data were fitted using a combination of seven pure Gaussian curves and a single linear offset. The modulation broadening was included in the fit function as a convolution with a semicircular function [see Eq. (2.10)]. The same applies to the Fermi- and RF-broadening, which were accounted for as additional Gaussian broadening terms [see Eq. (2.12) and (2.13)]. This particular analysis was performed by Michael Schelchshorn. A closely related analysis method is described in his master's thesis [119].

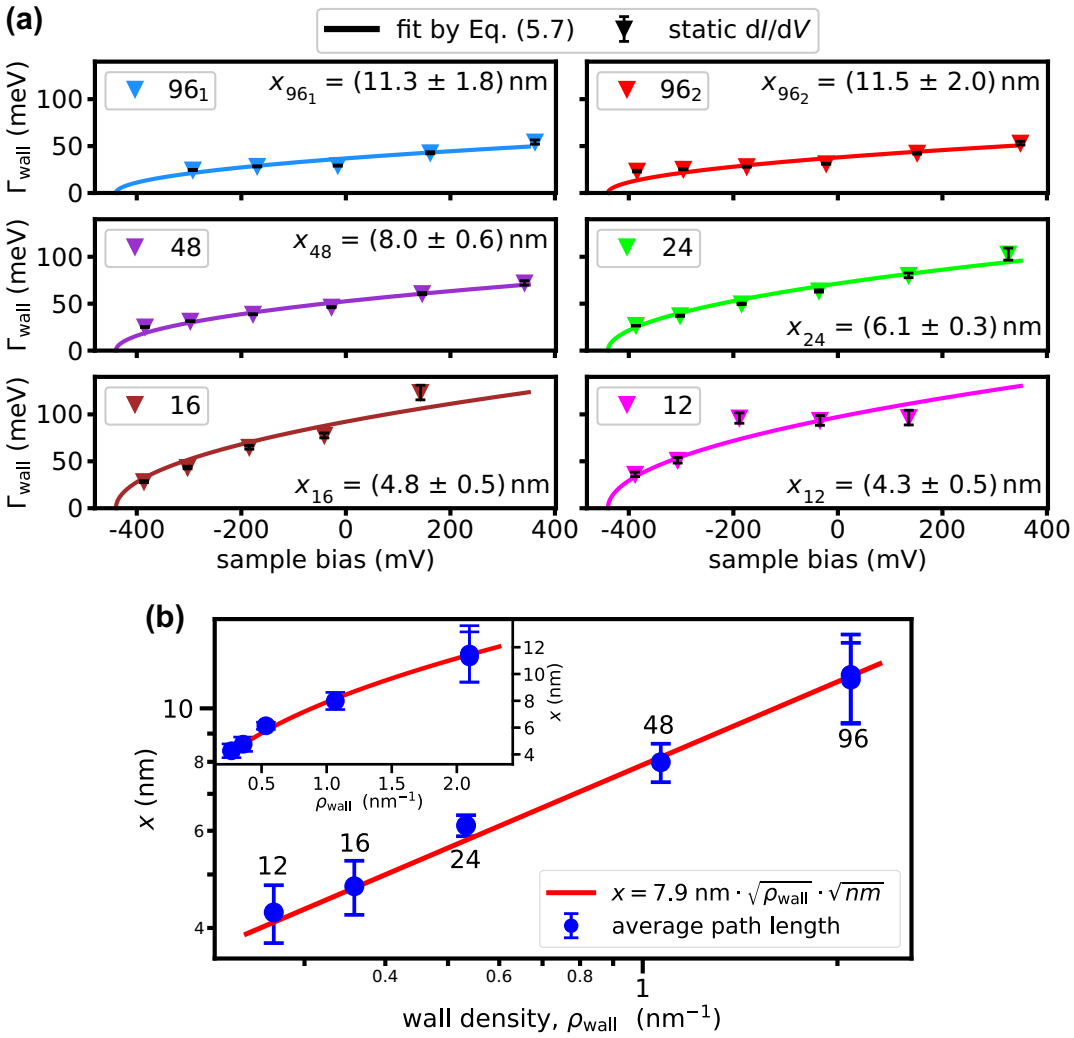


Figure 5.11: (a): Energy-dependent spectral widths Γ_{wall} of $l = 0$ corral states measured at the center of quantum corrals with different wall densities and a common radius of 7.13 nm. Solid lines represent fits of the average path length model [Eq. (5.7)]. The average path lengths x of the confined electrons in each quantum corral are displayed in every plot. (b): Average path length x extracted from the fits in (a) as a function of wall density ρ_{wall} (logarithmic scale). Blue markers denote the data points; numbers indicate the corresponding number of CO molecules in the corral wall. The inset presents the same data on a linear scale. The red line shows the empirical relationship.

5.4. Discussion

5.4.1. Relating spectral width and wall density

As highlighted in Section 5.2, the dominant mechanism limiting the lifetime of confined surface-state electrons in a quantum corral is their interaction with the corral wall. In general, three processes can occur when an electron interacts with the wall: reflection, absorption (for example, into bulk states), and lateral transmission. The latter two are lossy[1] channels. Considering these three interaction mechanisms, the total probability for an electron-wall interaction can be written as

$$P_{\mathrm{R}} + P_{\mathrm{A}} + P_{\mathrm{T}} = 100\%. \tag{5.8}$$

Experimentally, the respective probabilities (P_{R} for reflection, P_{A} for absorption, and P_{T} for transmission) are found to scale with the wall density ρ_{wall}.
For a wall density of $\rho_{\mathrm{wall}} = 0\ \mathrm{nm}^{-1}$, the probability for transmission is $P_{\mathrm{T}} = 100\%$, since neither reflection nor absorption at a boundary is possible. As the wall density ρ_{wall} increases, the separation between neighboring CO molecules decreases, which is expected to reduce the probability P_{T} for lateral transmission through the corral wall. Furthermore, the experimental results clearly show (see Figs. 5.10 and 5.11) that the lifetimes of corral states (i.e., inversely related to the spectral widths) increase monotonically with wall density. This implies a monotonic increase of the reflection probability P_{R} with increasing ρ_{wall}. Accepting that the interaction of surface-state electrons with the corral wall includes lossy absorption channels, an increase in ρ_{wall} also suggests an increase in the number of such lossy absorption channels[2] (increase in the number of scatterers), and therefore a monotonic increase of the absorption probability P_{A}. These relations – the monotonic decrease of P_{T} from 100% with increasing ρ_{wall}, the monotonic increase of both P_{R} and P_{A}, and the constraint that the sum of all probabilities equals 100% – are illustrated schematically in Fig. 5.12. Within this simplified framework, two notable observations can be made. First,

[1] Here, the term "lossy" refers to processes in which an electron leaves the corral state it currently occupies. This can occur, for example, via scattering into bulk states (i.e., leaving the Shockley surface state) or via tunneling through the corral wall, where no confined corral states exist.
[2] It is assumed here that each CO molecule in the wall of the corral opens a lossy absorption channel for electrons. As a result, the number of lossy absorption channels increases with the number of CO molecules in the wall.

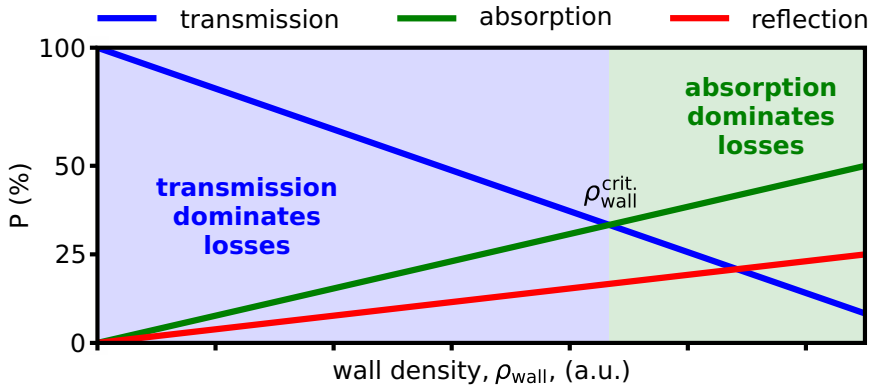


Figure 5.12: Schematic illustration of the three possible interactions for a surface-state electron at the corral wall: reflection (P_R), transmission into the surrounding surface state (P_T, lossy), and absorption (P_A, lossy). The sum of all probabilities is $P_R + P_T + P_A = 100\%$. Experimental results show that the corral state lifetimes increase with increasing wall density ρ_{wall}, which is consistent with an increasing reflection probability. At a critical wall density $\rho_{wall}^{crit.}$, the probabilities for transmission and absorption are equal. The linear dependence of the probabilities on ρ_{wall} is used purely for illustrative purposes. The actual functional forms and slopes are unknown. Both scenarios — absorption exceeding reflection (as shown) or vice versa — are therefore possible. Nevertheless, the experimental trends require that the transmission probability decreases more rapidly with increasing wall density than the absorption probability increases.

beyond a critical wall density $\rho_{wall}^{crit.}$, the dominant lossy channel changes from lateral transmission to absorption at the corral wall. Second, the transmission probability must be more sensitive to variations in ρ_{wall} than the absorption probability.

Several theoretical approaches in the literature offer different perspectives on the dominant lifetime-limiting process in quantum corrals. Some studies identify coupling to bulk states (absorption) as the primary mechanism [24, 97, 129], while others, such as the work by García-Calderón and Chaos-Cador [131], suggest that coherent processes like tunneling (transmission) play a more significant role. In contrast, some theoretical treatments rely entirely on elastic scattering mechanisms without introducing bulk coupling [132, 133]. Taking these theoretical considerations together with the experimental observations presented here, one can propose that corrals with low wall density operate in a regime where transmission dominates the lifetime limitation, whereas for corrals with high wall density, an absorptive loss channel, commonly associated with coupling to bulk states, becomes dominant. Within the scope of this work, the critical wall density $\rho_{wall}^{crit.}$ cannot be determined.

5.4.2. Gaussian spectral line shape

In the following, three possible mechanisms that could explain the Gaussian spectral line shape are discussed: (1) a non-exponential survival probability of electrons, originating from scattering at the corral wall, (2) an electron-phonon coupling to a collective vibrational mode of the boundary, called the breathing mode, and (3) a direct modulation of the corral-state energies caused by that breathing mode.

Non-exponential survival probability from scattering at the wall Previous studies of quantum corrals have predominantly described the spectral line shapes of confined surface-state electrons by Lorentzian functions (e.g., Refs. [79, 128, 134, 135]). A Lorentzian line shape corresponds to an exponential decay of the survival probability in the time domain, which implies that electrons inside the corral experience a uniform decay probability at any given moment in time. Such a description is appropriate when the dominant lifetime-limiting mechanism acts homogeneously in time and space.

The results presented in this work, however, indicate that the dominant mechanism limiting the lifetime of corral states is the interaction of confined electrons with the corral wall. This fundamentally changes the nature of the decay process: Instead of experiencing a uniform decay probability, electrons predominantly "leave" the corral state at interaction events with the boundary. As a consequence, the survival probability of an electron inside the corral is not expected to decay exponentially in time, and a non-Lorentzian spectral line shape emerges. To illustrate this effect, a semiclassical single-particle model is considered in which an electron propagates freely inside the corral and interacts with the wall only once before leaving the corral state through a lossy channel (absorption or transmission).

The measurements reported in Section 5.1 were performed with tunneling currents below $\approx 500\,\mathrm{pA}$, corresponding to one electron tunneling every $\approx 320\,\mathrm{ps}$. This is several orders of magnitude longer than the lifetimes inferred from the measured spectral widths, which are typically on the order of tens of femtoseconds[1]. This suggests that the observed line shapes are intrinsic properties of the corral states and are negligibly influenced by the tip position and the tunneling electrons. Con-

[1] A spectral width of $\Gamma = 45\,\mathrm{meV}$, which is approximately the width of the peaks of the big 48-CO corral around the Fermi energy, corresponds via $T_{\mathrm{life}} = \hbar/\Gamma$ to a lifetime of about 15 fs.

sequently, the corral wall can be used as a reference point and thus defines a set of possible path lengths and corresponding travel times for electrons, as shown schematically in Fig. 5.13(a)-(c).
Assuming equal probability for all paths, the resulting survival probability is obtained by mapping the travel times, leading to the curve shown in Fig. 5.13(d). The resulting survival probability clearly deviates from an exponential decay, which results in a non-Lorentzian peak shape in the energy domain.
This simple framework demonstrates that a wall-limited decay mechanism alone is sufficient to qualitatively explain the observed deviation from Lorentzian behavior. Although the inclusion of multiple scattering events could lead to peak shapes resembling a Gaussian distribution in the energy domain, such an extension is beyond the scope of this work and is reserved for future theoretical studies.

Electron-phonon coupling to a collective boundary mode Gaussian spectral line shapes have been reported previously in other confined systems, such as quantum dots [136] and defects in salt layers [137], where they were attributed to a strong coupling between electrons and a phonon mode of the nanostructure itself. In the context of quantum corrals, a plausible candidate for such a phonon mode is a coherent radial motion of the corral wall, also referred to as a breathing mode. Although a direct interaction between neighboring CO molecules can be neglected due to their large separation (e.g., 938 pm in the 48-CO corral), adsorbates on metal surfaces are known to interact over long distances through the surface state (e.g., Refs. [138–141]). The radially symmetric corral states may induce a coherent motion of the CO molecules, enabling a collective phonon mode of the corral boundary. In the regime of strong electron-phonon coupling, this coherent motion might provide an explanation for the Gaussian shapes observed in the energy distributions. While a more rigorous computational approach addressing this phenomenon would be beneficial, this remains outside the scope of this work.

Direct modulation of corral state energies by boundary motion The existence of a breathing mode could also directly influence the energy of the corral states. A modulation of the corral radius due to radial motion of the wall would shift the energy positions of the confined states: Reducing the radius ($R_C - \Delta R_C$) increases the energy, while increasing the radius ($R_C + \Delta R_C$) lowers it. A continuous variation

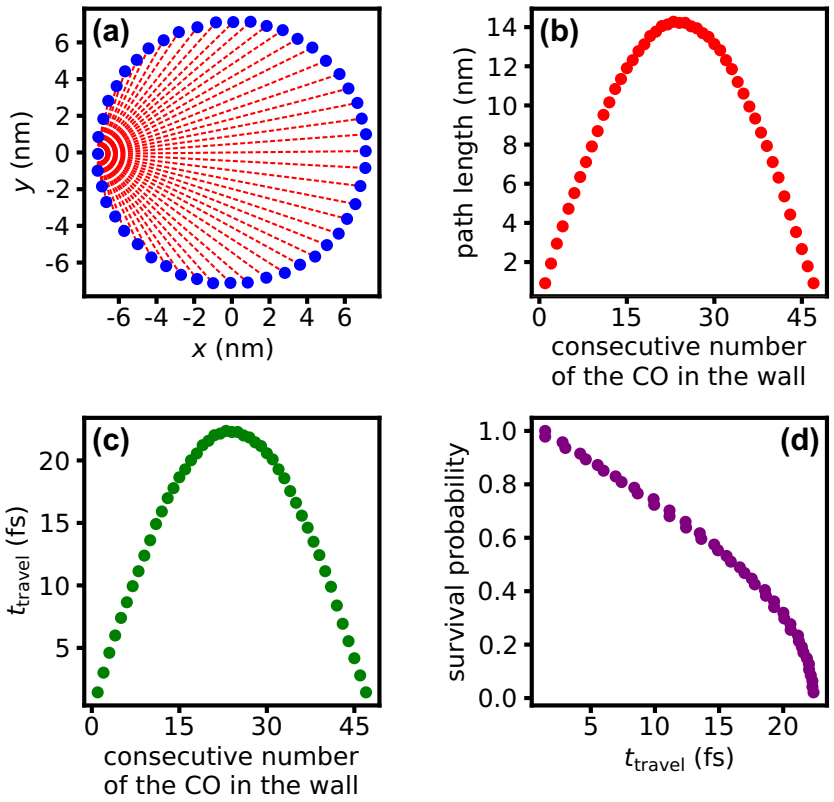


Figure 5.13: (a): The blue markers give the position of the CO molecules in the big 48-CO corral. The red dashed lines indicate the possible paths an electron can take when starting at the wall. (b): The possible path lengths from panel (a). (c): Traveling times t_{travel} of an electron at the Fermi energy, corresponding to the path lengths in panel (b). (d): Survival probability curve translated from panel (c), considering only one scattering event. The non-exponential shape in the time domain results in a non-Lorentzian peak shape in the energy domain.

of the radius would therefore lead to a broadening of the measured spectral peaks. According to the hard wall model [see Eq. (3.7)], the energy difference introduced by the breathing mode at the extreme positions ($R_\mathrm{C} \pm \Delta R_\mathrm{C}$) is

$$\Delta E_\mathrm{breathing} = (E_{n,l}^\mathrm{circ} + 440\,\mathrm{meV}) \cdot \left[\frac{R_\mathrm{C}^2}{(R_\mathrm{C} - \Delta R_\mathrm{C})^2} - \frac{R_\mathrm{C}^2}{(R_\mathrm{C} + \Delta R_\mathrm{C})^2} \right]. \tag{5.9}$$

Here, $E_{n,l}^\mathrm{circ}$ denotes the energies of the unmodulated corral states, as introduced in Subsection 3.2.2.

To fully account for the spectral widths reported in Figs. 5.8 and 5.11(a) via this mechanism, radial amplitudes of approximately 200 pm would be required. This estimate is based on the peak widths of the big 48-CO corral near the Fermi level, which are approximately 45 meV. Since 200 pm exceeds the radius of a copper atom (132 pm), and no laterally displaced CO molecules were observed during the measurements, it can be concluded that breathing-induced energy modulation cannot be the dominant broadening mechanism.

The requirement of such a large amplitude suggests that the breathing mode may only contribute partially to the observed spectral widths. To estimate its realistic contribution, the established positional uncertainty of an isolated CO molecule can be used, which can be approximated by a Gaussian FWHM of about 33 pm [142]. Interpreting this uncertainty as a fluctuation in the corral radius yields an estimated Gaussian broadening of 4.1 meV for states at the Fermi energy (440 meV above the band edge). For higher-energy states located 400 meV above the Fermi level, the broadening increases to approximately 7.8 meV. Thus, even such a small coherent adsorbate motion of a few tens of picometers is expected to contribute non-negligibly to the measured energy distributions.

In conclusion, it is proposed that the overall Gaussian line shape arises from a combination of three effects: (1) non-exponential survival probability originating from wall-limited scattering, (2) electron-phonon coupling to a collective boundary mode, and (3) the direct modulation of corral state energies by the collective boundary motion.

5.5. Summary and Outlook

Summary

In this chapter, the spectral properties of quantum corral states were investigated using scanning tunneling spectroscopy. Two circular quantum corrals were constructed on Cu(111) with different radii (7.13 nm and 3.57 nm) but identical wall densities. By comparing the measured local density of states (LDOS) with a linear combination of probability densities obtained from a hard wall model, the energy distributions of individual corral states, including states with $l \neq 0$, were determined. Analysis of the energy distributions revealed that the line shape of all observed states is best described by a Gaussian function rather than a Lorentzian. In addition, a clear correlation was found between the size of the corral and the spectral width: Larger corrals host states with narrower energy distributions, while smaller corrals lead to broader energy distributions. This indicates that the dominant limitation of the state lifetime originates from the interaction of the confined electrons with the corral wall.

On the basis of this observation, a classical model was introduced to relate the spectral widths of the corral states to the average path length of a surface-state electron. The model quantitatively captures the experimentally observed energy dependence of the spectral widths and allows the lifetime of corral states to be characterized by a single parameter.

To further characterize the electron-wall interaction, quantum corrals with varying wall densities were constructed. The measured spectral widths decrease systematically with increasing wall density, demonstrating that denser boundaries support corral states with longer lifetimes. This behavior indicates that increasing the wall density suppresses lateral transmission through the corral wall more strongly than it affects the coupling of corral states to bulk electronic states at the boundary.

Finally, three mechanisms were considered to explain the observed Gaussian line shape of the corral state energy distributions. While previous studies commonly describe the energy distributions of corral states using Lorentzian functions, implying an exponential decay of the electron survival probability, the results presented in this work suggest that the wall interaction dominates the lifetime limitation. This lifetime limitation due to electron-wall interaction leads to a non-exponential

survival probability and, consequently, to non-Lorentzian spectral profiles. In addition, literature reports Gaussian line shapes in systems where electrons are strongly coupled to phonon modes [136, 137]. In the present system, a plausible candidate is a collective breathing mode of the corral wall, corresponding to a coherent radial motion of the CO molecules. Such a mode can also contribute to Gaussian broadening both through electron-phonon coupling and through a direct modulation of the corral radius. Although the estimated magnitude of the radius modulation alone cannot fully account for the observed widths, it is likely to represent a contributing mechanism to the overall Gaussian line shape.

Outlook

Recent research has demonstrated that the lifetimes of laterally confined field-emission resonances can be prolonged by increasing the lateral extent of the confining potential or the vertical confinement [143]. The results presented in this thesis demonstrate that a similar lifetime enhancement can be achieved for adsorbate-based quantum corrals confining the Shockley surface state, either by increasing the corral radius (see Fig. 5.8) or by increasing the wall density (see Fig. 5.11). Building on these findings, several strategies can be considered to further increase the lifetime of quantum corral states.

A first approach is to further suppress lateral transmission through the corral wall. The systematic variation of the wall density presented in this work reveals an approximately order-of-magnitude change in the average electron path length. Extrapolating the observed trend in Fig. 5.11(b) suggests that a hypothetical wall allowing nearest-neighbor occupation on every Cu adsorption site could yield an average path length of approximately 16 nm. While such a density cannot be realized with CO molecules, the effective wall thickness could be increased by constructing multi-row boundaries, for example using double- or triple-row CO walls. Using this approach, it may be possible to suppress the lifetime-limiting effects of transmission (tunneling) so significantly that the spectral widths become primarily dominated by electron-electron scattering, electron-phonon interactions, and coupling to the bulk.

A second route to lifetime enhancement involves modifying the vibrational properties of the corral boundary. As discussed in Subsection 5.4.2, part of the observed Gaussian broadening is likely related to the vibrational motion of the CO molecules

forming the wall. The use of adsorbates that exhibit a reduced vibrational amplitude in comparison to that of CO could serve to mitigate this effect (for instance, adsorbates that are more rigidly bound to the surface).
Finally, reducing the coupling of corral states to bulk states represents a promising strategy for further lifetime enhancement. As shown in Subsection 5.4.1, bulk coupling becomes increasingly relevant at high wall densities and can ultimately limit the achievable lifetime. The use of alternative adsorbates with weaker bulk coupling [127, 144] could minimize this effect. Additionally, the influence of bulk coupling may be further reduced by carefully choosing the substrate material. While significant progress has already been demonstrated on semiconductor substrates [28], layered two-dimensional materials may provide an especially attractive platform for realizing long-lived corral states in future experiments.

6. Characterizing the decay lengths of interatomic forces

Most of the work presented in this chapter has been published in Physical Review B [145]. Parts of the text and figures are reproduced from this publication. All experiments, data analyses, and modeling were carried out by the author.

This chapter investigates the interaction between an AFM tip and the confined Shockley surface state inside a quantum corral on Cu(111). Section 6.1 presents constant-height AFM measurements inside square quantum corrals and analyzes the distance dependence of the attractive and repulsive tip-corral interactions. The robustness of the extracted decay lengths with respect to tip configuration and corral wall density is also examined.

To interpret these observations, Section 6.2 introduces a model of Pauli repulsion and examines the attractive metal-tip interaction within the chemical-attraction picture proposed by Stilp *et al.* [17]. Based on these results, Section 6.3 compares the experimentally observed decay length ratio with the ratio assumed in the Morse potential. Finally, Section 6.4 relates the measured decay lengths to interactions between two natural atoms in order to clarify why both attractive and repulsive interactions are longer ranged in the quantum corral system.

6.1. AFM measurements inside quantum corrals

The analysis of the distance-dependent tip-corral interaction begins with a square quantum corral, constructed from 26 individually positioned CO molecules. A constant-current STM image of this structure is shown in Fig. 6.1. The side lengths of the corral are $L_x = 6.13\,\mathrm{nm}$ and $L_y = 6.20\,\mathrm{nm}$. The intermolecular distance along the upper and lower walls is 1020 pm, whereas along the left and right walls it is 885 pm. A detailed construction plan, including the precise adsorption sites of the CO molecules, is provided in Appendix A.1.

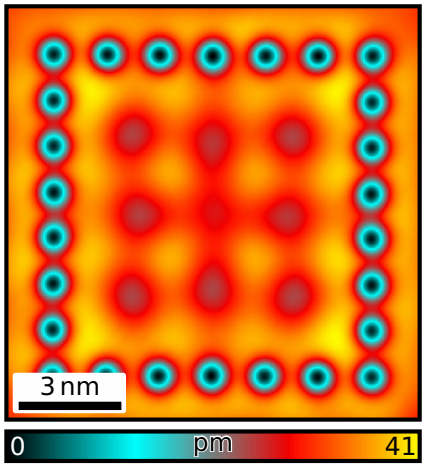


Figure 6.1: Constant-current STM image of the square quantum corral consisting of 26 CO molecules. The image was acquired with a metal-tip at a sample bias of 10 mV and a tunneling current setpoint of 100 pA. The side lengths are $L_x = 6.13$ nm and $L_y = 6.20$ nm. The checkerboard-like structure inside the corral reflects the confined surface-state electron density near the Fermi level.

6.1.1. Constant-height AFM images and the total surface charge density

This subsection illustrates how the AFM contrast observed inside the square quantum corral reflects the spatial variation of the total surface charge density [17]. Figure 6.2(a) shows a constant-height AFM image acquired inside the quantum corral using a CO-terminated tip. All AFM measurements presented in this chapter were performed with a sample bias of $V = 0$ mV to suppress the tunneling current and thus avoid cross-coupling between the STM and AFM detection electrodes of the qPlus sensor [60].

The image in Fig. 6.2(a) was recorded at a tip-sample separation of 340 pm. At this small separation, using a CO-functionalized tip, the Cu surface atoms appear as small attractive (dark) features, consistent with previous high-resolution AFM studies [30, 146]. Superimposed on the atomic lattice, broader spatial features are visible. These originate from the confined Shockley surface state inside the corral. The pattern consists of four bright regions around the center, surrounded by eight light-dark features. To enhance the visibility of this long-wavelength pattern, a Gaussian low-pass filter was applied to suppress the high-spatial-frequency contributions of the Cu lattice [17]. Details of the filtering procedure are provided

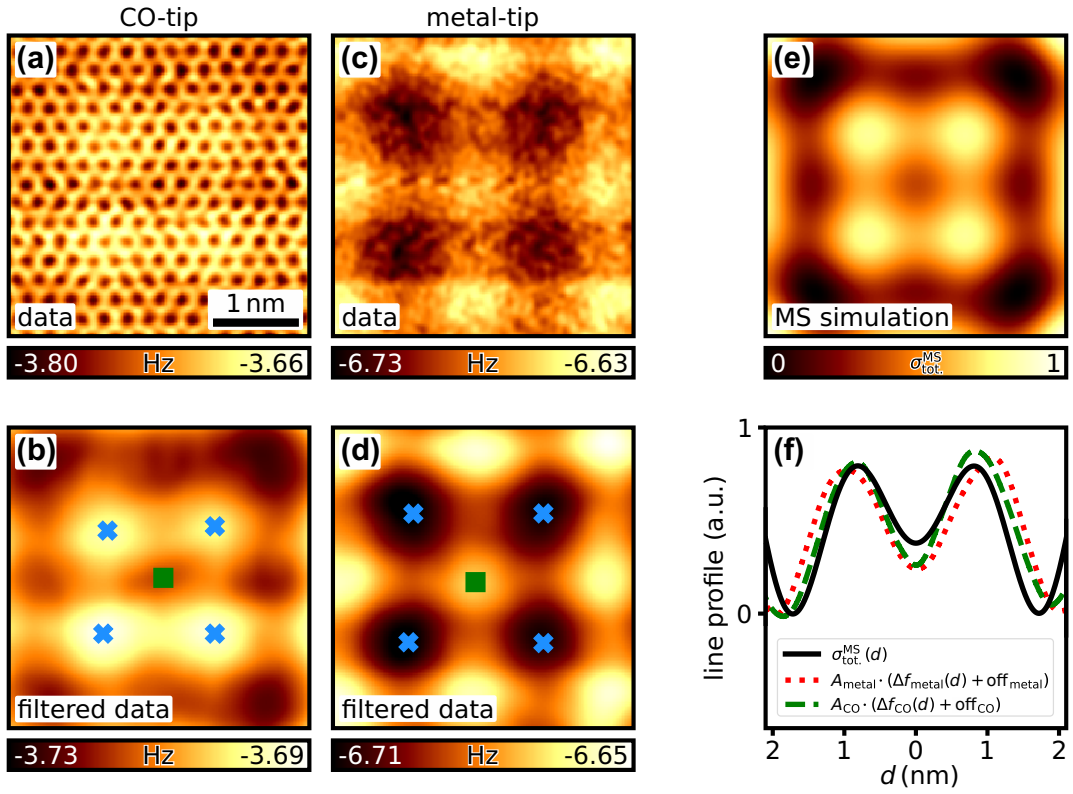


Figure 6.2: (a): Constant-height frequency shift image acquired with a CO-tip inside the square corral. Cu surface atoms appear as small dark features. The confined surface state manifests as four bright regions around the center, surrounded by eight light-dark features. (b): Gaussian low-pass filtered version of (a) in order to suppress the Cu grid [17]. (c): Constant-height frequency shift image acquired with a monoatomic metal-tip inside the square corral. The confined surface state is visible as four dark spots around the center of the image, surrounded by eight bright spots. (d): Gaussian low-pass filtered version of (c). (e): Multiple scattering (MS) simulation of the total surface charge density $\sigma_{\text{tot}}^{\text{MS}}$. Bright (dark) regions correspond to a high (low) charge density. (f): Averaged diagonal line profiles extracted from (b) and (d), compared to the simulated profile from (e). The horizontal axis d is the distance from the center of the corral. For a qualitative comparison, an offset of $\text{off}_{\text{CO}} = 3.73\,\text{Hz}$ was added and the result was multiplied by a scaling factor of $A_{\text{CO}} = 31\,\frac{\text{a.u.}}{\text{Hz}}$: $A_{\text{CO}} \cdot (\Delta f_{\text{CO}} + \text{off}_{\text{CO}})$. The red dotted line represents the corresponding averaged line profile from the metal-tip AFM image in (d). Similar to the CO-tip case, the line profile is scaled by using $\text{off}_{\text{metal}} = 6.65\,\text{Hz}$ and $A_{\text{metal}} = -14.7\,\frac{\text{a.u.}}{\text{Hz}}$. The solid black line shows the simulated profile extracted from (e).

in Appendix A.4. The filtered image is shown in Fig. 6.2(b).
A comparison between measurements obtained with CO- and metal-tips provides direct insight into how the sign of the tip-corral interaction depends on the tip termination. When the same region inside the square quantum corral is imaged with a monoatomic metal-tip, the contrast is inverted [see Fig. 6.2(c,d)]. Regions that appear bright with the CO-tip appear dark with the metal-tip. This contrast inversion has previously been reported by Stilp *et al.* [17]. For metal-tips, regions of enhanced total surface charge density σ_{tot} correspond to a stronger attractive interaction, which was interpreted by Stilp *et al.* as chemical attraction [17], whereas CO-tips exhibit increased repulsion. The latter was attributed to Pauli repulsion [17].
To relate the observed AFM contrast to the total surface charge density inside the square quantum corral, the spatial variation of the total surface charge density has to be modeled. In principle, this can be done within the hard wall framework. To achieve a realistic simulation within this framework, a complete spectroscopic analysis of the corral states must be carried out to determine the energy distributions of the corral states. This would be comparable to what was described in Chapter 5 for the circular corrals. Since such an extensive characterization is not the aim of this chapter, multiple scattering (MS) simulations are employed. The MS formalism, developed by Heller *et al.* [24], treats surface adsorbates as δ-like s-wave scatterers and is widely used to describe the electronic properties of quantum corrals. The best agreement with experiment is obtained in the so-called "black-dot" limit, where the scatterers include a strong absorbing channel [24]. The MS formalism provides the spatially resolved local density of states as a function of the electron energy. By integrating the simulated LDOS from the band edge of the Shockley surface state up to the Fermi energy, a measure of the total surface charge density σ_{tot} is obtained.
The simulations showed that the confined surface-state electrons exhibit an effective mass $m^*_{\mathrm{e,conf.}}$ slightly higher than that of free surface-state electrons $m^*_{\mathrm{e,free}}$. The best agreement between simulation and measurement was found for $m^*_{\mathrm{e,conf.}} = 0.45 \cdot m_{\mathrm{e}}$, while the effective mass of the free Shockley surface state is $m^*_{\mathrm{e,free}} = (0.405 \pm 0.025) \cdot m_{\mathrm{e}}$ (e.g., Refs. [15, 47, 69–73]). Details about the determination of the effective mass are given in Appendix A.5. A slight increase in the effective mass of confined electrons is a known phenomenon and has also been observed, for example, in semiconductor quantum dots [147]. Furthermore, Freeney *et al.* [82] simulated

square-shaped quantum corrals on Cu(111) using a muffin-tin model and reported effective masses of $0.48 \cdot m_e$ and $0.46 \cdot m_e$, which are in good agreement with the value obtained here. The effective mass was determined to ensure a consistent description between simulation and experiment, but it is not central to the analysis presented in this thesis and will therefore not be discussed further.
The simulated total surface charge density σ_{tot}^{MS} for the square quantum corral is shown in Fig. 6.2(e). Bright regions correspond to a higher total surface charge density, whereas dark regions correspond to a lower surface charge density.
Comparing the filtered AFM image obtained with the CO-tip [Fig. 6.2(b)] with the simulated surface charge density [Fig. 6.2(e)] shows that regions of increased surface charge density correspond to regions of increased repulsive contrast in the AFM image. The opposite behavior is observed for measurements with a metal-tip. In this case, regions of higher surface charge density correspond to a stronger attractive contrast, which appears dark in the AFM image [Fig. 6.2(d)]. Figure 6.2(f) shows the average line profiles along the two diagonals of the respective images. For a qualitative comparison between measurement and simulation, an offset was added to the measured line profiles and subsequently multiplied by a scaling factor. The values are provided in the caption of Fig. 6.2. For the metal-tip measurement, the scaling factor is negative, effectively inverting the profile. This reflects the inverted contrast observed with a metal-tip.
It is worth noting that the maxima of the line profiles in Fig. 6.2(f) are slightly further apart for the metal-tip measurement than for the CO-tip measurement. Specifically, the maxima are separated by 2 nm for the metal-tip and by 1.7 nm for the CO-tip. Previously, it has been reported that the close proximity of an AFM tip can shift the energy of the corral states [17]. CO-tips were reported to increase the energy of the corral states slightly, leading to a small depopulation of states near the Fermi level, whereas metal-tips slightly lower the energy of the states, and thereby increase the electron population.
Such tip-induced energy shifts alter the total surface charge density, which can explain the subtle differences both among the measured AFM profiles themselves and between the experimental profiles and the MS simulations. In addition, the simulated total surface charge density may deviate slightly from the experiment because the band edge of the Shockley surface state was chosen to be -440 meV below the Fermi level, a value that varies slightly in the literature.

Overall, the qualitative agreement between AFM measurements and MS simulations demonstrates that the measured frequency shift signal reflects the spatial variation of the total surface charge density inside the quantum corral. This supports the contrast behavior of AFM measurements in corrals reported by Stilp *et al.* [17].

6.1.2. Distance dependence of attractive and repulsive interactions

The observations and considerations discussed above were based on AFM images recorded at a specific tip-sample separation. However, recording constant-height AFM images at different tip-sample distances provides additional insight into the distance dependence of the interaction between the probe tip and the corral states. The evolution of the frequency shift contrast $C^{\Delta f}$ as a function of the tip-sample distance z is shown in Fig. 6.3. Each data point of $C^{\Delta f}$ in Fig. 6.3 is extracted from a single AFM image. The contrast is defined as the average absolute difference between the four innermost extrema, marked by blue crosses, and the center of the corral, marked by the green square [see Fig. 6.2(b) and (d)]. The maximum and minimum values obtained from these extrema define the error bars.
It should be emphasized that the total span of the error bars (from minimum to maximum) is nearly the same for both the CO-tip and metal-tip measurements. The apparent difference in their size originates from the much smaller contrast signal observed in the CO-tip data.
The frequency shift contrast decays exponentially with increasing tip-sample separation for both the CO-tip and the metal-tip. The extracted decay lengths are $\lambda_{\mathrm{CO}}^{\mathrm{repul.}} = (48 \pm 11)\,\mathrm{pm}$ and $\lambda_{\mathrm{metal}}^{\mathrm{attr.}} = (65 \pm 6)\,\mathrm{pm}$. For CO-tip measurements, no attractive force contrast was observed. The interaction contrast remained purely repulsive. As discussed in Section 2.1, an exponential dependence of the frequency shift contrast entails that the corresponding force contrast C^F also follows an exponential behavior [35]. The force contrasts are therefore given by $C^F_{\mathrm{CO}}(z) = 291\,\mathrm{fN} \cdot \exp[-(z - 323\,\mathrm{pm})/\lambda_{\mathrm{CO}}^{\mathrm{repul.}}]$ for the CO-tip measurements and $C^F_{\mathrm{metal}}(z) = 1522\,\mathrm{fN} \cdot \exp[-(z - 417\,\mathrm{pm})/\lambda_{\mathrm{metal}}^{\mathrm{attr.}}]$ for the metal-tip measurements. These expressions show that at the smallest tip-sample separations (323 pm for the CO-tip and 417 pm for the metal-tip) force contrasts of 291 fN and 1522 fN were measured. The force contrasts are displayed as solid red lines in Fig. 6.3.

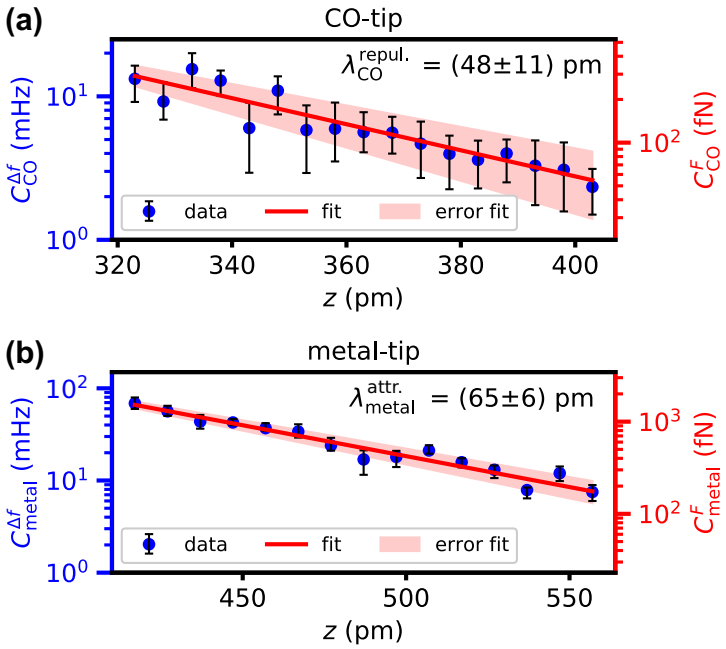


Figure 6.3: (a): Frequency shift contrast $C_{CO}^{\Delta f}$ measured with a CO-tip as a function of the tip-sample distance z. An exponential behavior is observed with a decay length of $\lambda_{CO}^{repul.} = (48 \pm 11)$ pm. The contrast is defined as the difference between the average of the four innermost maxima and the central minimum of one constant-height AFM image. (b): Frequency shift contrast $C_{metal}^{\Delta f}$ measured with a metal-tip, yielding a decay length of $\lambda_{metal}^{attr.} = (65 \pm 6)$ pm. Here the contrast is defined as the average difference between the central maximum and the four innermost minima. In both cases the frequency shift contrast was fitted with an exponential decay function (solid red lines). The corresponding force contrasts are shown on the right axis. The red shaded regions indicate twice the standard deviation of the fits and the definition of the data point error bars is given in the main text.

	$\lambda_{\mathrm{CO}}^{\mathrm{repul.}}$ (pm)	$\lambda_{\mathrm{metal}}^{\mathrm{attr.}}$ (pm)
Corral 1 (Figs. 6.1-6.3)	48 ± 11	65 ± 6
Corral 2 (Appendix A.6)	40 ± 13 39 ± 14	67 ± 8
Denser corral (Fig. 6.4)	51 ± 9	68 ± 13
Average	46 ± 6	66 ± 5

Table 6.1: Decay lengths of the AFM contrast measured with CO- and metal-tips for different quantum corrals and tip configurations. Corral 1 was first measured with a monoatomic metal-tip and subsequently with a CO-terminated tip (same metal-tip background but equipped with a CO at the apex). Corral 2 was constructed after several preparation cycles on the same copper sample and measured with a different mesoscopic tip configuration. For the CO-tip measurements of corral 2, the measurement and analysis were repeated to verify reproducibility. The denser corral was measured using the same tips as for corral 1.

While the decay lengths obtained from Fig. 6.3 already provide a first estimate of the distance dependence of the probed interactions, it is important to verify that these values are not specific to a particular tip configuration or quantum corral. To improve the reliability and accuracy of the extracted decay lengths and test their robustness against experimental variations, additional measurements were performed with different tips in a separate quantum corral[1]. The corresponding analysis is presented in Appendix A.6 and summarized in Table 6.1. The obtained decay lengths are consistent within experimental uncertainty, demonstrating that the decay length of the interaction between the corral states and the probe tip is independent of the mesoscopic tip geometry and the local environment of the quantum corral.

The negligible influence of the mesoscopic tip geometry can also be estimated quantitatively. Because the interaction between the tip and the corral states decays exponentially on a length scale of a few tens of picometers, the dominant contribution originates from the frontmost atom of the tip apex. For a monoatomic metal-tip, the atoms in the second layer are located approximately 200 pm further away from the

[1]While both measurement series were carried out on the same sample, the sample underwent multiple sputtering and annealing cycles between the two sessions. Moreover, the mesoscopic tip configuration was not identical. In the period separating the two experiments, the tip apex was altered several hundred times via pokes.

surface. With a decay length of 66 pm, their contribution to the force amounts to only about 5% of that of the apex atom. Consequently, the mesoscopic tip geometry has only a negligible influence on the measured force contrast.

In Chapter 5, it was shown that the electronic properties of corral states depend on the wall density. A higher wall density increases the lifetime of the confined states. However, the decay of the corral states towards the vacuum should not be affected by this parameter. To verify this experimentally, AFM measurements were also performed in a corral with twice the wall density of the one presented in Fig. 6.1. The construction plan of this denser square corral is provided in Appendix A.1. Applying the same analysis as for the less dense corral yields very similar decay lengths of (51 ± 9) pm for the repulsive force and (68 ± 13) pm for the attraction. The values are summarized in Table 6.1 and the corresponding analysis is shown in Fig. 6.4.

As is evident from Table 6.1, the measured decay lengths remain identical within the experimental uncertainty, independent of the mesoscopic tip geometry, the environment of the corral, or the density of the corral wall. This motivates the introduction of a quantitative relationship between the decay lengths of the attractive interaction with a metal-tip and the repulsive interaction with a CO-tip:

$$\lambda_{\text{metal}}^{\text{attr.}} = (1.4 \pm 0.2) \cdot \lambda_{\text{CO}}^{\text{repul.}}. \tag{6.1}$$

This relation shows that, for quantum corrals on Cu(111), the decay lengths of the measured attractive and repulsive interactions differ by a factor of 1.4.

As discussed in Subsection 6.1.1, the close proximity of the probe tip can slightly shift the energies of the corral states. Such shifts can modify the occupation of states near the Fermi level and thereby influence the total surface charge density. In principle, this effect could alter the distance dependence of the frequency shift contrast. As shown in Chapter 5, corral states in denser structures have longer lifetimes and therefore narrower energy distributions, making their total surface charge densities more sensitive to tip-induced energy shifts. Since both dense and less dense corrals yield identical decay lengths within the experimental uncertainty (see Table 6.1), the influence of this effect can be considered negligible.

It is well known that the CO molecule at the apex of an AFM tip is flexible and can bend laterally during scanning. This bending can even enhance the spatial

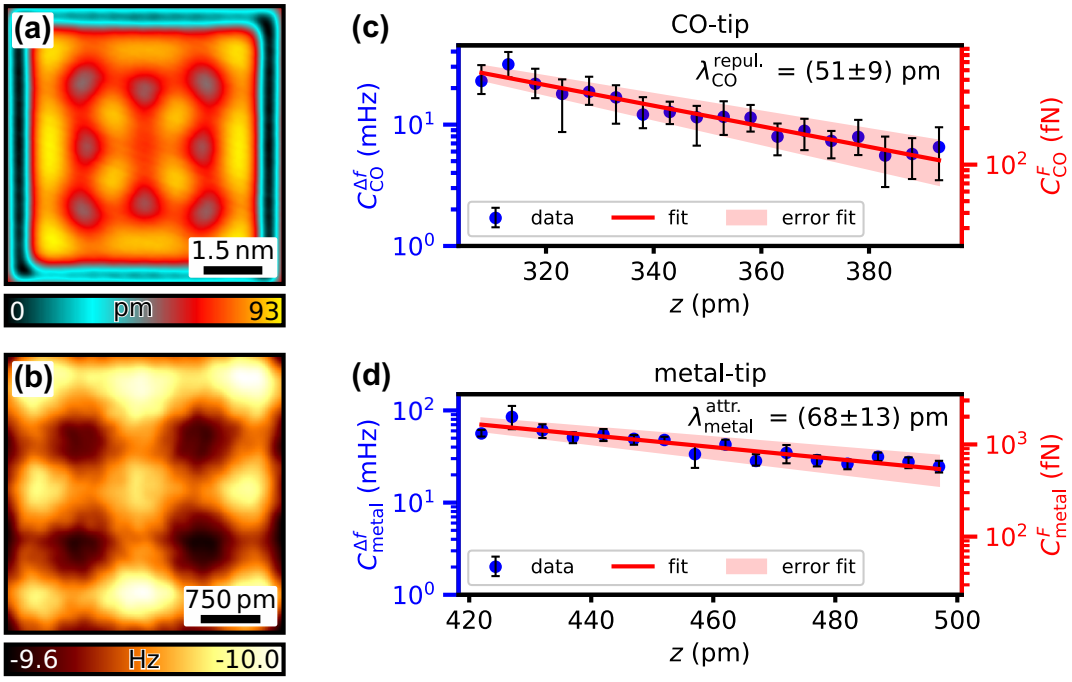


Figure 6.4: (a): Constant-current STM image of the denser square quantum corral, consisting of 52 CO molecules, measured with a metal-tip at a sample bias of −10 mV and a tunneling current setpoint of 100 pA. The corral has side lengths of 6.13 nm in the horizontal direction and 6.20 nm in the vertical direction. (b): Constant-height frequency shift image acquired with a metal-tip inside the quantum corral. (c) and (d): Frequency shift and corresponding force contrast measured with a CO-tip and a metal-tip as a function of the tip-sample distance z. Both measurements show an exponential distance dependence with decay lengths of $\lambda_{CO}^{repul.} = (51 \pm 9)$ pm and $\lambda_{metal}^{attr.} = (68 \pm 13)$ pm. The extracted decay lengths are consistent with those obtained for the less dense corral.

resolution when imaging molecules on surfaces [115]. However, since the analyzed frequency shift and force contrasts presented in this thesis were calculated based on local extrema, and consequently no lateral force was acting on the CO-tips at those points, the influence of CO bending on the reported decay lengths can be considered negligible. Nevertheless, to obtain a better understanding of AFM measurements inside quantum corrals, it is instructive to provide a rough estimate of the CO bending amplitude that occurs during measurements in the corral.

Due to the exponential dependence of the force contrast, the corresponding potential energy contrast C^V_{CO} at the smallest tip-sample separation z_{min} is given by

$$C^V_{\mathrm{CO}}(z_{\mathrm{min}}) = C^F_{\mathrm{CO}}(z_{\mathrm{min}}) \cdot \lambda^{\mathrm{repul.}}_{\mathrm{CO}}. \tag{6.2}$$

Using the values discussed above [$C^F_{\mathrm{CO}}(z_{\mathrm{min}} = 323\,\mathrm{pm}) = 291\,\mathrm{fN}$ and $\lambda^{\mathrm{repul.}}_{\mathrm{CO}} = 48\,\mathrm{pm}$], one obtains a potential energy contrast of $C^V_{\mathrm{CO}}(323\,\mathrm{pm}) = 14\,\mathrm{yJ} = 87\,\mu\mathrm{eV}$. This corresponds to the potential difference between the center of the corral and the outer extrema of the interaction landscape. To estimate the lateral force acting on the CO molecule, the lateral gradient of this potential is considered. The lateral distance between the center of the corral and these extrema is approximately 1 nm. As a first-order approximation, it is assumed that the potential energy landscape changes linearly between the center and the outer extrema. The lateral force is then

$$F^{\mathrm{lat.}}_{\mathrm{CO}} = \frac{14\,\mathrm{yJ}}{1\,\mathrm{nm}} = 14\,\mathrm{fN}. \tag{6.3}$$

With a lateral stiffness of a CO molecule on a metal-tip of $k^{\mathrm{lat.}}_{\mathrm{CO}} = 0.24\,\mathrm{N/m}$ [148], this force results in a lateral deflection of

$$\Delta x = \frac{F^{\mathrm{lat.}}_{\mathrm{CO}}}{k^{\mathrm{lat.}}_{\mathrm{CO}}} = 58\,\mathrm{fm}. \tag{6.4}$$

Compared to the approximate distance between the frontmost oxygen atom and the metal atom of the tip apex ($\approx 300\,\mathrm{pm}$), this deflection is negligible.

The observed decay lengths of the repulsive and attractive interactions therefore represent robust quantities that are independent of the specific mesoscopic tip geometry, local environment, and wall density of the quantum corral.

Stilp *et al.* [17] were the first to investigate circular quantum corrals using AFM and

interpreted the attractive interaction between the confined Shockley surface state and a metal-terminated AFM tip as a chemical interaction. They reported attractive decay lengths of 56 pm and 51 pm for two circular Fe corrals on Cu(111): a larger corral with a radius of 7.13 nm consisting of 48 Fe adatoms and a smaller corral with a radius of 3.57 nm consisting of 24 Fe adatoms. Both corrals had the same wall density, which is very close to that of the less dense square corral investigated in this thesis. However, no uncertainties are given regarding the reported decay lengths. In contrast to the measurements presented in this thesis, Stilp *et al.* did not report a similarly systematic analysis of repeated measurements for different tip configurations and corrals. If one assumes uncertainties of similar magnitude to those obtained here, i.e., on the order of ± 10 pm, the decay lengths reported by Stilp *et al.* are compatible with the values presented in this thesis (see Table 6.1).
In addition to possible systematic experimental uncertainties, such as thermal drift or small deviations in the z-calibration, another effect may contribute to the slightly smaller values reported in Ref. [17]. As shown in the same publication, the close proximity of a metal-tip shifts corral states downward in energy. Such tip-induced energy shifts modify the occupation of states close to the Fermi energy and thereby alter the local density of states and the total surface charge density inside the corral. As a consequence, the measured decay length of the contrast is influenced not only by the distance dependence of the force itself, but also by the tip-induced modification of the electronic structure. This effect may therefore have contributed slightly to the extracted decay lengths.
In the following section, model descriptions of Pauli repulsion and chemical attraction are introduced to examine how these reported interaction pictures relate to the experimentally observed decay lengths and why they are different.

6.2. Model descriptions of tip-corral interactions

To interpret the experimentally observed decay lengths, simplified analytical models for the two dominant interaction mechanisms are introduced. These models capture the essential distance dependence of Pauli repulsion and chemical attraction and provide a simple framework for understanding the measured force contrasts.
Stilp *et al.* [17] interpreted the attractive interaction observed between a metal-

terminated AFM tip and the confined Shockley surface state as a chemical interaction. This interpretation was based on the exponential distance dependence of the measured attraction, with decay lengths of about 50 pm, comparable to values reported for chemical interactions between a metal-tip and individual atoms. In addition, calculations presented by Stilp *et al.* showed that long-range electrostatic forces provide only a negligible contribution to the observed contrast. The analysis of the frequency shift contrast also largely suppresses the long-range van der Waals background arising from the interaction between the tip and the underlying Cu surface atoms. However, a spatially varying van der Waals attraction between the tip and the confined surface state cannot be excluded experimentally based on the measured distance dependence alone. In the following, the attractive interaction is discussed within the chemical-interaction interpretation proposed in Ref. [17].

6.2.1. Model description of Pauli repulsion for CO-tips

Before introducing the model description of Pauli repulsion, it is important to note that the decay length of the repulsion, which was extracted from the CO-tip measurements, is greater than the decay length of the surface charge density ($\lambda_{\mathrm{S}}^{\rho} = \lambda_{\mathrm{S}}^{\psi}/2 = 42\,\mathrm{pm}$). This behavior can be understood within a commonly used model description of Pauli repulsion which uses an overlap integral of the total charge densities of the tip ρ_{CO} and the sample ρ_{S}. Because the electronic wave functions of both the tip and the sample decay exponentially into the vacuum, the overlap of their electron densities, and therefore the resulting Pauli repulsion, is also expected to exhibit an approximately exponential dependence on the tip-sample separation. The overlap integral of the total charge densities is given by

$$F^{\mathrm{Pauli}} \propto -\frac{\partial}{\partial z}\int [\rho_{\mathrm{tip}}(\vec{r})\rho_{\mathrm{S}}(\vec{r})]^{\alpha}\mathrm{d}\vec{r}, \tag{6.5}$$

with $\alpha \approx 1$ (e.g., Refs. [116, 149–151]). In this model, the overlap integral is used to approximate the potential energy of the two interacting systems. Taking the derivative in the z-direction then yields the normal force F^{Pauli}, to which AFM is sensitive.

Equation (6.5) shows that the measured force, and therefore the force contrast, depends on both the decay length of the sample charge density and that of the

tip. In Section 3.1, the decay length of the sample electron density was determined as $\lambda_{\mathrm{S}}^{\rho} = 42\,\mathrm{pm}$ in the context of the electronic properties of the Shockley surface state. The charge density at the apex of the CO-tip can be approximated as an s-wave-like distribution (i.e., Slater-type functions for large distances from the atomic core). Based on the effective nuclear charge $Z_{\mathrm{eff}} \approx 4.5$ for the valence electrons of oxygen [152], the charge density of the frontmost part of a CO-tip decays approximately[1] with a decay length of 12 pm. Approximating the electron density of the sample also as an s-wave-like distribution has the advantage that Eq. (6.5) becomes analytically solvable, and similar solutions have been reported in related forms in textbooks (e.g., Ref. [153]). The analytically solved overlap integral for two s-wave-like electron densities is provided in Appendix A.7. A justification of the s-wave approximation on the sample side will be discussed later in Subsection 6.2.3.

Figure 6.5 shows the modeled Pauli repulsion between the tip and the corral states using the electron density decay lengths $\lambda_{\mathrm{S}}^{\rho} = 42\,\mathrm{pm}$ and $\lambda_{\mathrm{CO}}^{\rho} = 12\,\mathrm{pm}$ with $\alpha = 1$. Fitting the modeled curve with an exponential function in the height range where the CO-tip measurements were conducted (between 300 pm and 450 pm) yields a decay length of $\lambda_{\mathrm{CO}}^{\mathrm{Pauli}} = 43\,\mathrm{pm}$. This value is slightly larger than the charge density decay length of the Shockley surface state and lies within the measured error window of $(46 \pm 6)\,\mathrm{pm}$.

Discussion of the modeled decay length

Despite the good agreement between the modeled and measured decay length of Pauli repulsion, three possibilities were identified that could explain why the modeled decay length is slightly shorter than the measured one.

One possibility stems from the fact that the decay length of the Shockley surface state towards the vacuum was calculated using the work function of Cu(111) reported in the literature: $\Phi = 4.94\,\mathrm{eV}$ [47]. It is known that the close proximity of a probe tip can locally alter the potential landscape of the surface, which leads to a modification of the work function [154, 155]. Such a perturbation of the system by the AFM tip

[1] This estimate is based on Slater-type s-orbitals [152]: $\psi_{\mathrm{Slater}} \propto r^{n^*-1} \cdot \exp\bigl(-r \cdot Z_{\mathrm{eff}}/(a_0 n^*)\bigr)$. In this equation, r denotes the radial distance from the atomic core, a_0 the Bohr radius, n^* the effective quantum number, and Z_{eff} the effective nuclear charge. For large r the exponential function dominates and the decay length of the wave function is given by $\lambda_{\mathrm{eff}} = (a_0 n^*)/Z_{\mathrm{eff}}$.

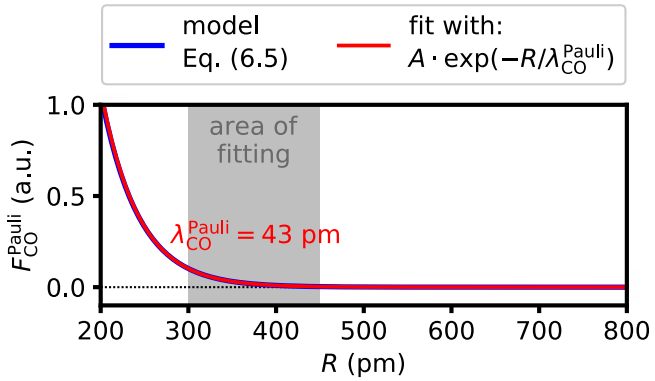


Figure 6.5: Modeled repulsive force (blue), based on Eq. (6.5). The electron densities of tip and sample were approximated by s-like distributions. The distance between the tip and the surface (center of the s-like electron density) is given by R. The electron density decay lengths for the tip and sample are $\lambda_{CO}^{\rho} = 12\,\text{pm}$ and $\lambda_{S}^{\rho} = 42\,\text{pm}$. The modeled curve was fitted with an exponential function (red) in the region between $R = 300\,\text{pm}$ and $R = 450\,\text{pm}$, corresponding to the height range where the CO-tip measurements were conducted. The fit yields a decay length of $\lambda_{CO}^{Pauli} = 43\,\text{pm}$.

could lead to a longer decay length of the sample wave function than expected from the unperturbed surface. A tip-induced effective sample work function of $\approx 4.5\,\text{eV}$ would be required to closely match the measured decay length[1].

Another possible explanation for the slight difference between the measured and simulated decay length is the scaling exponent α, which appears in the model description of Pauli repulsion [149, 150]. For clarity and consistency, this exponent was set to 1 up to this point. However, it has been shown that α can vary depending on the interacting systems. For molecular systems [150], values slightly above 1 have been reported, while interactions between single natural atoms often yield values slightly below 1 [149]. To closely match the modeled and measured decay lengths, a value of $\alpha = 0.92$ would be required. This suggests that small deviations from the idealized scaling behavior may be an intrinsic property of the interaction between the corral system and the CO-tip. This possibility could be taken into account for future refinements of the model.

A third possible contribution could arise from an additional long-range attractive interaction between the CO-tip and the corral states, which is not included in

[1]This was estimated by adjusting λ_{S}^{ρ} in Eq. (6.5) until the fitted decay length matched the measured value. The effective work function was then calculated using Eq. (3.3) from Section 3.1.

the model description of Pauli repulsion. Electrostatic forces are the most likely candidate for such an interaction. However, calculations by Stilp *et al.* [17] demonstrated that the electrostatic interaction between the AFM tip and the corral states is negligibly small. This is caused by the formation of a compensation layer of electron depletion below the corral states. The depletion layer has the same spatial distribution but the opposite sign, resulting in strongly reduced electrostatic forces. Furthermore, the remaining electrostatic interaction is expected to decay on the order of several hundred picometers. Additionally, since the presented analysis considers only the frequency shift contrast, spatially uniform long-range contributions, including the van der Waals background arising from the interaction between the tip and the underlying Cu surface atoms, are largely suppressed.

6.2.2. Model description of chemical attraction for metal-tips

A commonly used approximation for the distance dependence of chemical bonding is the overlap of wave functions (e.g., Refs. [153, 155–157]):

$$F^{\text{chem.}} \propto \frac{\partial}{\partial z} \int \psi_{\text{tip}}(\vec{r}) \psi_{\text{S}}(\vec{r}) \, \mathrm{d}\vec{r}. \tag{6.6}$$

Around the Fermi energy, which is the relevant energy regime for a quantum corral[1], metallic tips can predominantly be characterized by *s*-orbitals [158]. The decay length of these orbitals can be estimated in the same way as the decay length of the Shockley surface state [159, 160]: $\lambda^{\psi}_{\text{metal}} = \sqrt{\hbar^2/(2m_{\text{e}}(\Phi + 440\,\text{meV})} = 84\,\text{pm}$, where m_{e} is the electron mass and $\Phi = 4.94\,\text{eV}$ is the work function of copper. This estimate corresponds to the decay length at the onset of the Shockley surface state band, which lies 440 meV below the Fermi energy. Between the band edge and the Fermi level, the decay length of the tip varies only by about 5%. This slight variation is neglected for the following steps, as it does not affect the interpretation. The analytically solved overlap integral for two *s*-orbitals is provided in Appendix A.7. Figure 6.6 shows the modeled chemical attraction based on the overlap of *s*-like wave functions of tip and sample [Eq. (6.6)]. To account for the attractive interaction, a phenomenological minus sign was introduced. Fitting the modeled curve with an

[1]The band edge of the Shockley surface state is located 440 meV below the Fermi energy. Compared to the energy scales of natural atoms, this range is very narrow and located close to E_{F}.

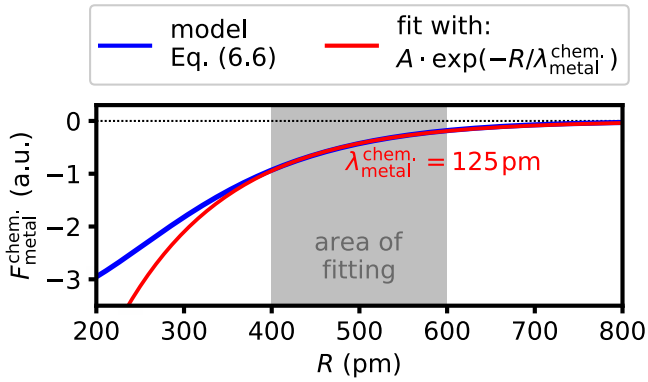


Figure 6.6: Modeled attractive force (blue), based on Eq. (6.6). The wave functions of tip and sample were approximated by s-orbitals. The distance between the centers of the orbitals is denoted by R. The decay lengths of both wave functions were set to 84 pm (see text). The modeled curve was fitted with an exponential function (red) in the region between $R = 400\,\text{pm}$ and $R = 600\,\text{pm}$, corresponding to the height range of the metal-tip measurements. The fit yields a decay length of $\lambda^{\text{chem.}}_{\text{metal}} = 125\,\text{pm}$.

exponential function in the height range where the metal-tip measurements were performed (between 400 pm and 600 pm) yields a decay length of $\lambda^{\text{chem.}}_{\text{metal}} = 125\,\text{pm}$. Within this simplified picture, the key difference between Pauli repulsion and chemical attraction lies in the quantities entering the respective models. The Pauli repulsion model depends on the overlap of the electron densities, i.e., the square of the wave function ($\rho \propto |\psi|^2$), whereas the chemical attraction model depends on the overlap of the wave functions themselves (ψ). Since the electron density decays spatially as $|\psi|^2$, it follows that the decay length associated with Pauli repulsion is intrinsically shorter than that associated with chemical attraction.

The same trend is also observed experimentally (Table 6.1), where the repulsive interaction measured with a CO-tip (46 pm) is shorter ranged than the attractive interaction measured with a metal-tip (66 pm).

Discussion of the modeled decay length

It is important to emphasize that the presented description of the chemical interaction between the tip and the corral states represents only a simplified model. While this approach qualitatively explains why chemical attraction decays more slowly than Pauli repulsion, the resulting decay length is approximately twice as large as the experimentally observed value.

A more accurate description of the interaction would require a more detailed treatment of the electronic structure. For example, approaches based on a linear combination of atomic orbitals (LCAO) naturally incorporate the spatial overlap of different orbitals and therefore provide a more realistic description of chemical bonding.
Developing such a model for the interaction between the AFM tip and the confined surface-state electrons is beyond the scope of this thesis. Instead, the simplified overlap model presented here is used to illustrate the qualitative physical origin of the longer decay length of chemical attraction compared to Pauli repulsion.

6.2.3. Estimated Pauli repulsion for metal-tips and validation of the model

The models introduced in the previous subsections describe the experimentally accessible interaction regimes: Pauli repulsion measured with a CO-functionalized tip and chemical attraction measured with a metallic tip. However, measurements with a pure metal-tip were experimentally limited to the attractive regime, since attempting to enter the repulsive regime resulted in tip instabilities. Although this regime was therefore not directly accessible, estimating the repulsive interaction expected for a metallic tip is instructive for interpreting the measured decay lengths and helps constrain the decay length ratio discussed in Section 6.3. Furthermore, the models used in the previous subsections are based on the use of s-like wave functions and electron density distributions. The validity of these approximations will also be evaluated below.

Estimated repulsive decay length for metal-tips

Assuming that the model description of Pauli repulsion based on the overlap of electron densities [Eq. (6.5)] also holds for a bare metal-tip, the repulsive decay length can be estimated within the same framework used for the CO-tip case. The decay lengths of the tip and sample electron densities are set to $\lambda^{\rho}_{\mathrm{metal}} = \lambda^{\rho}_{\mathrm{S}} = \lambda^{\psi}_{\mathrm{metal}}/2 = \lambda^{\psi}_{\mathrm{S}}/2 = (84\,\mathrm{pm})/2 = 42\,\mathrm{pm}$. Figure 6.7 shows the resulting simulated force, which is based on Eq. (6.5). Fitting an exponential function to the calculated force curve in the height range between 400 pm and 600 pm, which corresponds to

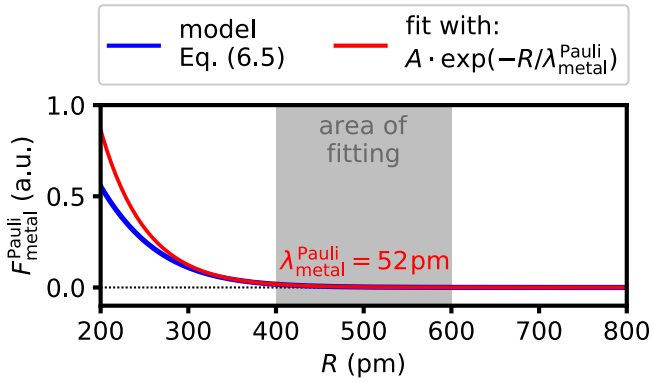


Figure 6.7: Modeled repulsive force (blue) for two s-like electron distributions. The distance between the two centers is given by R, while the electron density decay lengths were set to $\lambda^{\rho}_{\text{metal}} = \lambda^{\rho}_{\text{S}} = 42\,\text{pm}$. While experimentally not accessible, this setup simulates the repulsive force expected for a bare metal-tip. The modeled curve was fitted with an exponential function (red) in the region between 400 pm and 600 pm, corresponding to the height range of the metal-tip measurements. The fit yields a decay length of $\lambda^{\text{Pauli}}_{\text{metal}} = 52\,\text{pm}$.

the height range in which the metal-tip measurements were conducted, yields a modeled decay length of $\lambda^{\text{Pauli}}_{\text{metal}} = 52\,\text{pm}$.

This value is considerably larger than the modeled decay length in the case of a CO-tip, $\lambda^{\text{Pauli}}_{\text{CO}} = 43\,\text{pm}$ (see Subsection 6.2.1). This difference arises from the influence of the decay length of the tip electron density on the total decay length of the measured interaction. In both calculations, the decay length of the sample electron density was the same (42 pm), while the decay length of the tip electron density differed: 12 pm for the CO-tip and 42 pm for the metal-tip. Consequently, a longer decay length of the tip electron density results in a longer decay length of the measured interaction. This illustrates that the total decay length of the interaction is determined by both the sample and the tip electron densities. The influence of the tip decay length on the effective interaction decay length will be discussed further in Section 6.3.

Validation of the model approximations

In the previous subsections, both the wave functions and the electron density distributions were approximated by s-like functions. While this approximation is justified for the tip, its applicability to the sample may appear less intuitive because

the surface-state electron density extends laterally across the surface.
Nevertheless, the s-wave approximation for the sample is advantageous because it allows an analytical solution of the overlap integral while still capturing the essential decay behavior. To verify that this approximation does not significantly affect the resulting decay length, an overlap integral was calculated numerically using a more realistic sample electron density. In this numerical approach, the tip electron density was again modeled as an s-like distribution, while the sample electron density was assumed to be homogeneous in the xy-plane and to decay only exponentially in the z-direction:

$$\rho_{\mathrm{S}}(z) \propto \exp\left(-\frac{|z|}{\lambda_{\mathrm{S}}^{\rho}}\right). \tag{6.7}$$

For this calculation, the decay lengths of the tip and sample electron densities were set to $\lambda_{\mathrm{metal}}^{\rho} = \lambda_{\mathrm{S}}^{\rho} = 42\,\mathrm{pm}$. The tip position (distance between tip and sample) was varied between 200 pm and 800 pm, and for each position the three-dimensional overlap integral was calculated numerically[1]. The resulting curve is shown in Fig. 6.8. To compare the result with the analytical s-wave approximation used in the previous subsections (Subsections 6.2.1 and 6.2.2), the numerical curve was fitted with an exponential function in the range between 400 pm and 600 pm. The fit yields a decay length of 52 pm, which is in excellent agreement with the value obtained from the s-wave approximation (Fig. 6.7). This agreement demonstrates that the simplified s-wave approximation captures the relevant decay behavior of the interaction and therefore provides a reliable description of the force decay length within the considered distance range.

[1]The sample electron density was modeled in the xy-plane within a 1 nm × 1 nm area, which was discretized with a 5 pm pixel size. In the z-direction the same discretization was used and the sample electron density was modeled from −200 pm to 900 pm with $z = 0$ pm defined as the surface plane.

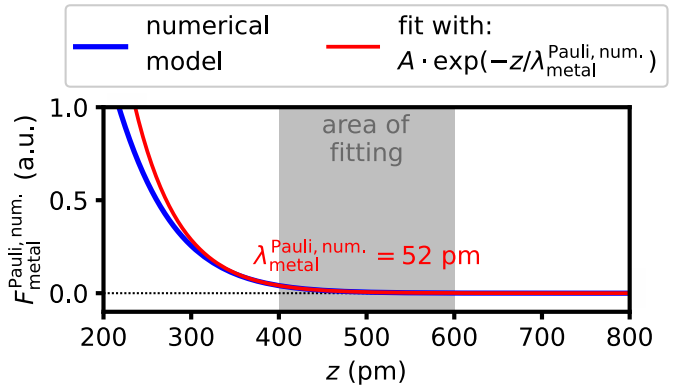


Figure 6.8: Numerically calculated overlap integral (blue) between an s-like electron distribution for the tip and a sample electron density that is homogeneous in the xy-plane and decays exponentially in the z-direction. The distance between the tip and the surface is given by R. Both decay lengths were set to $\lambda^{\rho}_{\text{metal}} = \lambda^{\rho}_{\text{S}} = 42\,\text{pm}$. The curve was fitted with an exponential function (red) in the region between $R = 400\,\text{pm}$ and $R = 600\,\text{pm}$, yielding a decay length of 52 pm, identical to the value obtained using the analytical s-wave approximation.

6.3. Decay length ratios and the Morse potential

The interaction potential between two atoms is often described by the semiempirical Morse potential [161], which provides an intuitive model for interatomic interactions. This potential consists of the sum of two exponential contributions: a short-range repulsive interaction dominating at small separations and a longer-ranged attractive interaction dominating at larger distances. Due to its simplicity and wide applicability, the Morse potential is widely used in many fields of science, ranging from surface catalysis to simulating dynamics in biological systems or gases [162]. It also provides a useful conceptual framework for analyzing interactions measured with atomic force microscopy.

In the original formulation by Morse, the attractive interaction decays with a characteristic length that is twice as large as that of the repulsive interaction, meaning $\mu = \lambda^{\text{attr.}}_{\text{Morse}}/\lambda^{\text{repul.}}_{\text{Morse}} = 2$. This ratio is not observed in the experimental data presented in this thesis. To assess whether the Morse ratio is compatible with the corral system, the role of the tip termination must therefore be taken into account. The attractive and repulsive decay lengths were not measured with the same tip: Attraction was probed with a metal-tip, whereas repulsion was measured with a CO-tip. Since the tip termination itself influences the measured decay lengths, the

ratio cannot be taken directly from the experimental data. The following discussion therefore uses the models introduced in this thesis to estimate physically plausible decay length ratios for a single tip termination.

For the metal-tip measurements, only the attractive regime of the interaction could be accessed, corresponding to the right-hand side of the minimum of the Morse-type interaction curve. Attempts to enter the repulsive regime with a metal-tip were unsuccessful because the strong forces between tip and sample led to tip instabilities or material transfer into the corral. Consequently, the experimental data are restricted to the attractive tail of the interaction, and a full Morse-type interaction curve could not be fitted to the measurements. Instead, the measured attraction was fitted with a single exponential function (Figs. 6.3 and 6.4), yielding an average decay length of 66 pm. It should be noted that fitting the attractive tail of a Morse-type interaction with a single exponential function leads to a systematic overestimation of the decay length. The steep repulsive part of the interaction, dominant at small tip-sample separations, slightly modifies the shape of the attractive tail, an effect that is not captured by a simple exponential fit.

This systematic overestimation can be used to derive an upper bound for the physically relevant decay length ratio. A mathematical analysis provided in Appendix A.8 shows that the fitted attractive decay length $\lambda^{\text{attr.}}_{\text{metal}}$ is always larger than or equal to the pure attractive decay length $\lambda^{\text{attr.}}_{\text{metal}} \geq \lambda^{\text{pure attr.}}_{\text{metal}}$, which means $\lambda^{\text{pure attr.}}_{\text{metal}} \leq 66\,\text{pm}$. If the original Morse ratio of $\mu = 2$ is applied, the corresponding repulsive decay length for a metal-tip would have to satisfy $\lambda^{\text{pure repul.}}_{\text{metal}} \leq 33\,\text{pm}$. This is incompatible with the experimental and modeled observations.

As demonstrated by the CO-tip measurements, Pauli repulsion in the corral system is well described by the overlap integral of electron densities. Since the decay length of the surface-state electron density is 42 pm, this value represents a strict lower bound for the repulsive decay length of the interaction.

To further illustrate this behavior, Fig. 6.9 shows a systematic analysis based on the electron density overlap model [Eq. (6.5)]. In this analysis, the decay length of the sample electron density was fixed at $\lambda^{\rho}_{\text{S}} = 42\,\text{pm}$, while the decay length of the tip electron density was varied between 1 pm and 100 pm. For each combination of decay lengths, the resulting modeled force curve was calculated and fitted with an exponential function in the experimentally relevant height range between 400 pm and 600 pm. The fitted decay lengths λ_{fit} are plotted as a function of $\lambda^{\rho}_{\text{tip}}$.

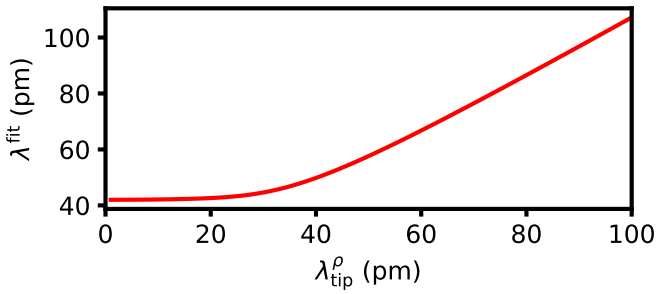


Figure 6.9: Simulated dependence of the fitted decay length λ_{fit} on the tip decay length $\lambda^{\rho}_{\text{tip}}$. The decay length of the sample electron density was fixed at $\lambda^{\rho}_{\text{S}} = 42$ pm, while $\lambda^{\rho}_{\text{tip}}$ was varied between 1 pm and 100 pm. The transition from a sample-dominated regime ($\lambda^{\rho}_{\text{tip}} \lesssim 30$ pm) to a tip-influenced regime ($\lambda^{\rho}_{\text{tip}} \gtrsim 30$ pm) illustrates the convolution-like character of the interaction.

For very short decay lengths of the tip electron density, the resulting interaction decay length remains close to the decay length of the sample electron density. The resulting decay length is always larger than that of the sample electron density ($\lambda^{\rho}_{\text{S}} = 42\,\text{pm}$). With increasing $\lambda^{\rho}_{\text{tip}}$, the decay length of the interaction becomes progressively influenced by the tip and eventually increases approximately linearly with $\lambda^{\rho}_{\text{tip}}$. This behavior reflects the convolution-like character of the interaction between tip and sample electron densities. This analysis also explains why the modeled Pauli repulsion decay length for a CO-tip (Subsection 6.2.1) remains close to the sample decay length: The very short decay length of the CO-tip electron density (12 pm) contributes only weakly to the total decay length of the interaction, which is therefore dominated by the electron density of the sample.

The lower bound of the repulsive decay length therefore already excludes the Morse ratio of $\mu = 2$. Using the measured attractive decay length as an upper limit yields $\mu_{\text{max}} = 66\,\text{pm}/42\,\text{pm} = 1.6$. Including the estimated repulsive decay length for a metal-tip (52 pm, see Subsection 6.2.3) further tightens this constraint: $\mu_{\text{max}} = 66\,\text{pm}/52\,\text{pm} = 1.3$.

It is important to note that the ratios presented here do not contradict the general concept of the Morse potential. They show that the decay ratio assumed in its original form is not applicable to the corral system.

The deviation from the Morse ratio suggests that the distance dependence of the interaction in a quantum corral on Cu(111) differs from that of conventional atom-atom interactions. To understand the origin of this difference, it is instructive to

compare the decay lengths observed in the corral system with those reported for interactions between natural atoms.

6.4. Comparison of a quantum corral to a natural atom

A better understanding of the measured decay lengths of the interaction between tip and corral can be achieved by comparing them with the decay lengths observed in interactions between natural atoms. Natural atom-atom interactions exhibit the same qualitative trend, with chemical attraction being longer ranged than Pauli repulsion, but their characteristic decay lengths are considerably shorter than those observed for the quantum corral system.

Ternes *et al.* [155] reported decay lengths for chemical bonding between a metal-tip and individual Cu and Pt adatoms on Cu(111) of approximately 40 pm. Comparable values were obtained by Rubio-Bollinger *et al.* [163] for metallic adhesion between gold atoms in atomic junctions, where decay lengths of around 45 pm were found. In contrast, the attractive interaction between a metal-tip and the corral states decays more slowly, with a decay length of 66 pm.

A similar trend is observed for Pauli repulsion. CO-tips on CaF_2 yielded a repulsive decay length of 27 pm, and atomic scattering experiments across various atomic species reported values of approximately 28 pm [164–169]. By comparison, the repulsive interaction measured with a CO-tip over the quantum corral exhibits a decay length of 46 pm.

The observed difference likely originates from the energy ranges of the interacting electronic states. Natural atoms exhibit electronic states that are distributed over a wide energy range, extending from deep-lying core levels up to the Fermi energy. These electronic states extend several electron volts below the Fermi level and include orbitals that are highly localized in space. For example, in Cu(111) the onset of the *sp*-bands lies roughly 10 eV below the Fermi energy and extends over a broad energy range [170–173]. In contrast, the 3*d*-band begins approximately 5 eV below E_F and is nearly fully occupied [170–173]. This situation is schematically illustrated in the lower left panel of Fig. 6.10(a).

An electronic state in a one-dimensional potential well can be used to approximate the

energy dependence of the decay lengths. Within such a framework, the exponential decay length is given by $\lambda = \hbar/\sqrt{-2m_e E}$, where the energy E is relative to the vacuum level (= 0). As an example, the $1s$ core level of copper has a binding energy of approximately 9 keV [174], which corresponds to an estimated wave function decay length of 2 pm. Because the atomic spacing in bulk copper is $\approx$ 255 pm, such deeply bound orbitals barely overlap and therefore do not form bands. In contrast, electronic states near the onset of the Shockley surface state, which lies 440 meV below E_F, exhibit decay lengths of approximately 84 pm. The corresponding dependence of the decay length on energy is illustrated in the lower right panel of Fig. 6.10(a).

Between two natural atoms, the total chemical interaction can be understood as a superposition of contributions from multiple orbitals across a wide energy range. Orbitals with long decay lengths, located near the Fermi energy, begin to overlap at relatively large distances. As the atoms approach each other, deeper and more localized orbitals start to overlap, leading to a more rapid increase in the interaction force. The total interaction can thus be interpreted as a combination of multiple orbital overlaps, each characterized by its own spatial decay. Because short-ranged contributions from strongly bound orbitals are also present, the resulting effective interaction decays faster than the individual contributions near the Fermi level alone. Since AFM is sensitive to the total charge density, including contributions from highly localized states with large binding energies, this framework also provides an explanation for the exceptional spatial resolution achieved in AFM measurements [109].

For an artificial atom such as a quantum corral, the situation is different. The occupied corral states lie within a very narrow energy window between the band edge of the Shockley surface state and the Fermi energy, corresponding to an energy range of only 440 meV. This situation is illustrated in the lower right panel of Fig. 6.10(b). In contrast to natural atoms, the corral system does not contain deeply bound, strongly localized states that could contribute to the interaction. The occupied corral states originate from the Shockley surface state and therefore exhibit decay lengths of 84 pm [17]. The estimated decay lengths of the electronic states of natural atoms vary only slightly within the narrow energy range of the occupied corral states (from 84 pm to 87 pm). This situation is illustrated in the lower left panel of Fig. 6.10(b). As a result, the interaction between the corral

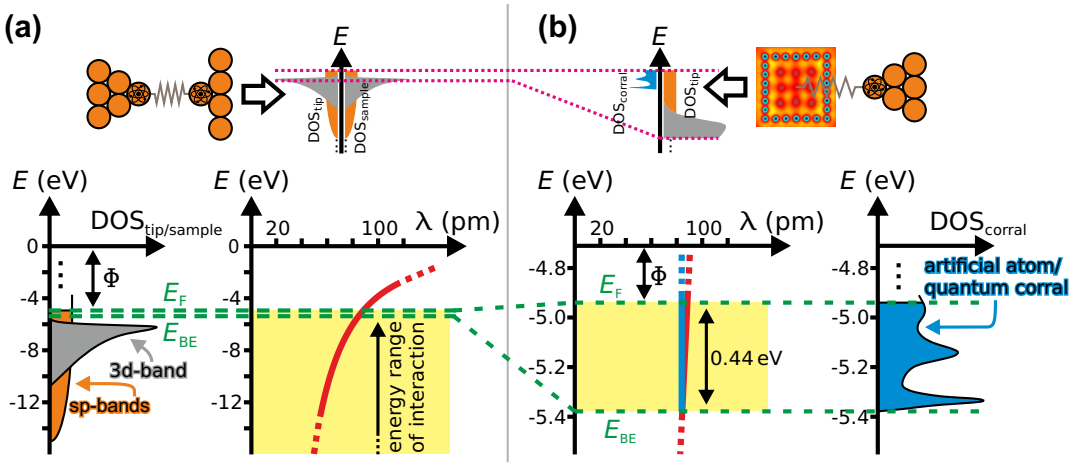


Figure 6.10: Qualitative comparison of the electronic states contributing to tip-sample interactions involving natural atoms and artificial atoms (quantum corrals). The key difference is that natural atoms possess electronic states over a wide energy range, including deeply bound orbitals with very short decay lengths, whereas quantum corrals contain only electronic states within a narrow energy window close to the Fermi level. As a result, interactions involving natural atoms include short-ranged contributions from deep orbitals, while interactions with quantum corrals are dominated by long-ranged states. (a): Natural atom-atom interaction. Bottom left: schematic density of states (DOS) of a natural atom at the AFM tip apex and of a natural adatom on a surface. For clarity, identical DOS profiles are assumed for tip and sample, both showing broad *sp*- and *d*-bands (lower-lying bands are omitted). The Fermi energy E_F lies $\Phi = 4.94\,\mathrm{eV}$ below the vacuum level, while E_BE indicates the band edge of the Shockley surface state. Bottom right: approximate dependence of the decay length λ on the binding energy, following $\lambda \propto 1/\sqrt{-E}$. (b): Interaction between a natural atom and an artificial atom (quantum corral). Top left: schematic comparison of the DOS of the tip and the corral states, where the tip DOS corresponds to a magnified view of the natural atom DOS shown in (a). Bottom left: the relevant interaction energy window for the corral is restricted to the range between the Shockley surface state band edge E_BE and the Fermi level E_F. Bottom right: local density of states (LDOS) at the center of the corral obtained from a $\mathrm{d}I/\mathrm{d}V$ spectrum (see Appendix A.5). Because only a narrow energy range contributes to the interaction in the corral system, the resulting interaction is dominated by long-ranged electronic states, leading to larger effective decay lengths than in natural atom-atom interactions.

states and the AFM tip is dominated exclusively by long-ranged electronic states, which leads to longer decay lengths for both attractive and repulsive interactions compared to interactions between natural atoms.

Examples from the literature further support that bonding in natural systems often involves deeper-lying electronic states. For instance, the $3d$-band of noble metals plays a crucial role in the adsorption of CO, O, and CO_2 on copper clusters [175] and on transition metal surfaces such as Cu, Ag, and Au [176]. This band lies several electron volts below E_F. Even fully occupied semicore orbitals can participate in bonding. For example, the existence of HgF_4 has been explained by bonding contributions from filled d-orbitals of mercury [177], while CsF_5 has been predicted to involve contributions from fully occupied p-orbitals [178]. A further example is the uranyl ion UO_2^{2+}, in which the bonding is mainly governed by $5f$- and $6d$-orbitals, while at shorter bond distances even the fully occupied $6p$ semicore orbitals begin to hybridize and participate in the interaction [179–181]. Deeper-lying orbitals were also shown to participate in bonding in solid-state systems [182]. The participation of such strongly bound orbitals implies that interactions between natural atoms contain contributions with very short decay lengths. As a result, the superposition of these contributions leads to an overall interaction that decays more rapidly than in the quantum corral system, where only electronic states near the Fermi level are involved.

This interpretation also suggests a possible route toward shorter interaction decay lengths in artificial atoms on surfaces. A reduction of the decay length of the Shockley surface state towards the vacuum would shorten the interaction decay length between an AFM tip and Shockley-surface-state-based corral states. This could bring the values measured over artificial atoms closer to those observed for natural atoms. Based on the modeling of the CO-tip measurements presented in Subsection 6.2.1, the same overlap-integral model can be used to estimate the sample electron-density decay length required to reproduce the interaction decay length of approximately 28 pm observed for a CO-tip above a natural atom. For this estimate, the sample electron-density decay length was varied until the fitted interaction decay length reached approximately 28 pm. The resulting sample decay length is about 27 pm.

As discussed in Chapter 3, the decay length of the Shockley surface state depends on both the work function of the surface and the band edge of the surface state.

According to Eq. (3.3), achieving an electron-density decay length of 27 pm would require a value of $\Phi + |E_{\mathrm{BE}}| \approx 13\,\mathrm{eV}$. Other noble-metal surfaces, such as Ag(111) and Au(111), have work functions similar to that of Cu(111) [183], namely $\Phi \approx 5\,\mathrm{eV}$, and Shockley surface state band edges E_{BE} at approximately $-60\,\mathrm{meV}$ and $-490\,\mathrm{meV}$, respectively [184]. They are therefore not suitable candidates.
It has been shown that Be(0001) also hosts a Shockley surface state observable with STM [185], with a band edge at approximately $-2.8\,\mathrm{eV}$ below the Fermi energy [186]. Combined with a work function of about 5 eV, this would yield a native electron-density decay length of roughly 36 pm. Evaluating the electron-density overlap integral, as in Subsection 6.2.1, for a CO-tip results in an interaction decay length of about 37 pm. This corresponds to 78% of the repulsive decay length observed for the CO-tip measurements on Cu(111).

6.5. Summary and Outlook

Summary

In this chapter, constant-height AFM measurements conducted with CO- and metal-terminated tips inside a square-shaped quantum corral on Cu(111) were presented. The comparison between the measurements and simulations based on the multiple scattering approach developed by Heller *et al.* [24] supports earlier observations [17] that the interaction measured with atomic force microscopy in a quantum corral scales with the surface charge density.
Metal-terminated tips interact attractively with the confined surface state, whereas CO-terminated tips experience a repulsive interaction. Furthermore, the forces measured with CO- and metal-terminated tips were found to decay exponentially with distinct decay lengths. AFM measurements performed over quantum corrals with identical geometry but a denser wall showed that the decay lengths of the attractive and repulsive interactions are independent of the corral wall density and the mesoscopic tip shape. The attractive interaction measured with a metal-tip exhibits a decay length of $\lambda_{\mathrm{metal}}^{\mathrm{attr.}} = (66 \pm 5)\,\mathrm{pm}$, while the repulsive interaction measured with a CO-tip yields $\lambda_{\mathrm{CO}}^{\mathrm{repul.}} = (46 \pm 6)\,\mathrm{pm}$. The two decay lengths differ by a factor of 1.4 ± 0.2.
Applying an established electron density overlap model to characterize Pauli repul-

sion (between CO-tip and corral states) resulted in a calculated decay length of $\lambda_{\mathrm{CO}}^{\mathrm{Pauli}} = 43\,\mathrm{pm}$. A first-order approximation of the suggested chemical attraction between a metal-tip and the corral states [17], based on the overlap of wave functions, reproduces the experimentally observed trend $\lambda_{\mathrm{metal}}^{\mathrm{attr.}} > \lambda_{\mathrm{CO}}^{\mathrm{repul.}}$, although it predicts a decay length that is larger than the experimentally observed value.

A full Morse-type curve could not be fitted to the metal-tip measurements due to experimental constraints. Instead, the attractive interaction was fitted with a single exponential function, leading to a systematic overestimation of the attractive decay length $\lambda_{\mathrm{metal}}^{\mathrm{attr.}} \geq \lambda_{\mathrm{metal}}^{\mathrm{pure\ attr.}}$. By analyzing the measured decay lengths together with the model descriptions, it was shown that the decay length ratio predicted by the original Morse potential, $\mu = \lambda_{\mathrm{Morse}}^{\mathrm{attr.}}/\lambda_{\mathrm{Morse}}^{\mathrm{repul.}} = 2$, does not apply to the quantum corral system. The analysis presented in this chapter establishes an upper bound of $\mu_{\mathrm{max}} = 1.6$, demonstrating that the decay ratio assumed in the original Morse formulation does not describe the interaction between an AFM tip and the confined surface state.

Finally, a comparison between natural atoms and artificial atoms (quantum corrals) showed that both attractive and repulsive interactions exhibit longer decay lengths in the quantum corral system. This behavior can be attributed to the absence of deep-lying, strongly localized orbitals within the narrow energy range of the occupied corral states near the Fermi level. In contrast, natural atoms exhibit electronic states across a wide energy range, including rapidly decaying orbitals far below E_{F}, which together result in a shorter effective decay length.

Outlook

Artificial nanostructures on surfaces generally provide an interesting platform for investigating novel electronic and chemical phenomena. Recently, Sierda *et al.* [28] introduced a method to simulate molecular electronic structures by constructing small coupled quantum corrals on the semiconductor InSb. An intriguing question for future studies is whether such artificial molecules exhibit a chemical reactivity similar to their natural counterparts.

The growing field of designer electronic states has already created exciting systems with unique properties, such as SSH chains [6] and kagome lattices [5] with interesting topological behavior, or Lieb lattices [3, 4] and artificial graphene [2] with Dirac

cones. These developments raise the fundamental question of how such exotic electronic states participate in, for example, chemical interactions. In particular, it remains to be investigated whether CO-functionalized and metallic tips interact with these designer electronic states in a manner similar to the interactions observed for individual quantum corrals.

Furthermore, quantum corrals have already been realized on a variety of other materials, including graphene [187], Rashba surface alloys [83], semiconductors [28], proximity-induced superconductors [130], and topological insulators [188]. A promising direction for future research is therefore to investigate the chemical bonding interactions between probe tips and confined electronic states in such systems.

Finally, the interactions between confined electronic states in artificial nanostructures and a probe tip can be explored using a variety of different tip terminations. Established terminations include copper oxide tips [189, 190], Xe-functionalized tips [191, 192], and magnetic molecules such as nickelocene [193]. Applying the experimental approach presented in this thesis with alternative tip functionalizations provides a promising avenue for investigating the nature of chemical bonds under conditions of precisely controlled chemical reactivity. In addition, spin-polarized tips [194, 195] offer interesting opportunities to investigate interactions on surfaces of materials where magnetism plays an important role, such as superconductors or topological insulators.

7. General conclusions and perspective

The concept of an artificial atom is powerful because it suggests that selected aspects of natural atoms can be recreated in a controlled solid-state environment. As expected, the results presented in this thesis show that quantum corrals are not simply enlarged versions of natural atoms. They are artificial quantum systems in which individual ingredients of atomic behavior, such as confinement, lifetime, and interaction with an external probe, can be separated and investigated more independently than in natural atoms.

In a natural atom, the orbital structure, the spatial decay of the wave functions, and the bonding behavior are largely determined by the nuclear charge and the resulting atomic potential. Changing this potential means changing the chemical identity of the atom. In a quantum corral, by contrast, the relevant electronic states originate from the pre-existing Shockley surface state of Cu(111). The corral wall defines a lateral confinement region for this two-dimensional electron gas and thereby turns the continuous surface state into discrete corral states. Although both systems host localized electronic states, the confinement is realized in different ways. Natural atoms bind electrons in an attractive atomic potential, whereas quantum corrals laterally confine a surface state with a boundary formed by atoms or molecules on the surface.

The nanometer size of quantum corrals makes these artificial atoms directly accessible to STM and AFM measurements. At the same time, the confining wall consists of individually positioned surface adsorbates, allowing the artificial atom to be modified by changing the geometry, density, or composition of the wall. Changing the boundary also changes the artificial atom, but this is precisely the advantage: The system can be modified in a controlled way, while the underlying electronic state remains the Shockley surface state of Cu(111). Quantum corrals are therefore valuable not because they perfectly imitate natural atoms, but because they allow selected components of atomic behavior to be isolated and studied in a controlled way.

7.1. Decoupling lifetime, confinement, and interaction range

A central theme of this thesis is the role of decay lengths. Two fundamentally different decay problems were investigated. The first concerns the lateral propagation of confined electrons inside the surface plane, which determines the lifetime and therefore the spectral width of the corral states. The second concerns the vertical decay of the electronic wave function into the vacuum, which determines the decay length of the interaction with an AFM tip.

The results show that these two decay problems can be decoupled. Altering the corral radius and wall density modifies the lifetime of the confined states by changing the probability for lateral transmission through the boundary and loss at the corral wall. At the same time, the vertical decay length of the interaction with the AFM tip remains essentially independent of the wall density. This demonstrates that the lifetime of an artificial state can be engineered via the boundary without necessarily changing the vacuum decay of the underlying electronic state.

The corral wall therefore has to be viewed as an integral part of the artificial atom, rather than as a passive geometric outline. Similar to the atomic core in a natural atom, it defines the confinement of the electronic states. However, the corral wall has a more versatile role: It acts as a reflector, a tunnel barrier, a channel to bulk states, and possibly as a dynamic object via the vibrational motion of the CO molecules. This is reflected in the observed dependence of the spectral width on the wall density, which shows that the boundary affects not only the spatial structure of the corral states, but also their lifetime and spectral shape.

The force measurements add a second layer to this picture. They show that the spatial range, i.e., the decay length, of the interaction between an AFM tip and an artificial atom is governed by the electronic structure of the participating states. Because the occupied corral states originate from the Shockley surface state and occupy only a narrow energy window near the Fermi level, the relevant wave-function and electron-density components have a comparatively large characteristic decay length into the vacuum. This explains why both attractive and repulsive force interactions have larger decay lengths in the quantum corral system than in interactions between natural atoms.

Taken together, the lifetime measurements and the force measurements highlight a central advantage of quantum corrals as artificial atoms. In natural atoms, the lifetime of an electronic state and the spatial extent of its wave function are both tied to the atomic potential, the shell structure, and the available decay channels. Although these properties can be influenced, for example, by external fields or by changing the atomic environment, this does not provide a simple structural tuning knob like the wall density of a quantum corral. In a quantum corral, by contrast, the wall density can modify the lifetime of the confined states, while the vertical decay length into the vacuum remains mainly governed by the Shockley surface state character. Quantum corrals therefore allow lifetime and interaction range to be influenced by different physical ingredients, which is one of their key advantages as artificial atoms.

7.2. Towards designer interactions

The results of this thesis suggest that quantum corrals can be used to move from designer electronic states towards designer interaction landscapes. The findings presented in this thesis show that the confined charge density is not only observable in spectroscopic measurements but also determines where an external atom (i.e., the AFM tip) is attracted or repelled. The wave functions of the artificial atom therefore become spatial templates for local interactions.

The vertical decay length of the force interaction is mainly governed by the electronic character of the Shockley surface state and is therefore not easily changed by modifying the corral wall. The in-plane interaction landscape, however, can be shaped by changing the occupied corral states through geometry, size, and wall density. Quantum corrals may therefore not allow arbitrary tuning of how far the interaction reaches into the vacuum, but they do allow control over where inside the artificial atom the interaction is strongest.

This distinction suggests a new way of thinking about artificial atoms. A corral state is not only an artificial orbital with a given energy and spatial pattern, but also a resonance with a finite quality factor. The spectral width describes how strongly this state is coupled to its environment, while the real-space charge distribution describes how it interacts locally with an external probe. Long-lived states with

designed spatial patterns would therefore represent artificial orbitals whose energy, lifetime, and interaction landscape can be optimized separately.

This idea also raises a broader conceptual question: Which ingredients are actually required for atom-like chemical interactions? In a natural atom, bonding is tied to electrons bound by a nuclear Coulomb potential and embedded in a complex shell structure. In a quantum corral, there is no central nucleus forming the confined state. Instead, a lateral boundary creates a structured electron density from the pre-existing Shockley surface state. The observation of attractive and repulsive force contrast shows that atom-like interaction patterns can emerge even when the electronic state is defined by a boundary rather than by a nuclear potential.

Quantum corrals therefore provide a reductionist model system for atomic-scale interaction physics. Natural atoms combine nuclear charge, core orbitals, valence orbitals, shell structure, and chemical identity in a single object. In quantum corrals, many of these ingredients are absent or can be varied separately. This makes it possible to ask which aspects of chemical interaction require the full complexity of a natural atom, and which already arise from a confined and spatially structured electron density near the Fermi level.

In this sense, the long-term goal is not only to create artificial atoms with selected energy levels. A more ambitious goal is to design quantum states with chosen spatial charge distributions, controlled lifetimes, and measurable local interaction patterns. Such systems provide a new route towards studying, for example, chemical interactions in an environment where the electronic structure can be engineered rather than merely accepted.

7.3. Concluding remarks

The work presented in this thesis shows that artificial atoms are not only analogues of natural atoms but also controllable laboratories for atomic-scale interaction physics. By tuning the boundary of a quantum corral, the lifetime of confined electronic states can be modified. By probing the same states with functionalized AFM tips, the resulting interactions can be measured and compared to those of natural atoms. Together, these results demonstrate that quantum corrals provide a model system in which confinement, lifetime, and interaction with an external probe can be studied

in a controlled and partially separable way.
The central insight is that artificial atoms do not need to reproduce all properties of natural atoms to be useful. Their strength lies precisely in the fact that selected properties can be isolated, modified, and probed independently. In this sense, quantum corrals offer a route towards designing quantum states not only with tailored energies and lifetimes but also with controlled spatial charge distributions and experimentally accessible interaction landscapes.

A. Appendix

A.1. Quantum corral construction plans

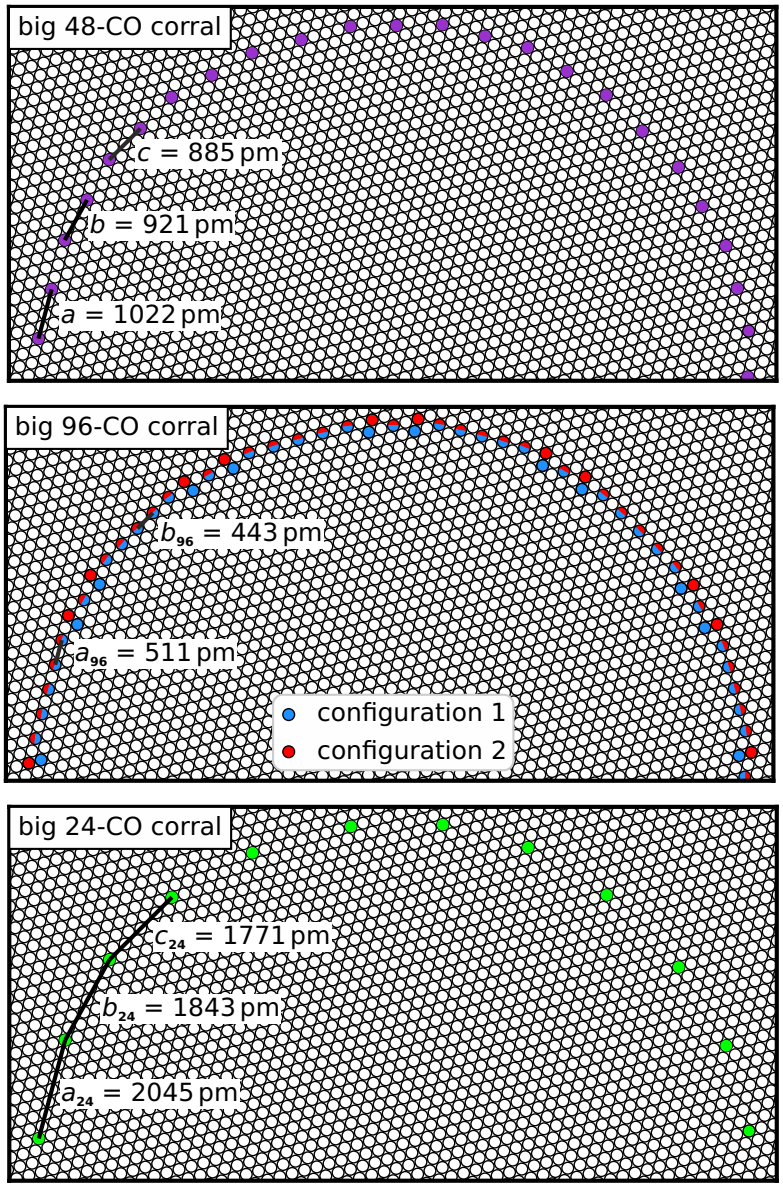
The radii and side lengths given for the quantum corrals in this thesis are based on the discrete adsorption sites of CO on Cu(111). For circular corrals, the calculated radius can depend slightly on the value chosen for the Cu lattice constant, on rounding, and on how the radius is determined from the discrete adsorption sites. For consistency with the original 48-Fe quantum corral introduced by Crommie *et al.* [79], the big circular corrals are referred to throughout this thesis by their nominal radius of 7.13 nm. The big 48-CO corral studied here follows the same lateral construction plan as the original 48-Fe corral, with the same relative distances between neighboring wall scatterers. If the average radius is calculated as the mean distance of all wall adsorption sites from the center of the corral, using the Cu lattice constant $a_0 = 361.5\,\text{pm}$ [106] yields an average radius of 7.15 nm. This differs from the nominal value of 7.13 nm by about 0.3%, which is negligible for the present analysis.

The same convention is used for the small 24-CO circular corral. Its nominal radius is defined as half of the nominal radius of the big 48-CO corral, i.e., $7.13\,\text{nm}/2 = 3.565\,\text{nm} \approx 3.57\,\text{nm}$. Calculating the mean distance of all wall adsorption sites from the center gives an average radius of 3.58 nm.

Applying the same calculation to the circular corrals with different wall densities shows that their average radii differ from one another by less than 1%. All big circular corrals are therefore treated as having the same nominal radius of 7.13 nm.

The intermolecular distances and wall densities given for the circular and square corrals are calculated using the same Cu lattice constant, $a_0 = 361.5\,\text{pm}$ [106]. The side lengths of the square corrals are also based on this value.

A.1.1. Circular quantum corrals



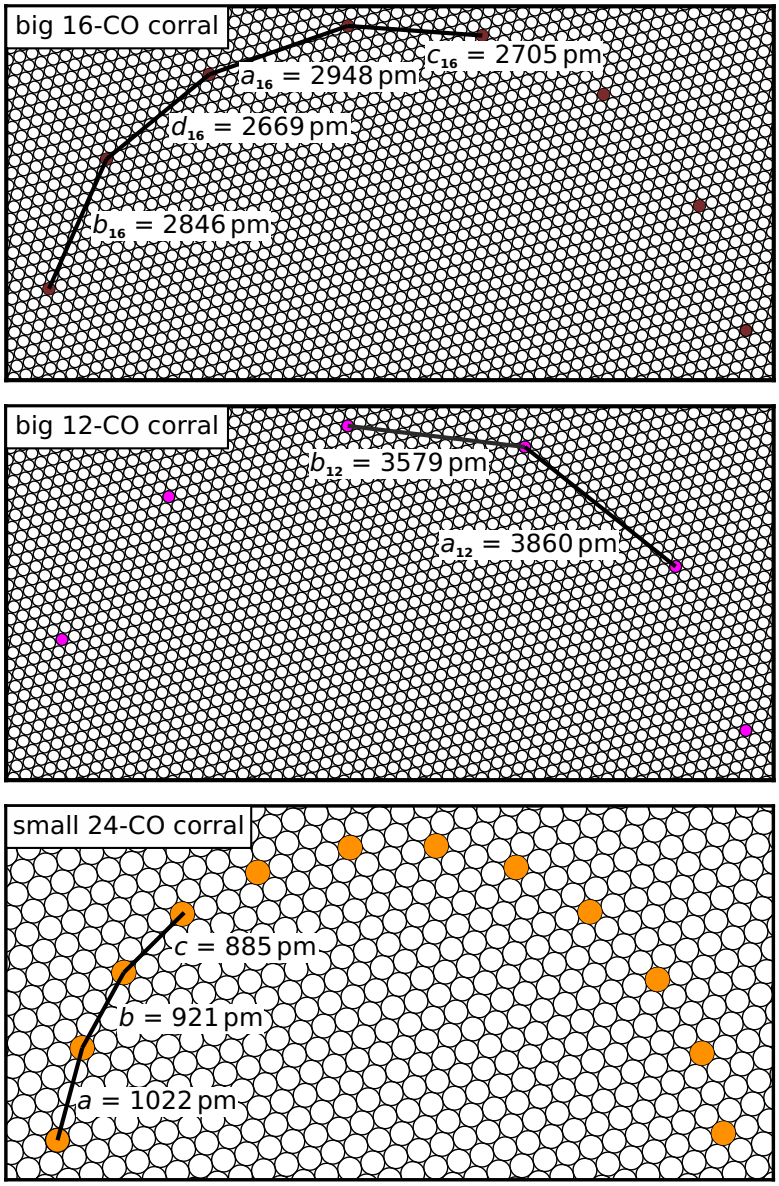


Figure A.1: Construction plans for the circular corrals studied in Chapter 5. Black unfilled circles represent the Cu(111) surface atoms, while filled colored circles indicate the positions of the CO molecules. The big corrals have a nominal radius of 7.13 nm, whereas the small 24-CO corral has a nominal radius of 3.57 nm. For the big 12-, 16-, 24-, 48-, and both 96-CO corrals, the average intermolecular distances are 3719 pm, 2792 pm, 1876 pm, 938 pm, and 477 pm, corresponding to wall densities of 0.269 nm^{-1}, 0.358 nm^{-1}, 0.533 nm^{-1}, 1.066 nm^{-1}, and 2.096 nm^{-1}, respectively. For the small 24-CO corral, the average intermolecular distance is 936 pm, corresponding to a wall density of 1.069 nm^{-1}.

A.1.2. Square quantum corrals

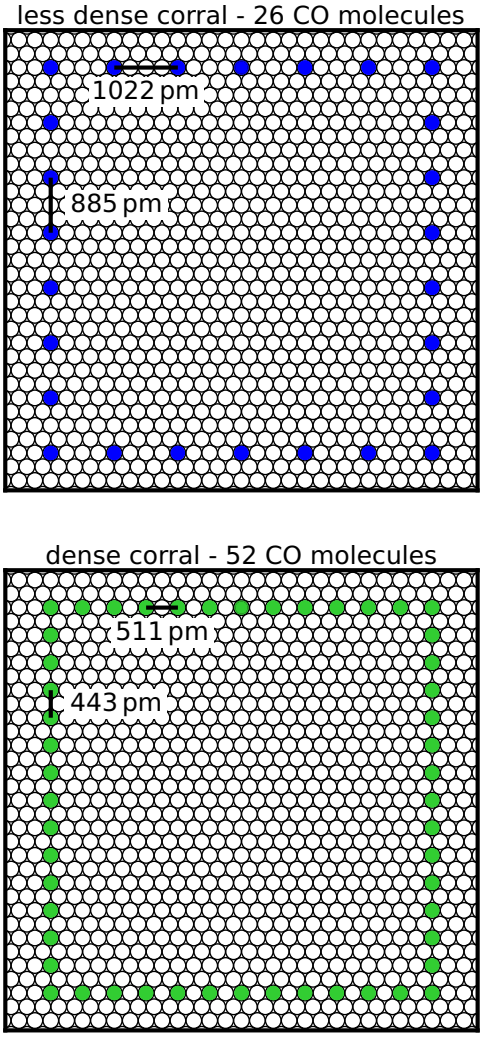


Figure A.2: Construction plans for the square quantum corrals studied in Chapter 6. Black unfilled circles represent the Cu(111) surface. Filled colored circles indicate the positions of the CO molecules. The less dense square corral consists of 26 CO molecules and the denser corral consists of 52. Both corrals have the same size with side lengths of $L_x = 6.13\,\mathrm{nm}$ and $L_y = 6.20\,\mathrm{nm}$. The average intermolecular distance is 948 pm for the less dense corral and 474 pm for the dense corral. The wall densities are $1.055\,\mathrm{nm}^{-1}$ and $2.110\,\mathrm{nm}^{-1}$.

A.2. Comparison between experimental and fitted line scans

Excellent agreement between the experimental $\mathrm{d}I/\mathrm{d}V$ line scans and the fit with Eq. (5.1) is found across the entire investigated bias range ($-450\,\mathrm{mV}$ to $400\,\mathrm{mV}$) for both corrals. This is illustrated by the direct comparison between experimental data and fit in Fig. A.3.

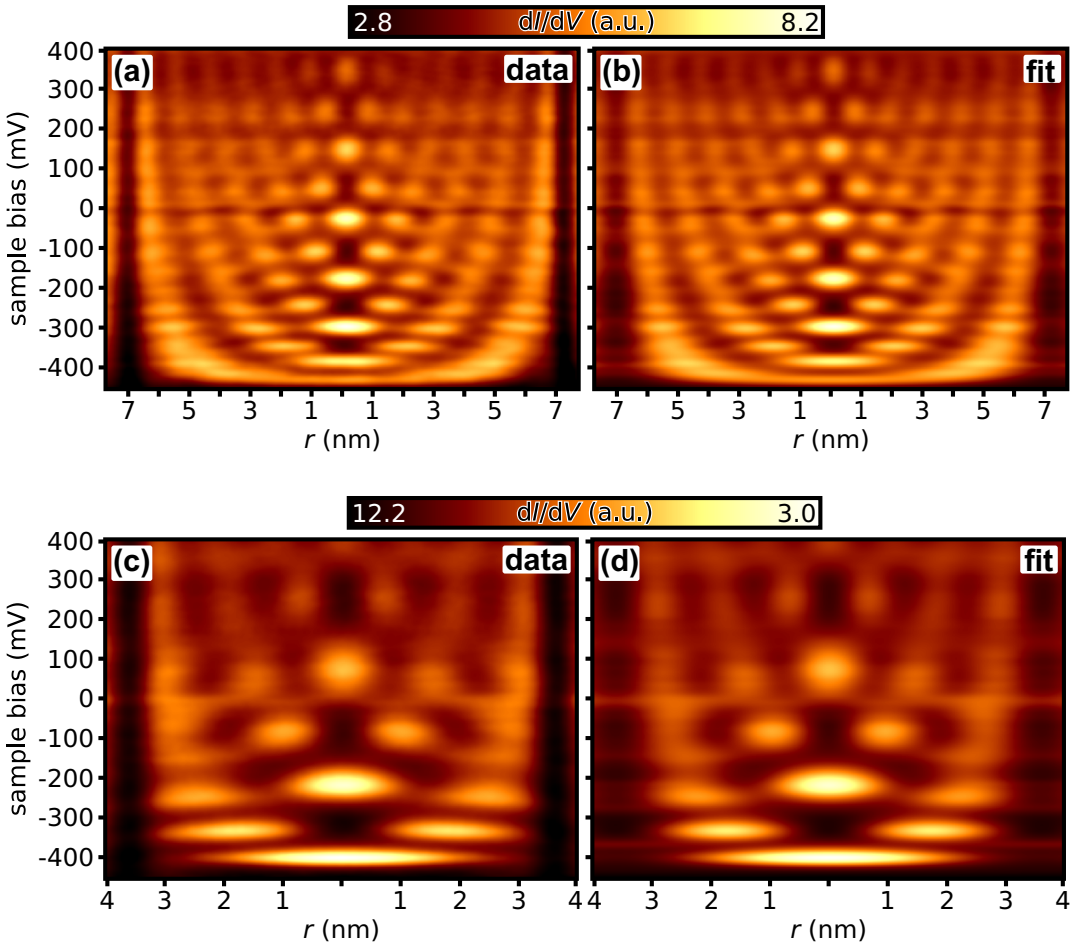


Figure A.3: $\mathrm{d}I/\mathrm{d}V$ measurements as a function of radial distance r from the center and sample bias for the (a) big 48-CO corral and the (c) small 24-CO corral. The fits with Eq. (5.1) to the experimental data are displayed in (b) and (d).

While there is excellent agreement between the data and the fit within the interior of the corrals, clear discrepancies emerge near the corral walls, where the CO molecules are positioned. For the big 48-CO corral, depicted in Fig. A.3(a) and

(b), these discrepancies are prominent at a radial distance of $r \approx 7\,\mathrm{nm}$. For the small 24-CO corral, depicted in Fig. A.3(c) and (d), these differences are notable around $r \approx 3.5\,\mathrm{nm}$. This discrepancy originates from the exclusion of the LDOS behavior near CO molecules in the wave function fits based on the hard wall model. However, it is important to note that the fits accurately reproduce the LDOS within the corral itself, which is the region of primary interest.

A.3. Energy distributions and fits for the big 48-CO and small 24-CO corral

The distributions were fitted with Eq. (5.3). Afterwards, the quality factor ξ was determined as described in Subsection 5.1.2. In this section, all the reconstructed energy distributions with $\xi \geq 0.80$ are presented.

A.3.1. $l = 0$ states - big 48-CO corral

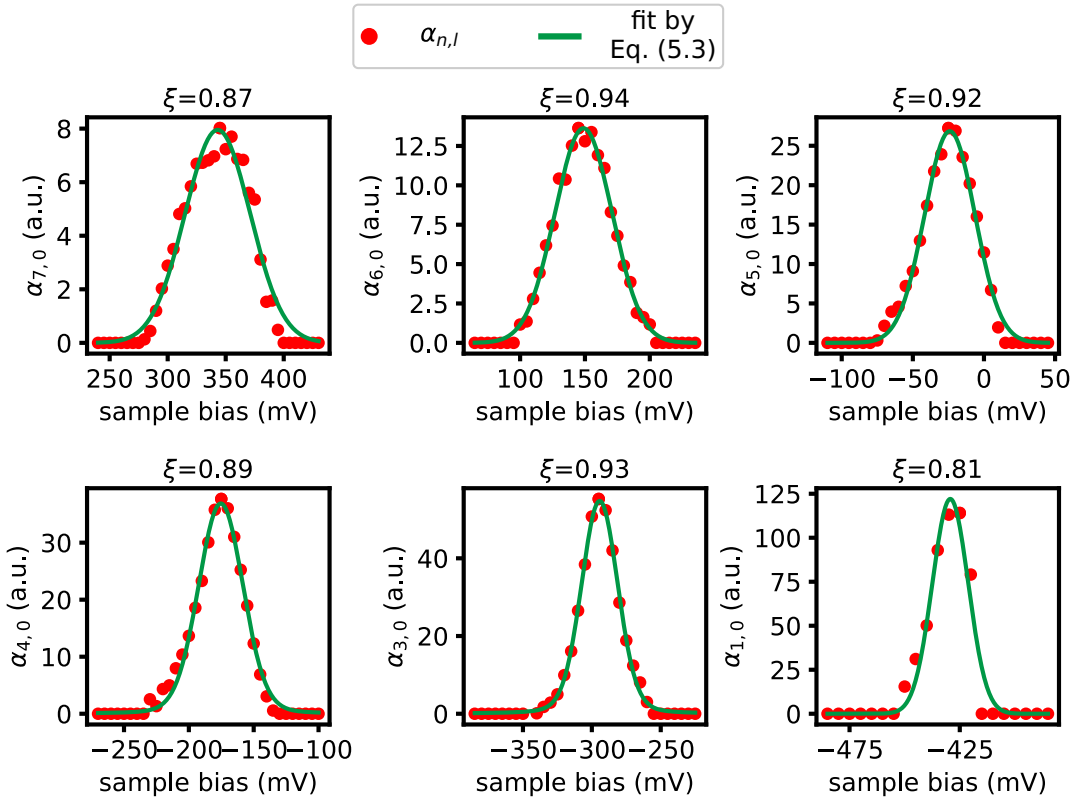


Figure A.4: Energy distributions of the states with $l = 0$ (red markers) fitted with Eq. (5.3) (green line). The quality factor ξ, as described in Subsection 5.1.2, can be found above each plot.

$\alpha_{7,0}$	(meV)
Γ_{wall}	65 ± 7
Γ_{L}	$0 \,^{+}_{(-)}\, 10$
$E_{7,0}$	343.0 ± 0.8

$\alpha_{6,0}$	(meV)
Γ_{wall}	51 ± 2
Γ_{L}	$0 \,^{+}_{(-)}\, 3$
$E_{6,0}$	148.9 ± 0.3

$\alpha_{5,0}$	(meV)
Γ_{wall}	40 ± 2
Γ_{L}	$0 \,^{+}_{(-)}\, 1$
$E_{5,0}$	-24.0 ± 0.3

$\alpha_{4,0}$	(meV)
Γ_{wall}	37 ± 2
Γ_{L}	4 ± 3
$E_{4,0}$	-175.4 ± 0.3

$\alpha_{3,0}$	(meV)
Γ_{wall}	27 ± 1
Γ_{L}	4 ± 1
$E_{3,0}$	-294.3 ± 0.2

$\alpha_{1,0}$	(meV)
Γ_{wall}	16 ± 3
Γ_{L}	$0 \,^{+}_{(-)}\, 1$
$E_{1,0}$	-429.3 ± 0.4

Table A.1: Results for fitting Eq. (5.3) to the reconstructed $l = 0$ energy distributions of the big corral.

A.3.2. $l = 1$ states - big 48-CO corral

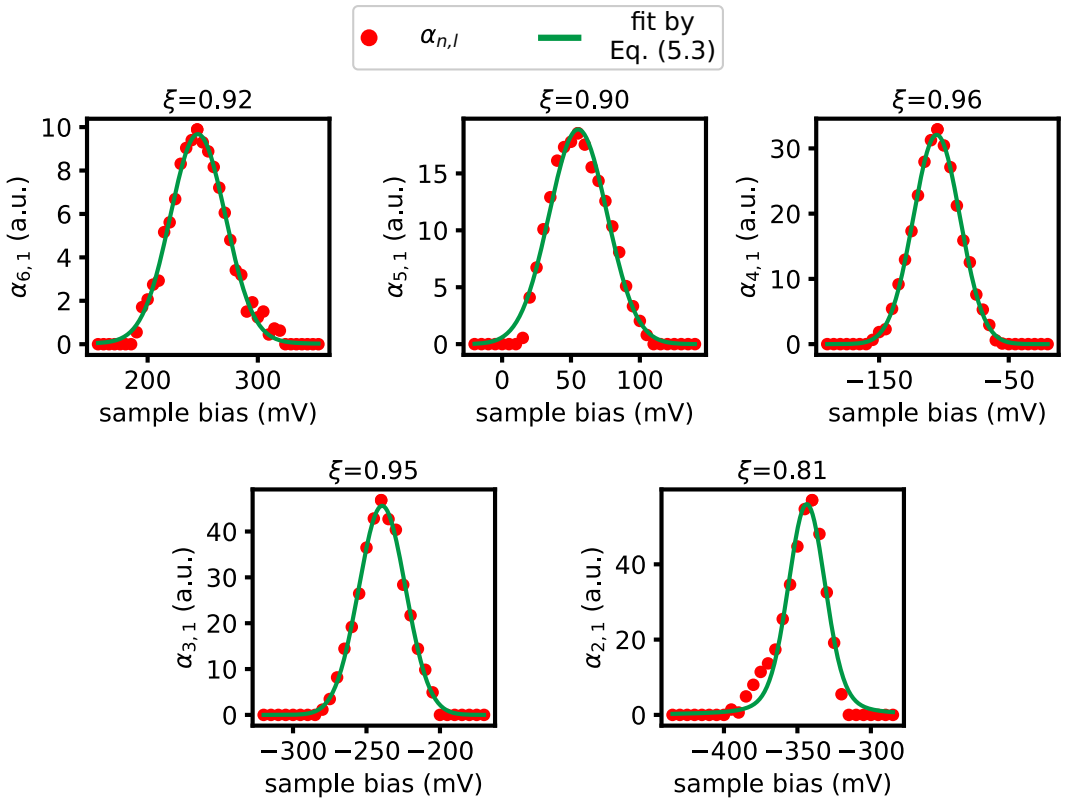


Figure A.5: Energy distributions of the states with $l = 1$ (red markers) fitted with Eq. (5.3) (green line). The quality factor ξ, as described in Subsection 5.1.2, can be found above each plot.

$\alpha_{6,1}$	(meV)
Γ_{wall}	57 ± 3
Γ_{L}	3 ± 3
$E_{6,1}$	245.6 ± 0.4

$\alpha_{5,1}$	(meV)
Γ_{wall}	48 ± 3
Γ_{L}	0 ± 4
$E_{5,1}$	55.2 ± 0.5

$\alpha_{4,1}$	(meV)
Γ_{wall}	41 ± 1
Γ_{L}	0 ± 2
$E_{4,1}$	-105.6 ± 0.2

$\alpha_{3,1}$	(meV)
Γ_{wall}	36 ± 2
Γ_{L}	0 ± 2
$E_{3,1}$	-239.4 ± 0.2

$\alpha_{2,1}$	(meV)
Γ_{wall}	24 ± 3
Γ_{L}	7 ± 4
$E_{2,1}$	-343.6 ± 0.4

Table A.2: Results for fitting Eq. (5.3) to the reconstructed $l = 1$ energy distributions of the big corral.

A.3.3. $l = 2$ states - big 48-CO corral

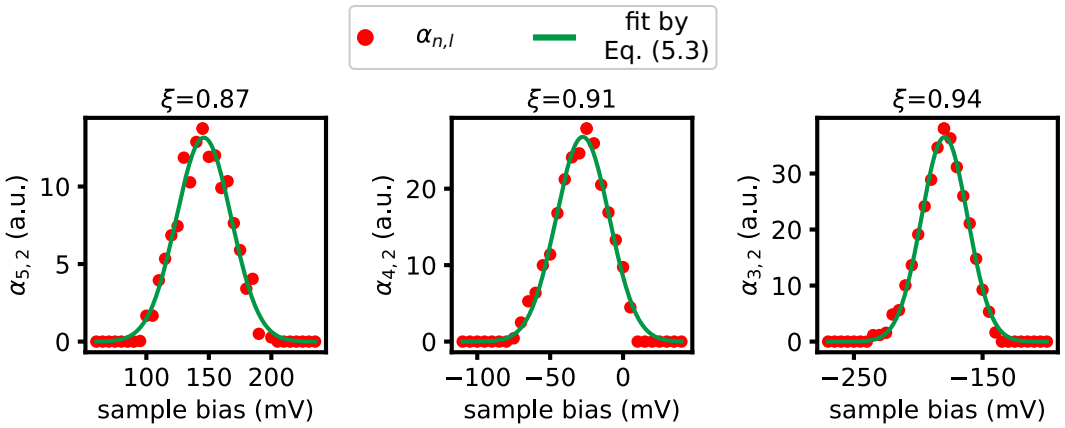


Figure A.6: Energy distributions of the states with $l = 2$ (red markers) fitted with Eq. (5.3) (green line). The quality factor ξ, as described in Subsection 5.1.2, can be found above each plot.

$\alpha_{5,2}$	(meV)
Γ_{wall}	51 ± 4
Γ_{L}	$0 \overset{+}{(-)} 2$
$E_{5,2}$	145.9 ± 0.6

$\alpha_{4,2}$	(meV)
Γ_{wall}	42 ± 3
Γ_{L}	$0 \overset{+}{(-)} 4$
$E_{4,2}$	-27.6 ± 0.4

$\alpha_{3,2}$	(meV)
Γ_{wall}	41 ± 2
Γ_{L}	$0 \overset{+}{(-)} 1$
$E_{3,2}$	-179.5 ± 0.2

Table A.3: Results for fitting Eq. (5.3) to the reconstructed $l = 2$ energy distributions of the big corral.

A.3.4. $l = 3$ states - big 48-CO corral

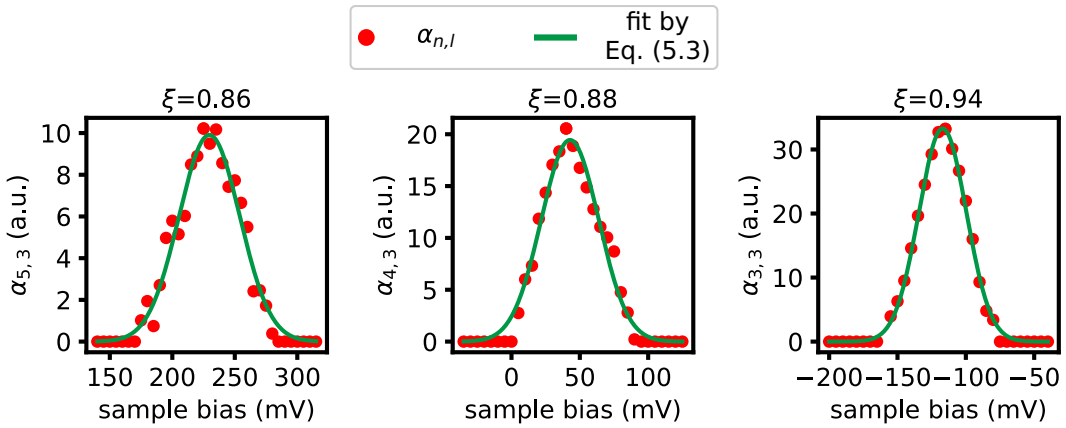


Figure A.7: Energy distributions of the states with $l = 3$ (red markers) fitted with Eq. (5.3) (green line). The quality factor ξ, as described in Subsection 5.1.2, can be found above each plot.

$\alpha_{5,3}$	(meV)
Γ_{wall}	56 ± 5
Γ_{L}	$0 \,{}^{+}_{(-)}\, 1$
$E_{5,3}$	229.6 ± 0.7

$\alpha_{4,3}$	(meV)
Γ_{wall}	48 ± 4
Γ_{L}	$0 \,{}^{+}_{(-)}\, 5$
$E_{4,3}$	42.8 ± 0.6

$\alpha_{3,3}$	(meV)
Γ_{wall}	40 ± 2
Γ_{L}	$0 \,{}^{+}_{(-)}\, 2$
$E_{3,3}$	-117.0 ± 0.2

Table A.4: Results for fitting Eq. (5.3) to the reconstructed $l = 3$ energy distributions of the big corral.

A.3.5. $l = 4$ states - big 48-CO corral

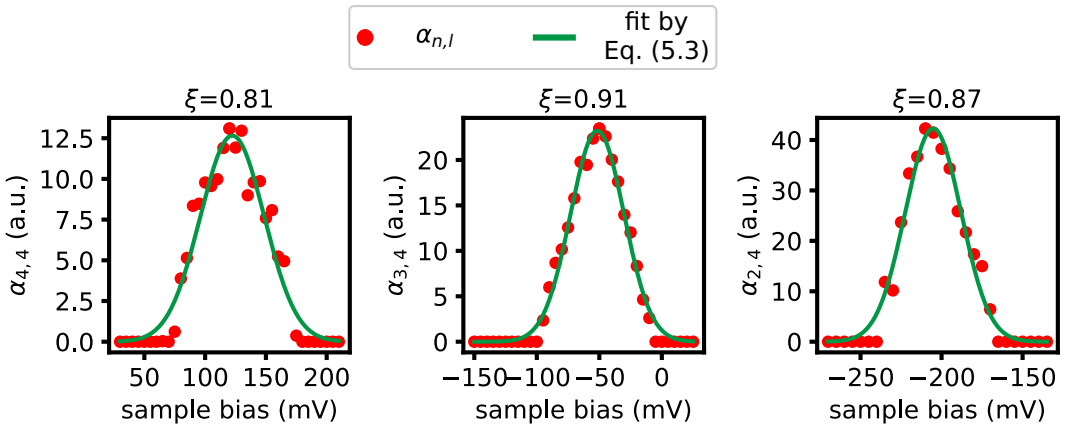


Figure A.8: Energy distributions of the states with $l = 4$ (red markers) fitted with Eq. (5.3) (green line). The quality factor ξ, as described in Subsection 5.1.2, can be found above each plot.

$\alpha_{4,4}$	(meV)
Γ_{wall}	61 ± 7
Γ_{L}	$0 \overset{+}{(-)} 10$
$E_{4,4}$	122 ± 1

$\alpha_{3,4}$	(meV)
Γ_{wall}	49 ± 3
Γ_{L}	$0 \overset{+}{(-)} 4$
$E_{3,4}$	-51.6 ± 0.4

$\alpha_{2,4}$	(meV)
Γ_{wall}	39 ± 4
Γ_{L}	$0 \overset{+}{(-)} 1$
$E_{2,4}$	-205.1 ± 0.5

Table A.5: Results for fitting Eq. (5.3) to the reconstructed $l = 4$ energy distributions of the big corral.

A.3.6. $l = 5$, $l = 6$ and $l = 7$ states - big 48-CO corral

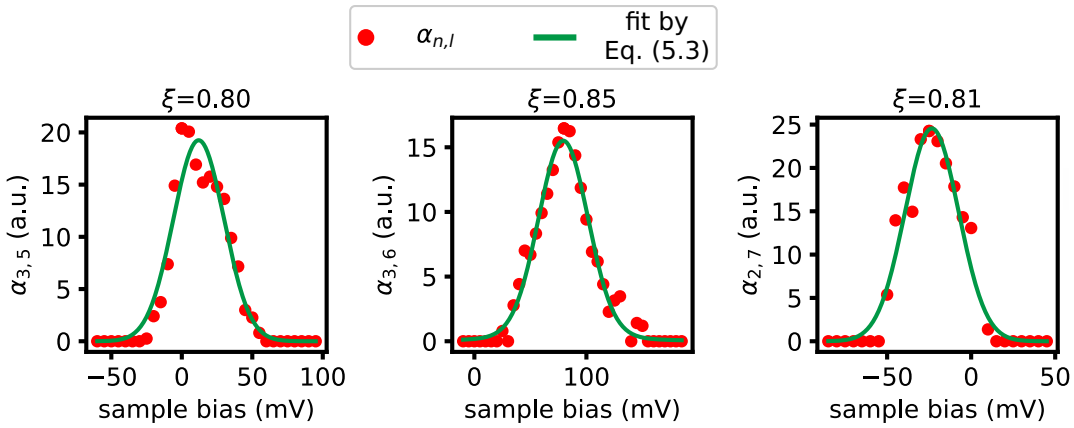


Figure A.9: Energy distributions of the states with $l = 5$, $l = 6$, and $l = 7$ (red markers) fitted with Eq. (5.3) (green line). The quality factor ξ, as described in Subsection 5.1.2, can be found above each plot.

$\alpha_{3,5}$	(meV)
Γ_{wall}	41 ± 5
Γ_{L}	$0\ ^{+}_{(-)}\ 1$
$E_{3,5}$	12.0 ± 0.8

$\alpha_{3,6}$	(meV)
Γ_{wall}	49 ± 4
Γ_{L}	5 ± 5
$E_{3,6}$	79.4 ± 0.6

$\alpha_{2,7}$	(meV)
Γ_{wall}	36 ± 5
Γ_{L}	$0\ ^{+}_{(-)}\ 5$
$E_{2,7}$	-23.4 ± 0.7

Table A.6: Results for fitting Eq. (5.3) to the reconstructed $l = 5$, $l = 6$, and $l = 7$ energy distributions of the big corral.

A.3.7. $l = 0$ states - small 24-CO corral

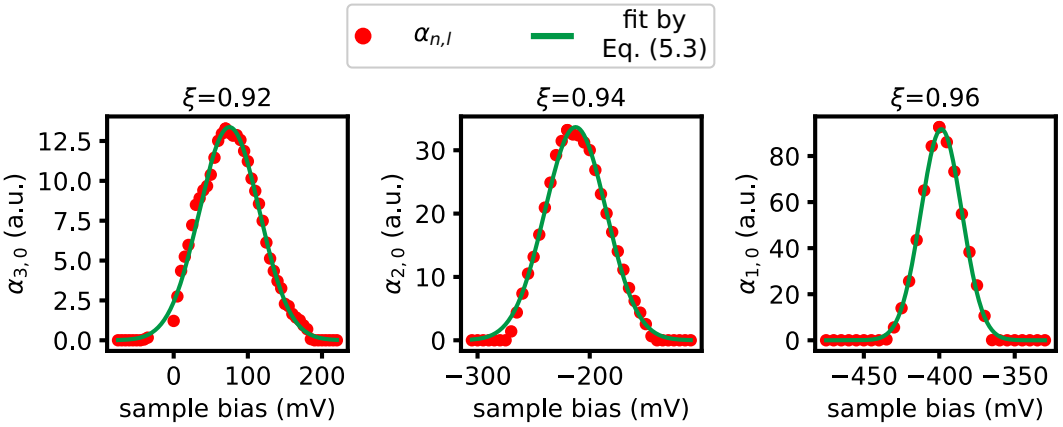


Figure A.10: Energy distributions of the states with $l = 0$ (red markers) fitted with Eq. (5.3) (green line). The quality factor ξ, as described in Subsection 5.1.2, can be found above each plot.

$\alpha_{3,0}$	(meV)
Γ_{wall}	95 ± 5
Γ_{L}	$0\ ^{+}_{(-)}\ 7$
$E_{3,0}$	75.1 ± 0.8

$\alpha_{2,0}$	(meV)
Γ_{wall}	64 ± 3
Γ_{L}	$0\ ^{+}_{(-)}\ 1$
$E_{2,0}$	-212.6 ± 0.4

$\alpha_{1,0}$	(meV)
Γ_{wall}	30 ± 1
Γ_{L}	$0\ ^{+}_{(-)}\ 1$
$E_{1,0}$	-398.6 ± 0.2

Table A.7: Results for fitting Eq. (5.3) to the reconstructed $l = 0$ energy distributions of the small corral.

A.3.8. $l = 1$ states - small 24-CO corral

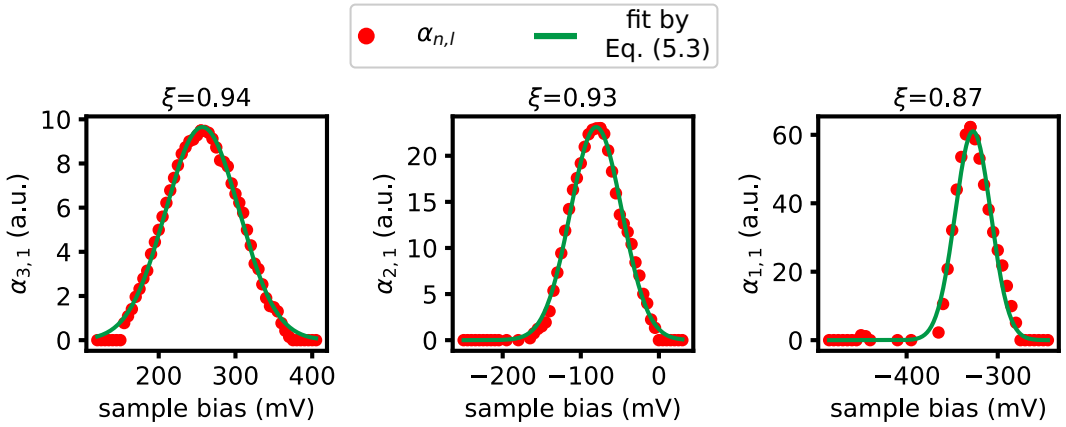


Figure A.11: Energy distributions of the states with $l = 1$ (red markers) fitted with Eq. (5.3) (green line). The quality factor ξ, as described in Subsection 5.1.2, can be found above each plot.

$\alpha_{3,1}$	(meV)
Γ_{wall}	113 ± 5
Γ_{L}	$0\ ^{+}_{(-)}\ 7$
$E_{3,1}$	256.8 ± 0.6

$\alpha_{2,1}$	(meV)
Γ_{wall}	77 ± 3
Γ_{L}	$0\ ^{+}_{(-)}\ 5$
$E_{2,1}$	-80.3 ± 0.5

$\alpha_{1,1}$	(meV)
Γ_{wall}	45 ± 4
Γ_{L}	$0\ ^{+}_{(-)}\ 1$
$E_{1,1}$	-327.2 ± 0.5

Table A.8: Results for fitting Eq. (5.3) to the reconstructed $l = 1$ energy distributions of the small corral.

A.3.9. $l = 2$ and $l = 3$ states - small 24-CO corral

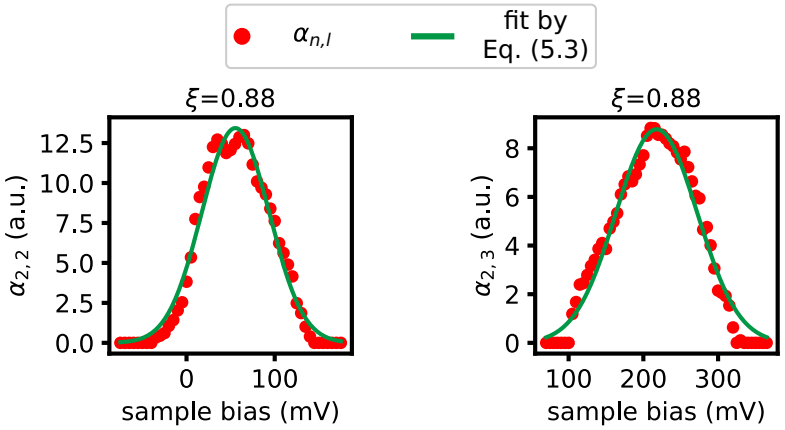


Figure A.12: Energy distributions of the states with $l = 2$ and $l = 3$ (red markers) fitted with Eq. (5.3) (green line). The quality factor ξ, as described in Subsection 5.1.2, can be found above each plot.

$\alpha_{2,2}$	(meV)
Γ_{wall}	49 ± 6
Γ_{L}	$0\ ^{+}_{(-)}\ 1$
$E_{2,2}$	55.4 ± 0.9

$\alpha_{2,3}$	(meV)
Γ_{wall}	128 ± 10
Γ_{L}	$0\ ^{+}_{(-)}\ 14$
$E_{2,3}$	218 ± 2

Table A.9: Results for fitting Eq. (5.3) to the reconstructed $l = 2$ and $l = 3$ energy distributions of the small corral.

A.4. Suppression of the copper grid in constant-height AFM measurements

In constant-height AFM measurements performed with a CO-terminated tip inside the quantum corral, the recorded contrast contains contributions from both the confined Shockley surface state and the atomic lattice of the Cu(111) surface. In the corresponding images, the Cu surface atoms appear as small attractive (dark) features, as shown in Fig. 6.2(a) of the main text.

To make the longer-wavelength contrast associated with the confined Shockley surface state more visible, the high-spatial-frequency contribution of the Cu lattice was reduced by applying a Gaussian low-pass filter. Following a procedure similar to that used in Ref. [17], each AFM image was first transformed into reciprocal space by means of a fast Fourier transformation (FFT). In Fourier space, the image was multiplied by a two-dimensional Gaussian kernel (in the k_x and k_y directions) in order to attenuate the high-frequency components. The filtered image was then transformed back into real space using the inverse FFT.

This filtering procedure was applied twice in succession, i.e., FFT $\rightarrow$ Gaussian filtering $\rightarrow$ inverse FFT, followed by a second repetition of the same sequence. Performing the filtering in two consecutive steps allowed for a controlled reduction of the Cu grid while preserving the larger-scale contrast of interest.

The Gaussian filter width is specified in pixels by the full width at half maximum in the k_x and k_y directions. All AFM images analyzed here contain between (192×192) pixels and (208×208) pixels. For images recorded with a CO-tip, filtering was required to suppress the Cu grid, and the two-step procedure was carried out using a Gaussian kernel with a width of 12 pixels. By contrast, images acquired with a metal-tip did not exhibit a visible Cu grid. In that case, the same two-step filtering scheme was used only for mild smoothing of the data, employing a Gaussian kernel with a width of 20 pixels.

A.5. Multiple scattering simulation and effective mass

Previous studies on semiconductor quantum dots have shown that the effective electron mass can depend on the size of the confined structure [147]. In smaller quantum dots, larger values of the effective mass were reported, indicating that the effective mass may depend on the geometric dimensions and confinement strength of the system.

To determine the confined effective mass in the square quantum corral investigated in Chapter 6, multiple scattering simulations in the black-dot limit [24] were compared with differential conductance measurements, $\mathrm{d}I/\mathrm{d}V$, recorded inside the corral. Spectra were acquired at two positions: at the center of the corral, $(x, y) = (0\,\mathrm{nm}, 0\,\mathrm{nm})$, and at an off-center position, $(x, y) = (0.53\,\mathrm{nm}, 0.53\,\mathrm{nm})$. The corresponding measurements and simulations are shown in Fig. A.13. To minimize the remaining influence of the tip density of states, the local density of states of the sample was extracted from the measured spectra using the full deconvolution method introduced by Wahl *et al.* [124].

The best agreement between experiment and simulation was obtained for a confined effective mass of $m^*_{\mathrm{e,conf.}} = 0.45 \cdot m_\mathrm{e}$, where m_e denotes the free electron mass. This value is slightly larger than the reported range for the unconfined Shockley surface state on Cu(111), $m^*_{\mathrm{e,free}} = (0.405 \pm 0.025) \cdot m_\mathrm{e}$ (e.g., Refs. [15, 47, 69–73]), indicating that confinement inside the corral leads to a small increase in the effective mass.

This result is also consistent with previous theoretical work on square corrals on Cu(111). Freeney *et al.* [82] obtained values of $0.48 \cdot m_\mathrm{e}$ and $0.46 \cdot m_\mathrm{e}$ using a muffin-tin model, which are close to the value found here.

Within the multiple scattering formalism, the spatially resolved local density of states can be calculated as a function of the energy of the surface-state electrons. By integrating the simulated LDOS from the onset of the Shockley surface state up to the Fermi level, a quantity proportional to the total surface charge density σ_tot is obtained.

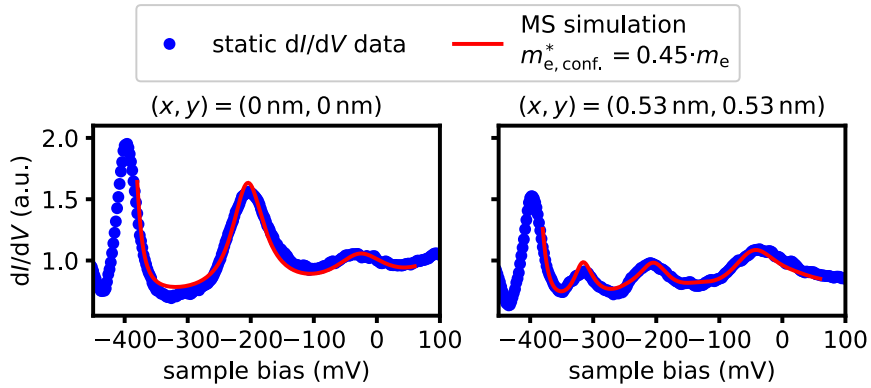


Figure A.13: Comparison of $\mathrm{d}I/\mathrm{d}V$ spectra (blue markers) with multiple scattering (MS) simulations (solid red line). The best agreement between experiment and simulation was obtained for a confined effective electron mass of $m^*_{\mathrm{e,conf.}} = 0.45 \cdot m_\mathrm{e}$.

A.6. Experimental force contrast measured with a second CO-tip and a second metal-tip over a square-shaped quantum corral

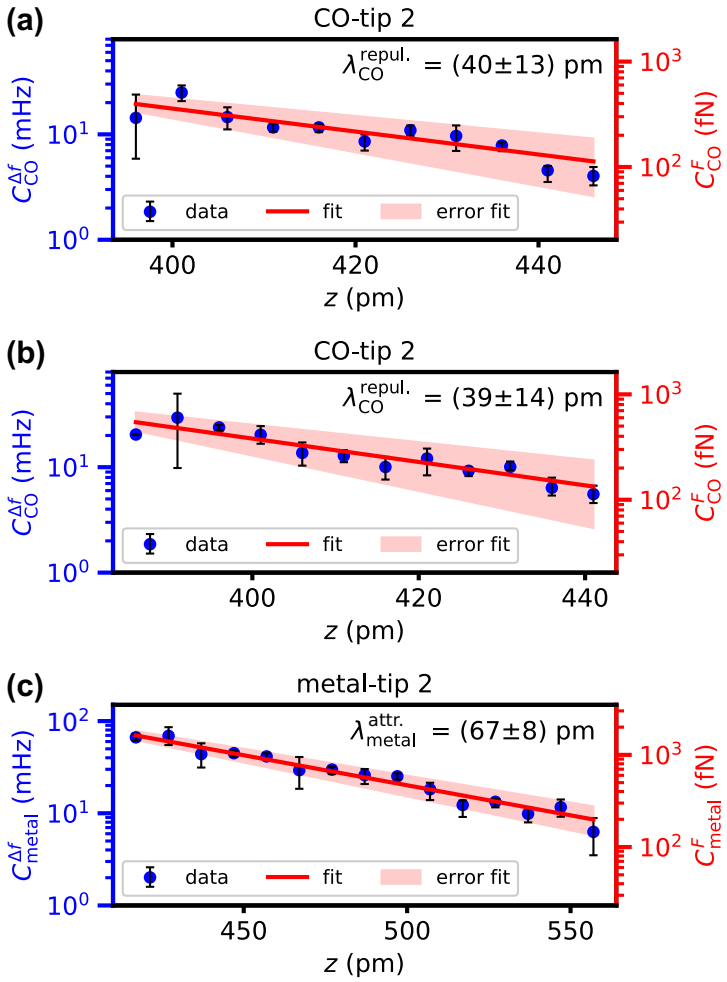


Figure A.14: Contrast in Δf and F measured with a second CO-tip and a second metal-tip, as a function of tip-sample separation z. The two CO-tip measurements yield $\lambda_{\mathrm{CO,(a)}}^{\mathrm{repul.}} = (40 \pm 13)\,\mathrm{pm}$ and $\lambda_{\mathrm{CO,(b)}}^{\mathrm{repul.}} = (39 \pm 14)\,\mathrm{pm}$. The metal-tip measurement yields $\lambda_{\mathrm{metal}}^{\mathrm{attr.}} = (67 \pm 8)\,\mathrm{pm}$. To show reproducibility of the measurement technique itself, the contrast evolution was determined twice with the same CO-tip.

A.7. Analytical solution of the overlap integral

To model the repulsive and attractive interactions between the AFM tip and the corral states, overlap integrals are used in Section 6.2. In the following, the analytical solution of the overlap integrals is presented using normalized s-waves:

$$\Psi_{\mathrm{A/B}}(\vec{r}) = \frac{1}{\sqrt{\pi(\lambda^{\Psi}_{\mathrm{A/B}})^3}} \exp\left(-\frac{|\vec{r} - \vec{R}_{\mathrm{A/B}}|}{\lambda^{\Psi}_{\mathrm{A/B}}}\right). \tag{A.1}$$

The centers of the respective wave functions are given by $\vec{R}_{\mathrm{A}}$ and $\vec{R}_{\mathrm{B}}$, while $\lambda^{\Psi}_{\mathrm{A}}$ and $\lambda^{\Psi}_{\mathrm{B}}$ describe the decay lengths of the wave functions. The overlap integral S is defined as

$$S = \int \Psi_{\mathrm{A}}(\vec{r})\Psi_{\mathrm{B}}(\vec{r})\mathrm{d}\vec{r}. \tag{A.2}$$

This integral can be solved in a straightforward way by using $R = |\vec{R}_{\mathrm{A}} - \vec{R}_{\mathrm{B}}|$, which describes the distance between the two centers of the wave functions, and elliptical coordinates:

$$\mu = \frac{|\vec{r} - \vec{R}_{\mathrm{A}}| + |\vec{r} - \vec{R}_{\mathrm{B}}|}{R} \quad \text{and} \quad \nu = \frac{|\vec{r} - \vec{R}_{\mathrm{A}}| - |\vec{r} - \vec{R}_{\mathrm{B}}|}{R}. \tag{A.3}$$

The differential volume element is then given by [153]

$$\mathrm{d}\vec{r} = \frac{R^3}{8}(\mu^2 - \nu^2)\,\mathrm{d}\mu\,\mathrm{d}\nu\,\mathrm{d}\varphi, \tag{A.4}$$

with $1 \leq \mu < \infty$, $-1 \leq \nu \leq 1$, and $0 \leq \varphi \leq 2\pi$ [153]. The analytical solution of the overlap integral is

$$S = \begin{cases} \left(1 + \dfrac{R}{\lambda^{\Psi}} + \dfrac{R^2}{3(\lambda^{\Psi})^2}\right)\exp\left(-\dfrac{R}{\lambda^{\Psi}}\right) & \text{if } \lambda^{\Psi}_{\mathrm{A}} = \lambda^{\Psi}_{\mathrm{B}} = \lambda^{\Psi} \\ \chi[S_1 S_2 - S_3 S_4] & \text{if } \lambda^{\Psi}_{\mathrm{A}} \neq \lambda^{\Psi}_{\mathrm{B}} \end{cases} \tag{A.5}$$

with

$$\chi = \frac{R^3}{4}\left(\frac{1}{\lambda^{\Psi}_{\mathrm{A}}}\right)^{3/2}\left(\frac{1}{\lambda^{\Psi}_{\mathrm{B}}}\right)^{3/2},$$

$$
\begin{aligned}
S_1 &= \frac{(K_\mathrm{p}^2 + 2K_\mathrm{p} + 2)\exp(-K_\mathrm{p})}{K_\mathrm{p}^3}, \\
S_2 &= \frac{\exp(K_\mathrm{m}) - \exp(-K_\mathrm{m})}{K_\mathrm{m}}, \\
S_3 &= \frac{\exp(-K_\mathrm{p})}{K_\mathrm{p}}, \\
S_4 &= \frac{\exp(-K_\mathrm{m})\Big[(K_\mathrm{m}^2 - 2K_\mathrm{m} + 2)\exp(2K_\mathrm{m}) - K_\mathrm{m}^2 - 2K_\mathrm{m} - 2\Big]}{K_\mathrm{m}^3}
\end{aligned}
$$

and

$$
\begin{aligned}
K_\mathrm{p} &= \frac{R}{2\lambda_\mathrm{A}^\Psi} + \frac{R}{2\lambda_\mathrm{B}^\Psi}, \\
K_\mathrm{m} &= \frac{R}{2\lambda_\mathrm{A}^\Psi} - \frac{R}{2\lambda_\mathrm{B}^\Psi}.
\end{aligned}
$$

To adapt Eq. (A.5) for electron density (ρ) overlaps, one must consider that the decay length of the electron density (λ^ρ) is half the decay length of the corresponding wave function (λ^Ψ). This follows directly from $|\Psi|^2 \propto \rho$. Squaring the exponential term $|\exp(-|r|/\lambda^\Psi)|^2$ results in $\exp(-(2|r|)/\lambda^\Psi) = \exp(-|r|/\lambda^\rho)$, where $\lambda^\rho = \lambda^\Psi/2$. Additionally, specific scaling factors must be applied when using Eq. (A.5) for density-based calculations:

- $\dfrac{1}{64\pi}\left(\dfrac{1}{\lambda^\rho}\right)^{3/2}\left(\dfrac{1}{\lambda^\rho}\right)^{3/2}$ when $\lambda_\mathrm{A}^\rho = \lambda_\mathrm{B}^\rho = \lambda^\rho$
- $\dfrac{1}{64\pi}\left(\dfrac{1}{\lambda_\mathrm{A}^\rho}\right)^{3/2}\left(\dfrac{1}{\lambda_\mathrm{B}^\rho}\right)^{3/2}$ when $\lambda_\mathrm{A}^\rho \neq \lambda_\mathrm{B}^\rho$.

A.8. Single-exponential fit to the attractive branch of a Morse-type interaction

The Morse potential, commonly used to describe the interaction between two atoms, consists of two exponential contributions: one repulsive and one attractive. The corresponding force therefore also consists of two exponential parts:

$$F_{\mathrm{Morse}}(z) = A \exp\left(-\frac{z}{\lambda_{\mathrm{Morse}}^{\mathrm{repul.}}}\right) - B \exp\left(-\frac{z}{\lambda_{\mathrm{Morse}}^{\mathrm{attr.}}}\right) \tag{A.6}$$

$$= \exp\left(-\frac{z}{\lambda_{\mathrm{Morse}}^{\mathrm{repul.}}}\right)\left(A - B \exp\left[-z\frac{\lambda_{\mathrm{Morse}}^{\mathrm{repul.}} - \lambda_{\mathrm{Morse}}^{\mathrm{attr.}}}{\lambda_{\mathrm{Morse}}^{\mathrm{repul.}}\lambda_{\mathrm{Morse}}^{\mathrm{attr.}}}\right]\right), \tag{A.7}$$

where A and B are positive prefactors, $\lambda_{\mathrm{Morse}}^{\mathrm{repul.}}$ denotes the decay length of the repulsive component, and $\lambda_{\mathrm{Morse}}^{\mathrm{attr.}}$ the decay length of the attractive component. The AFM measurements were conducted at the position $z = z_0 + \epsilon$, where z_0 denotes the base height of the measurement, and ϵ the relative displacement. Inserting this into Eq. (A.7) gives

$$F_{\mathrm{Morse}}(z_0+\epsilon) = \exp\left(-\frac{z_0+\epsilon}{\lambda_{\mathrm{Morse}}^{\mathrm{repul.}}}\right)\left(A - B \exp\left[-(z_0+\epsilon)\frac{\lambda_{\mathrm{Morse}}^{\mathrm{repul.}} - \lambda_{\mathrm{Morse}}^{\mathrm{attr.}}}{\lambda_{\mathrm{Morse}}^{\mathrm{repul.}}\lambda_{\mathrm{Morse}}^{\mathrm{attr.}}}\right]\right). \tag{A.8}$$

Here, it is assumed that the full force curve between the corral states and the tip follows a Morse-type interaction (first attractive, then repulsive). However, the experimental data for the metal-tip measurements can only be fitted with a single exponential function in the attractive regime. This can be expressed as

$$\begin{aligned} F_{\mathrm{Morse}}(z_0+\epsilon) &= \underbrace{\exp\left(-\frac{z_0+\epsilon}{\lambda_{\mathrm{Morse}}^{\mathrm{repul.}}}\right)\left(A - B \exp\left[-(z_0+\epsilon)\frac{\lambda_{\mathrm{Morse}}^{\mathrm{repul.}} - \lambda_{\mathrm{Morse}}^{\mathrm{attr.}}}{\lambda_{\mathrm{Morse}}^{\mathrm{repul.}}\lambda_{\mathrm{Morse}}^{\mathrm{attr.}}}\right]\right)}_{\text{Eq. (A.8)}} \\ &\approx \underbrace{-C \exp\left(-\frac{z_0+\epsilon}{\lambda_{\mathrm{fit}}^{\mathrm{attr.}}}\right)}_{\text{fit function}}. \end{aligned} \tag{A.9}$$

In this equation, the left-hand side (first row) describes the actual Morse-type force, while the right-hand side (second row) gives the single exponential function used for fitting. The constant C is positive and denotes the amplitude of the fitted function.

The general goal of this derivation is to see how the fitted decay length $\lambda_{\text{fit}}^{\text{attr.}}$ relates to the true attractive decay length $\lambda_{\text{Morse}}^{\text{attr.}}$. Before applying a natural logarithm, both sides of Eq. (A.9) are multiplied by -1 since the measured forces with a metal-tip are clearly attractive ($F < 0$). This leads to the following expression:

$$\begin{aligned}\ln\Big(-F_{\text{Morse}}(z_0+\epsilon)\Big) &= \underbrace{-\frac{z_0+\epsilon}{\lambda_{\text{Morse}}^{\text{repul.}}} + \ln\left(-A + B\exp\left[-(z_0+\epsilon)\frac{\lambda_{\text{Morse}}^{\text{repul.}} - \lambda_{\text{Morse}}^{\text{attr.}}}{\lambda_{\text{Morse}}^{\text{repul.}}\lambda_{\text{Morse}}^{\text{attr.}}}\right]\right)}_{\substack{\text{logarithmic form}\\ \text{of Eq. (A.8)}}} \\ &\approx \underbrace{\ln(C) - \frac{z_0+\epsilon}{\lambda_{\text{fit}}^{\text{attr.}}}}_{\substack{\text{logarithmic form}\\ \text{of fit function}}}.\end{aligned} \tag{A.10}$$

A Taylor expansion of the ln-term in the logarithmic form of the full Morse curve [first row of Eq. (A.10)] around $\epsilon = 0$ yields

$$\begin{aligned}\ln\Big(-F_{\text{Morse}}(z_0+\epsilon)\Big) = &-\frac{z_0}{\lambda_{\text{Morse}}^{\text{repul.}}} - \frac{\epsilon}{\lambda_{\text{Morse}}^{\text{repul.}}} + \ln\left(-A + B\exp\left[-z_0\frac{\lambda_{\text{Morse}}^{\text{repul.}} - \lambda_{\text{Morse}}^{\text{attr.}}}{\lambda_{\text{Morse}}^{\text{repul.}}\lambda_{\text{Morse}}^{\text{attr.}}}\right]\right) \\ &+ \frac{B}{A\exp\left(z_0\frac{\lambda_{\text{Morse}}^{\text{repul.}} - \lambda_{\text{Morse}}^{\text{attr.}}}{\lambda_{\text{Morse}}^{\text{repul.}}\lambda_{\text{Morse}}^{\text{attr.}}}\right) - B}\frac{\lambda_{\text{Morse}}^{\text{repul.}} - \lambda_{\text{Morse}}^{\text{attr.}}}{\lambda_{\text{Morse}}^{\text{repul.}}\lambda_{\text{Morse}}^{\text{attr.}}}\epsilon + \mathcal{O}(\epsilon^2).\end{aligned} \tag{A.11}$$

To simplify this expression and to better compare it to the logarithmic form of the fit function [see second row in Eq. (A.10)], the general ratio $\mu = \lambda_{\text{Morse}}^{\text{attr.}}/\lambda_{\text{Morse}}^{\text{repul.}}$ with $\mu > 1$ is introduced, and all terms independent of ϵ are combined into an offset:

$$\ln\Big(-F_{\text{Morse}}(z_0+\epsilon)\Big) = \left(-\frac{\mu}{\lambda_{\text{Morse}}^{\text{attr.}}} + \kappa(z_0)\right)\epsilon + \text{offset} + \mathcal{O}(\epsilon^2), \tag{A.12}$$

with

$$\kappa(z_0) = \frac{B}{A\exp\left(z_0\frac{1-\mu}{\lambda_{\text{Morse}}^{\text{attr.}}}\right) - B}\cdot\frac{1-\mu}{\lambda_{\text{Morse}}^{\text{attr.}}}. \tag{A.13}$$

By comparing the coefficients of ϵ in Eq. (A.12) and the ln-form of the fit function [see second row in Eq. (A.10)], a relation between the fitted decay length $\lambda_{\text{fit}}^{\text{attr.}}$ and

the true attractive decay length $\lambda_{\mathrm{Morse}}^{\mathrm{attr.}}$ can be found:

$$\frac{1}{\lambda_{\mathrm{fit}}^{\mathrm{attr.}}} = \frac{\mu}{\lambda_{\mathrm{Morse}}^{\mathrm{attr.}}} - \kappa(z_0). \tag{A.14}$$

This relation shows that the fitted decay length $\lambda_{\mathrm{fit}}^{\mathrm{attr.}}$ generally differs from the true attractive decay length $\lambda_{\mathrm{Morse}}^{\mathrm{attr.}}$ through the correction term $\kappa(z_0)$, which depends on the measurement height z_0.
In the limit of a large tip-sample separation ($z_0 \to \infty$), where the repulsive part of the Morse-type interaction becomes negligible, the correction term [see Eq. (A.13)] becomes

$$\kappa(z_0 \to \infty) = -\frac{1-\mu}{\lambda_{\mathrm{Morse}}^{\mathrm{attr.}}}, \tag{A.15}$$

which, when inserted into Eq. (A.14), leads to

$$\frac{1}{\lambda_{\mathrm{fit}}^{\mathrm{attr.}}} = \frac{\mu}{\lambda_{\mathrm{Morse}}^{\mathrm{attr.}}} + \frac{1-\mu}{\lambda_{\mathrm{Morse}}^{\mathrm{attr.}}} = \frac{1}{\lambda_{\mathrm{Morse}}^{\mathrm{attr.}}} \quad \Rightarrow \quad \lambda_{\mathrm{fit}}^{\mathrm{attr.}} = \lambda_{\mathrm{Morse}}^{\mathrm{attr.}}. \tag{A.16}$$

This shows that the fitted decay length only matches the true attractive decay length in the limit of a large tip-sample separation. Another important point is the minimum of the Morse-type interaction curve, which is located at

$$z_{\mathrm{min}} = -\frac{\lambda_{\mathrm{Morse}}^{\mathrm{attr.}}}{1-\mu} \ln\left(\frac{\mu A}{B}\right). \tag{A.17}$$

At this position, the correction term in Eq. (A.13) becomes

$$\kappa(z_{\mathrm{min}}) = \frac{\mu}{\lambda_{\mathrm{Morse}}^{\mathrm{attr.}}}, \tag{A.18}$$

which, when inserted into Eq. (A.14), leads to

$$\frac{1}{\lambda_{\mathrm{fit}}^{\mathrm{attr.}}} = 0 \quad \Rightarrow \quad \lambda_{\mathrm{fit}}^{\mathrm{attr.}} = \infty. \tag{A.19}$$

Since the correction term $\kappa(z_0)$ is monotonic between these two critical points (at large separation and at the minimum of the Morse-type interaction curve), this

defines the boundaries for the fitted decay length:

$$\lambda_{\text{fit}}^{\text{attr.}} \in [\lambda_{\text{Morse}}^{\text{attr.}}, \infty), \tag{A.20}$$

which yields the central result:

$$\lambda_{\text{fit}}^{\text{attr.}} \geq \lambda_{\text{Morse}}^{\text{attr.}}. \tag{A.21}$$

List of Publications

The following list contains all publications to which the author contributed as first author or co-author.

- F. Stilp, M. Weiss, and F. J. Giessibl, *Visualizing the effect of engineered internal perturbations on an artificial 2D atom and explaining it using perturbation theory*, New Journal of Physics, accepted (2026).
- M. Weiss, F. Stilp, F. Huber, and F. J. Giessibl, *Electrostatic origin of multi-non-monotonic forces above single Ho, Gd, and Fe adatoms on Cu(111) revealed by atomic force microscopy*, Physical Review B **113**, 245402 (2026).
- M. Weiss, F. Stilp, M. Reinhart, and F. J. Giessibl, *Measurement and qualitative explanation of the decay lengths of attractive and repulsive forces between natural and artificial atoms*, Physical Review B **112**, 205413 (2025).
- M. Weiss, M. Schelchshorn, F. Stilp, A. J. Weymouth, and F. J. Giessibl, *Increasing the lifetime of confined electronic states in an artificial quantum structure*, Physical Review B **109**, 235422 (2024).
- M. Schelchshorn, F. Stilp, M. Weiss, and F. J. Giessibl, *On the origin and elimination of cross coupling between tunneling current and excitation in scanning probe experiments that utilize the qPlus sensor*, Review of Scientific Instruments **94**, 113704 (2023).

Bibliography

[1] D. M. Eigler and E. K. Schweizer, *Positioning single atoms with a scanning tunnelling microscope*, Nature **344**, 524 (1990).

[2] K. K. Gomes, W. Mar, W. Ko, F. Guinea, and H. C. Manoharan, *Designer Dirac fermions and topological phases in molecular graphene*, Nature **483**, 306 (2012).

[3] M. R. Slot, T. S. Gardenier, P. H. Jacobse, G. C. P. van Miert, S. N. Kempkes, S. J. M. Zevenhuizen, C. Morais Smith, D. Vanmaekelbergh, and I. Swart, *Experimental realization and characterization of an electronic Lieb lattice*, Nature Physics **13**, 672 (2017).

[4] R. Drost, T. Ojanen, A. Harju, and P. Liljeroth, *Topological states in engineered atomic lattices*, Nature Physics **13**, 668 (2017).

[5] S. N. Kempkes, M. R. Slot, J. J. van den Broeke, P. Capiod, W. A. Benalcazar, D. Vanmaekelbergh, D. Bercioux, I. Swart, and C. Morais Smith, *Robust zero-energy modes in an electronic higher-order topological insulator*, Nature Materials **18**, 1292 (2019).

[6] S. N. Kempkes, P. Capiod, S. Ismaili, J. Mulkens, L. Eek, I. Swart, and C. Morais Smith, *Compact localized boundary states in a quasi-1D electronic diamond-necklace chain*, Quantum Frontiers **2**, 1 (2023).

[7] S. E. Freeney, J. J. van den Broeke, A. J. J. Harsveld van der Veen, I. Swart, and C. Morais Smith, *Edge-dependent topology in Kekulé lattices*, Physical Review Letters **124**, 236404 (2020).

[8] C. F. Hirjibehedin, C. P. Lutz, and A. J. Heinrich, *Spin coupling in engineered atomic structures*, Science **312**, 1021 (2006).

[9] D. Serrate, P. Ferriani, Y. Yoshida, S.-W. Hla, M. Menzel, K. von Bergmann, S. Heinze, A. Kubetzka, and R. Wiesendanger, *Imaging and manipulating the spin direction of individual atoms*, Nature Nanotechnology **5**, 350 (2010).

[10] T. Esat, D. Borodin, J. Oh, A. J. Heinrich, F. S. Tautz, Y. Bae, and R. Temirov, *A quantum sensor for atomic-scale electric and magnetic fields*, Nature Nanotechnology **19**, 1466 (2024).

[11] A. J. Heinrich, C. P. Lutz, J. A. Gupta, and D. M. Eigler, *Molecule cascades*, Science **298**, 1381 (2002).

[12] A. A. Khajetoorians, J. Wiebe, B. Chilian, and R. Wiesendanger, *Realizing all-spin–based logic operations atom by atom*, Science **332**, 1062 (2011).

[13] C. R. Moon, L. S. Mattos, B. K. Foster, G. Zeltzer, and H. C. Manoharan, *Quantum holographic encoding in a two-dimensional electron gas*, Nature Nanotechnology **4**, 167 (2009).

[14] F. E. Kalff, M. P. Rebergen, E. Fahrenfort, J. Girovsky, R. Toskovic, J. L. Lado, J. Fernández-Rossier, and A. F. Otte, *A kilobyte rewritable atomic memory*, Nature Nanotechnology **11**, 926 (2016).

[15] M. F. Crommie, C. P. Lutz, and D. M. Eigler, *Imaging standing waves in a two-dimensional electron gas*, Nature **363**, 524 (1993).

[16] M. A. Kastner, *Artificial atoms*, Physics Today **46**, 24 (1993).

[17] F. Stilp, A. Bereczuk, J. Berwanger, N. Mundigl, K. Richter, and F. J. Giessibl, *Very weak bonds to artificial atoms formed by quantum corrals*, Science **372**, 1196 (2021).

[18] G. Schedelbeck, W. Wegscheider, M. Bichler, and G. Abstreiter, *Coupled quantum dots fabricated by cleaved edge overgrowth: from artificial atoms to molecules*, Science **278**, 1792 (1997).

[19] J.-P. Jahn, M. Munsch, L. Béguin, A. V. Kuhlmann, M. Renggli, Y. Huo, F. Ding, R. Trotta, M. Reindl, O. G. Schmidt, A. Rastelli, P. Treutlein, and R. J. Warburton, *An artificial Rb atom in a semiconductor with lifetime-limited linewidth*, Physical Review B **92**, 245439 (2015).

[20] R. Pisoni, Z. Lei, P. Back, M. Eich, H. Overweg, Y. Lee, K. Watanabe, T. Taniguchi, T. Ihn, and K. Ensslin, *Gate-tunable quantum dot in a high*

quality single layer MoS_2 van der Waals heterostructure, Applied Physics Letters **112**, 123101 (2018).

[21] J. Kliewer, R. Berndt, E. V. Chulkov, V. M. Silkin, P. M. Echenique, and S. Crampin, *Dimensionality effects in the lifetime of surface states*, Science **288**, 1399 (2000).

[22] K.-F. Braun and K.-H. Rieder, *Engineering electronic lifetimes in artificial atomic structures*, Physical Review Letters **88**, 096801 (2002).

[23] S. Crampin, H. Jensen, J. Kröger, L. Limot, and R. Berndt, *Resonator design for use in scanning tunneling spectroscopy studies of surface electron lifetimes*, Physical Review B **72**, 035443 (2005).

[24] E. J. Heller, M. F. Crommie, C. P. Lutz, and D. M. Eigler, *Scattering and absorption of surface electron waves in quantum corrals*, Nature **369**, 464 (1994).

[25] T. D. Ladd, F. Jelezko, R. Laflamme, Y. Nakamura, C. Monroe, and J. L. O'Brien, *Quantum computers*, Nature **464**, 45 (2010).

[26] S. Pezzagna and J. Meijer, *Quantum computer based on color centers in diamond*, Applied Physics Reviews **8**, 011308 (2021).

[27] S. Gao, S.-Y. Yin, Z.-X. Liu, Z.-D. Zhang, Z.-N. Tian, Q.-D. Chen, N.-K. Chen, and H.-B. Sun, *Narrow-linewidth diamond single-photon sources prepared via femtosecond laser*, Applied Physics Letters **120**, 023104 (2022).

[28] E. Sierda, X. Huang, D. I. Badrtdinov, B. Kiraly, E. J. Knol, G. C. Groenenboom, M. I. Katsnelson, M. Rösner, D. Wegner, and A. A. Khajetoorians, *Quantum simulator to emulate lower-dimensional molecular structure*, Science **380**, 1048 (2023).

[29] G. Binnig, C. F. Quate, and C. Gerber, *Atomic force microscope*, Physical Review Letters **56**, 930 (1986).

[30] M. Emmrich, F. Huber, F. Pielmeier, J. Welker, T. Hofmann, M. Schneiderbauer, D. Meuer, S. Polesya, S. Mankovsky, D. Ködderitzsch, H. Ebert, and

F. J. Giessibl, *Subatomic resolution force microscopy reveals internal structure and adsorption sites of small iron clusters*, Science **348**, 308 (2015).

[31] F. Huber, J. Berwanger, S. Polesya, S. Mankovsky, H. Ebert, and F. J. Giessibl, *Chemical bond formation showing a transition from physisorption to chemisorption*, Science **366**, 235 (2019).

[32] F. Huber, *Tieftemperatur-Rasterkraftmikroskopie mit funktionalisierten Spitzen an einzelnen Adatomen*, PhD thesis, Universität Regensburg (2018).

[33] R. García and R. Pérez, *Dynamic atomic force microscopy methods*, Surface Science Reports **47**, 197 (2002).

[34] F. J. Giessibl, *Advances in atomic force microscopy*, Reviews of Modern Physics **75**, 949 (2003).

[35] F. J. Giessibl, *The qPlus sensor, a powerful core for the atomic force microscope*, Review of Scientific Instruments **90**, 011101 (2019).

[36] S. Morita, R. Wiesendanger, and E. Meyer, *Noncontact atomic force microscopy*, Springer Verlag, Berlin (2002).

[37] S. Morita, F. J. Giessibl, and R. Wiesendanger, *Noncontact atomic force microscopy, Volume 2*, Springer Verlag, Berlin (2009).

[38] S. Morita, F. J. Giessibl, E. Meyer, and R. Wiesendanger, *Noncontact atomic force microscopy, Volume 3*, Springer Verlag, Berlin (2015).

[39] T. R. Albrecht, P. Grütter, D. Horne, and D. Rugar, *Frequency modulation detection using high-Q cantilevers for enhanced force microscope sensitivity*, Journal of Applied Physics **69**, 668 (1991).

[40] F. J. Giessibl, *A direct method to calculate tip–sample forces from frequency shifts in frequency-modulation atomic force microscopy*, Applied Physics Letters **78**, 123 (2001).

[41] J. Welker, E. Illek, and F. J. Giessibl, *Analysis of force-deconvolution methods in frequency-modulation atomic force microscopy*, Beilstein Journal of Nanotechnology **3**, 238 (2012).

[42] F. J. Giessibl, H. Bielefeldt, S. Hembacher, and J. Mannhart, *Calculation of the optimal imaging parameters for frequency modulation atomic force microscopy*, Applied Surface Science **140**, 352 (1999).

[43] G. Binnig, H. Rohrer, C. Gerber, and E. Weibel, *Surface studies by scanning tunneling microscopy*, Physical Review Letters **49**, 57 (1982).

[44] C. J. Chen, *Introduction to scanning tunneling microscopy*, Oxford University Press, New York (1993).

[45] R. Wiesendanger, *Scanning probe microscopy and spectroscopy: methods and applications*, Cambridge University Press, Cambridge (1994).

[46] G. Binnig, H. Rohrer, C. Gerber, and E. Weibel, *Tunneling through a controllable vacuum gap*, Applied Physics Letters **40**, 178 (1982).

[47] P. O. Gartland and B. J. Slagsvold, *Transitions conserving parallel momentum in photoemission from the (111) face of copper*, Physical Review B **12**, 4047 (1975).

[48] J. Bardeen, *Tunnelling from a many-particle point of view*, Physical Review Letters **6**, 57 (1961).

[49] J. Repp, *Rastertunnelmikroskopie und -spektroskopie an Adsorbaten auf Metall- und Isolatoroberflächen*, PhD thesis, Freie Universität Berlin (2002).

[50] M. Ternes, *Scanning tunneling spectroscopy at the single atom scale*, PhD thesis, Technische Universität Berlin (2006).

[51] K. Bladh, D. Gunnarsson, E. Hürfeld, S. Devi, C. Kristoffersson, B. Smålander, S. Pehrson, T. Claeson, P. Delsing, and M. Taslakov, *Comparison of cryogenic filters for use in single electronics experiments*, Review of Scientific Instruments **74**, 1323 (2003).

[52] H. le Sueur and P. Joyez, *Microfabricated electromagnetic filters for millikelvin experiments*, Review of Scientific Instruments **77**, 115102 (2006).

[53] M. Assig, M. Etzkorn, A. Enders, W. Stiepany, C. R. Ast, and K. Kern, *A 10 mK scanning tunneling microscope operating in ultra high vacuum and high magnetic fields*, Review of Scientific Instruments **84**, 033903 (2013).

[54] A. Peronio, N. Okabayashi, F. Griesbeck, and F. Giessibl, *Radio frequency filter for an enhanced resolution of inelastic electron tunneling spectroscopy in a combined scanning tunneling- and atomic force microscope*, Review of Scientific Instruments **90**, 123104 (2019).

[55] J. B. Johnson, *Thermal agitation of electricity in conductors*, Physical Review **32**, 97 (1928).

[56] J. Barry, E. Lee, and D. Messerschmitt, *Digital communication*, Springer New York, New York (2004).

[57] J. Kim, G. A. Fiete, H. Nam, A. H. MacDonald, and C.-K. Shih, *Universal quenching of the superconducting state of two-dimensional nanosize Pb-island structures*, Physical Review B **84**, 014517 (2011).

[58] C. Poole and I. Darwazeh, *Chapter 14 - Low-noise amplifier design*, in C. Poole and I. Darwazeh (Editors), *Microwave active circuit analysis and design*, p. 475–517, Academic Press, Oxford (2016).

[59] F. J. Giessibl, *High-speed force sensor for force microscopy and profilometry utilizing a quartz tuning fork*, Applied Physics Letters **73**, 3956 (1998).

[60] M. Schelchshorn, F. Stilp, M. Weiss, and F. J. Giessibl, *On the origin and elimination of cross coupling between tunneling current and excitation in scanning probe experiments that utilize the qPlus sensor*, Review of Scientific Instruments **94**, 113704 (2023).

[61] J. Berwanger, *Atom-by-atom assembly and investigation of small Fe clusters with high-resolution atomic force microscopy*, PhD thesis, Universität Regensburg (2019).

[62] B. J. van Wees, H. van Houten, C. W. J. Beenakker, J. G. Williamson, L. P. Kouwenhoven, D. van der Marel, and C. T. Foxon, *Quantized conductance of point contacts in a two-dimensional electron gas*, Physical Review Letters **60**, 848 (1988).

[63] M. Schneiderbauer, M. Emmrich, A. J. Weymouth, and F. J. Giessibl, *CO tip functionalization inverts atomic force microscopy contrast via short-range electrostatic forces*, Physical Review Letters **112**, 166102 (2014).

[64] B. Cordero, V. Gómez, A. E. Platero-Prats, M. Revés, J. Echeverría, E. Cremades, F. Barragán, and S. Alvarez, *Covalent radii revisited*, Dalton Transactions **37**, 2832 (2008).

[65] W. Shockley, *On the surface states associated with a periodic potential*, Physical Review **56**, 317 (1939).

[66] A. Zangwill, *Physics at surfaces*, Cambridge University Press, Cambridge (1988).

[67] T. Fauster, L. Hammer, K. Heinz, and M. A. Schneider, *Oberflächenphysik: Grundlagen und Methoden*, Oldenbourg Verlag, München (2013).

[68] Y. Hasegawa and P. Avouris, *Direct observation of standing wave formation at surface steps using scanning tunneling spectroscopy*, Physical Review Letters **71**, 1071 (1993).

[69] S. D. Kevan, *Evidence for a new broadening mechanism in angle-resolved photoemission from Cu(111)*, Physical Review Letters **50**, 526 (1983).

[70] R. Courths, M. Lau, T. Scheunemann, H. Gollisch, and R. Feder, *From the Shockley surface state on Cu(111) to sp-like surface resonances on $Cu_3Au(111)$*, Physical Review B **63**, 195110 (2001).

[71] F. Forster, G. Nicolay, F. Reinert, D. Ehm, S. Schmidt, and S. Hüfner, *Surface and interface states on adsorbate covered noble metal surfaces*, Surface Science **532-535**, 160 (2003).

[72] P. Hyldgaard and T. L. Einstein, *Surface-state mediated three-adsorbate interaction: electronic nature and nanoscale consequences*, Surface Science **532-535**, 600 (2003).

[73] G. Butti, S. Caravati, G. P. Brivio, M. I. Trioni, and H. Ishida, *Image potential states and electronic structure of Na/Cu(111)*, Physical Review B **72**, 125402 (2005).

[74] G. Hörmandinger, *Imaging of the Cu(111) surface state in scanning tunneling microscopy*, Physical Review B **49**, 13897 (1994).

[75] T. Andreev, I. Barke, and H. Hövel, *Adsorbed rare-gas layers on Au(111): shift of the Shockley surface state studied with ultraviolet photoelectron spectroscopy and scanning tunneling spectroscopy*, Physical Review B **70**, 205426 (2004).

[76] M. P. Everson, R. C. Jaklevic, and W. Shen, *Measurement of the local density of states on a metal surface: scanning tunneling spectroscopic imaging of Au(111)*, Journal of Vacuum Science & Technology A **8**, 3662 (1990).

[77] M. P. Everson, L. C. Davis, R. C. Jaklevic, and W. Shen, *Effects of surface features upon the Au(111) surface state local density of states studied with scanning tunneling spectroscopy*, Journal of Vacuum Science & Technology B **9**, 891 (1991).

[78] L. C. Davis, M. P. Everson, R. C. Jaklevic, and W. Shen, *Theory of the local density of surface states on a metal: comparison with scanning tunneling spectroscopy of a Au(111) surface*, Physical Review B **43**, 3821 (1991).

[79] M. F. Crommie, C. P. Lutz, and D. M. Eigler, *Confinement of electrons to quantum corrals on a metal surface*, Science **262**, 218 (1993).

[80] M. Ternes, C. P. Lutz, C. F. Hirjibehedin, F. J. Giessibl, and A. J. Heinrich, *The force needed to move an atom on a surface*, Science **319**, 1066 (2008).

[81] J. Berwanger, F. Huber, F. Stilp, and F. J. Giessibl, *Lateral manipulation of single iron adatoms by means of combined atomic force and scanning tunneling microscopy using CO-terminated tips*, Physical Review B **98**, 195409 (2018).

[82] S. E. Freeney, S. T. P. Borman, J. W. Harteveld, and I. Swart, *Coupling quantum corrals to form artificial molecules*, SciPost Physics **9**, 085 (2020).

[83] W. Jolie, T.-C. Hung, L. Niggli, B. Verlhac, N. Hauptmann, D. Wegner, and A. A. Khajetoorians, *Creating tunable quantum corrals on a Rashba surface alloy*, ACS Nano **16**, 4876 (2022).

[84] J. Fuchs, *Bau eines Quantum Corrals aus CO Molekülen*, Bachelor thesis, Universität Regensburg (2020).

[85] L. Bartels, G. Meyer, and K.-H. Rieder, *Basic steps of lateral manipulation of single atoms and diatomic clusters with a scanning tunneling microscope tip*, Physical Review Letters **79**, 697 (1997).

[86] B. A. McDougall, T. Balasubramanian, and E. Jensen, *Phonon contribution to quasiparticle lifetimes in Cu measured by angle-resolved photoemission*, Physical Review B **51**, 13891(R) (1995).

[87] J. Li, W.-D. Schneider, R. Berndt, O. R. Bryant, and S. Crampin, *Surface-state lifetime measured by scanning tunneling spectroscopy*, Physical Review Letters **81**, 4464 (1998).

[88] L. Bürgi, O. Jeandupeux, H. Brune, and K. Kern, *Probing hot-electron dynamics at surfaces with a cold scanning tunneling microscope*, Physical Review Letters **82**, 4516 (1999).

[89] P. M. Echenique, J. Osma, M. Machado, V. M. Silkin, E. V. Chulkov, and J. M. Pitarke, *Surface-state electron dynamics in noble metals*, Progress in Surface Science **67**, 271 (2001).

[90] A. Fukui, H. Kasai, and A. Okiji, *Many-body effects on the lifetime of Shockley states on metal surfaces*, Surface Science **493**, 671 (2001).

[91] A. Eiguren, B. Hellsing, F. Reinert, G. Nicolay, E. V. Chulkov, V. M. Silkin, S. Hüfner, and P. M. Echenique, *Role of bulk and surface phonons in the decay of metal surface states*, Physical Review Letters **88**, 066805 (2002).

[92] B. Hellsing, A. Eiguren, and E. V. Chulkov, *Electron-phonon coupling at metal surfaces*, Journal of Physics: Condensed Matter **14**, 5959 (2002).

[93] L. Vitali, P. Wahl, M. A. Schneider, K. Kern, V. M. Silkin, E. V. Chulkov, and P. M. Echenique, *Inter- and intraband inelastic scattering of hot surface state electrons at the Ag(111) surface*, Surface Science **523**, L47 (2003).

[94] M. G. Vergniory, J. M. Pitarke, and S. Crampin, *Lifetimes of Shockley electrons and holes at Cu(111)*, Physical Review B **72**, 193401 (2005).

[95] E. V. Chulkov, A. G. Borisov, J. P. Gauyacq, D. Sánchez-Portal, V. M. Silkin, V. P. Zhukov, and P. M. Echenique, *Electronic excitations in metals and at metal surfaces*, Chemical Reviews **106**, 4160 (2006).

[96] P. Hofmann, I. Y. Sklyadneva, E. D. L. Rienks, and E. V. Chulkov, *Electron–phonon coupling at surfaces and interfaces*, New Journal of Physics **11**, 125005 (2009).

[97] S. Crampin, M. H. Boon, and J. E. Inglesfield, *Influence of bulk states on laterally confined surface state electrons*, Physical Review Letters **73**, 1015 (1994).

[98] R. G. Musket, W. McLean, C. A. Colmenares, D. M. Makowiecki, and W. J. Siekhaus, *Preparation of atomically clean surfaces of selected elements: a review*, Applications of Surface Science **10**, 143 (1982).

[99] J. Naumann, J. Osing, A. Quinn, and I. Shvets, *Morphology of sputtering damage on Cu(111) studied by scanning tunneling microscopy*, Surface Science **388**, 212 (1997).

[100] W. L. Chan and E. Chason, *Making waves: kinetic processes controlling surface evolution during low energy ion sputtering*, Journal of Applied Physics **101**, 121301 (2007).

[101] M. Schneiderbauer, *Aufbau eines Tieftemperatur-Ultrahochvakuum-Rasterkraftmikroskops und Messung elektrischer Multipolkräfte im Piconewton-Bereich*, PhD thesis, University of Regensburg (2014).

[102] M. Emmrich, *Subatomare Auflösung auf Adatomen und kraftfeldabhängige laterale Manipulation mit einem eigenentwickelten Tieftemperatur-Rasterkraftmikroskop*, PhD thesis, University of Regensburg (2015).

[103] R. K. Tiwari, D. M. Otálvaro, C. Joachim, and M. Saeys, *Origin of the contrast inversion in the STM image of CO on Cu(111)*, Surface Science **603**, 3286 (2009).

[104] J. Kessler and F. Thieme, *Chemisorption of CO on differently prepared Cu(111) surfaces*, Surface Science **67**, 405 (1977).

[105] S. Ishi, Y. Ohno, and B. Viswanathan, *An overview on the electronic and vibrational properties of adsorbed CO*, Surface Science **161**, 349 (1985).

[106] M. E. Straumanis and L. S. Yu, *Lattice parameters, densities, expansion coefficients and perfection of structure of Cu and of Cu–In α phase*, Acta Crystallographica Section A **25**, 676 (1969).

[107] T. Hofmann, *Hochauflösende Rasterkraftmikroskopie auf Graphen und Kohlenmonoxid*, PhD thesis, Universität Regensburg (2014).

[108] A. Liebig, *From non-contact to contact – high-precision atomic force microscopy with atomically characterized tips*, PhD thesis, Universität Regensburg (2021).

[109] J. Welker and F. J. Giessibl, *Revealing the angular symmetry of chemical bonds by atomic force microscopy*, Science **336**, 444 (2012).

[110] J. Welker, A. J. Weymouth, and F. J. Giessibl, *The influence of chemical bonding configuration on atomic identification by force spectroscopy*, ACS Nano **7**, 7377 (2013).

[111] L. Gross, F. Mohn, N. Moll, P. Liljeroth, and G. Meyer, *The chemical structure of a molecule resolved by atomic force microscopy*, Science **325**, 1110 (2009).

[112] N. Moll, L. Gross, F. Mohn, A. Curioni, and G. Meyer, *The mechanisms underlying the enhanced resolution of atomic force microscopy with functionalized tips*, New Journal of Physics **12**, 125020 (2010).

[113] N. Pavliček and L. Gross, *Generation, manipulation and characterization of molecules by atomic force microscopy*, Nature Reviews Chemistry **1**, 0005 (2017).

[114] P. Jelínek, *High resolution SPM imaging of organic molecules with functionalized tips*, Journal of Physics: Condensed Matter **29**, 343002 (2017).

[115] L. Gross, F. Mohn, N. Moll, B. Schuler, A. Criado, E. Guitián, D. Peña, A. Gourdon, and G. Meyer, *Bond-order discrimination by atomic force microscopy*, Science **337**, 1326 (2012).

[116] N. Moll, L. Gross, F. Mohn, A. Curioni, and G. Meyer, *A simple model of molecular imaging with noncontact atomic force microscopy*, New Journal of Physics **14**, 083023 (2012).

[117] L. Bartels, G. Meyer, and K.-H. Rieder, *Controlled vertical manipulation of single CO molecules with the scanning tunneling microscope: a route to chemical contrast*, Applied Physics Letters **71**, 213 (1997).

[118] M. Weiss, M. Schelchshorn, F. Stilp, A. J. Weymouth, and F. J. Giessibl, *Increasing the lifetime of confined electronic states in an artificial quantum structure*, Physical Review B **109**, 235422 (2024).

[119] M. Schelchshorn, *Exploring the dominant confining mechanism in quantum corrals on Cu(111) with combined scanning tunneling and atomic force microscopy*, Master thesis, University of Regensburg (2024).

[120] M. Weiss, *Tunnelspektroskopie an einem Kohlenstoffmonoxid-Quantum-Corral*, Master thesis, Universität Regensburg (2021).

[121] T. Kumagai and A. Tamura, *Scanning tunneling spectrum of electrons confined in a rectangular quantum corral*, Journal of Physics: Condensed Matter **21**, 225004 (2009).

[122] S. Mitsuoka and A. Tamura, *STM images and STS for a rectangular quantum corral constructed with δ-function barriers and the effect of an adsorbed atom on STM images and STS*, Physica E: Low-dimensional Systems and Nanostructures **44**, 1410 (2012).

[123] M. Newville *et al.*, *lmfit/lmfit-py 1.0.1*, Zenodo, software, version 1.0.1, DOI: 10.5281/zenodo.3814709 (2020).

[124] P. Wahl, L. Diekhöner, M. A. Schneider, and K. Kern, *Background removal in scanning tunneling spectroscopy of single atoms and molecules on metal surfaces*, Review of Scientific Instruments **79**, 043104 (2008).

[125] J. J. Quinn and R. A. Ferrell, *Electron self-energy approach to correlation in a degenerate electron gas*, Physical Review **112**, 812 (1958).

[126] P. M. Echenique, R. Berndt, E. V. Chulkov, T. Fauster, A. Goldmann, and U. Höfer, *Decay of electronic excitations at metal surfaces*, Surface Science Reports **52**, 219 (2004).

[127] S. Heers, P. Mavropoulos, S. Lounis, R. Zeller, and S. Blügel, *Lifetime reduction of surface states at Cu, Ag, and Au(111) caused by impurity scattering*, Physical Review B **86**, 125444 (2012).

[128] H. Jensen, J. Kröger, R. Berndt, and S. Crampin, *Electron dynamics in vacancy islands: scanning tunneling spectroscopy on Ag(111)*, Physical Review B **71**, 155417 (2005).

[129] S. Crampin and O. R. Bryant, *Fully three-dimensional scattering calculations of standing electron waves in quantum nanostructures: the importance of quasiparticle interactions*, Physical Review B **54**, R17367 (1996).

[130] L. Schneider, K. T. Ton, I. Ioannidis, J. Neuhaus-Steinmetz, T. Posske, R. Wiesendanger, and J. Wiebe, *Proximity superconductivity in atom-by-atom crafted quantum dots*, Nature **621**, 60 (2023).

[131] G. García-Calderón and L. Chaos-Cador, *Theory of coherent and incoherent processes in quantum corrals*, Physical Review B **73**, 195405 (2006).

[132] H. K. Harbury and W. Porod, *Elastic scattering theory for electronic waves in quantum corrals*, Physical Review B **53**, 15455 (1996).

[133] A. I. Rahachou and I. V. Zozoulenko, *Elastic scattering of surface electron waves in quantum corrals: importance of the shape of the adatom potential*, Physical Review B **70**, 233409 (2004).

[134] S. Crampin, *Scanning tunneling spectroscopy of surfaces where surface states dominate*, Journal of Electron Spectroscopy and Related Phenomena **109**, 51 (2000).

[135] J. Kliewer, R. Berndt, and S. Crampin, *Scanning tunnelling spectroscopy of electron resonators*, New Journal of Physics **3**, 22 (2001).

[136] L. Jdira, K. Overgaag, R. Stiufiuc, B. Grandidier, C. Delerue, S. Speller, and D. Vanmaekelbergh, *Linewidth of resonances in scanning tunneling spectroscopy*, Physical Review B **77**, 205308 (2008).

[137] J. Repp, G. Meyer, S. Paavilainen, F. E. Olsson, and M. Persson, *Scanning tunneling spectroscopy of Cl vacancies in NaCl films: strong electron-phonon coupling in double-barrier tunneling junctions*, Physical Review Letters **95**, 225503 (2005).

[138] K. H. Lau and W. Kohn, *Indirect long-range oscillatory interaction between adsorbed atoms*, Surface Science **75**, 69 (1978).

[139] B. Gumhalter and W. Brenig, *Indirect adsorbate-adsorbate interactions mediated by quasi-one-dimensional surface electronic states*, Progress in Surface Science **48**, 39 (1995).

[140] P. Hyldgaard and M. Persson, *Long-ranged adsorbate-adsorbate interactions mediated by a surface-state band*, Journal of Physics: Condensed Matter **12**, L13 (2000).

[141] P. Hyldgaard and T. Einstein, *Surface-state mediated three-adsorbate interaction: exact and numerical results and simple asymptotic expression*, Applied Surface Science **212-213**, 856 (2003).

[142] N. Okabayashi, A. Peronio, M. Paulsson, T. Arai, and F. J. Giessibl, *Vibrations of a molecule in an external force field*, Proceedings of the National Academy of Sciences **115**, 4571 (2018).

[143] R. Rejali, L. Farinacci, D. Coffey, R. Broekhoven, J. Gobeil, Y. M. Blanter, and S. Otte, *Confined vacuum resonances as artificial atoms with tunable lifetime*, ACS Nano **16**, 11251 (2022).

[144] J. Fernández, M. Moro-Lagares, D. Serrate, and A. A. Aligia, *Manipulation of the surface density of states of Ag(111) by means of resonators: experiment and theory*, Physical Review B **94**, 075408 (2016).

[145] M. Weiss, F. Stilp, M. Reinhart, and F. J. Giessibl, *Measurement and qualitative explanation of decay lengths of attractive and repulsive forces between natural and artificial atoms*, Physical Review B **112**, 205413 (2025).

[146] B. Schuler, W. Liu, A. Tkatchenko, N. Moll, G. Meyer, A. Mistry, D. Fox, and L. Gross, *Adsorption geometry determination of single molecules by atomic force microscopy*, Physical Review Letters **111**, 106103 (2013).

[147] H. Bekhouche, D. Rahou, A. Gueddim, M. K. Abdelhafidi, and N. Bouarissa, *Electron states, effective masses and transverse effective charge of InAs quantum dots*, Optical and Quantum Electronics **50**, 309 (2018).

[148] A. J. Weymouth, T. Hofmann, and F. J. Giessibl, *Quantifying molecular stiffness and interaction with lateral force microscopy*, Science **343**, 1120 (2014).

[149] Y. S. Kim, S. K. Kim, and W. D. Lee, *Dependence of the closed-shell repulsive interaction on the overlap of the electron densities*, Chemical Physics Letters **80**, 574 (1981).

[150] M. Ellner, P. Pou, and R. Pérez, *Molecular identification, bond order discrimination, and apparent intermolecular features in atomic force microscopy studied with a charge density based method*, ACS Nano **13**, 786 (2019).

[151] A. Liebig, P. Hapala, A. J. Weymouth, and F. J. Giessibl, *Quantifying the evolution of atomic interaction of a complex surface with a functionalized atomic force microscopy tip*, Scientific Reports **10**, 14104 (2020).

[152] J. C. Slater, *Atomic shielding constants*, Physical Review **36**, 57 (1930).

[153] G. Baym, *Lectures on quantum mechanics*, W. A. Benjamin, New York (1969).

[154] N. D. Lang, *Apparent barrier height in scanning tunneling microscopy*, Physical Review B **37**, 10395 (1988).

[155] M. Ternes, C. González, C. P. Lutz, P. Hapala, F. J. Giessibl, P. Jelínek, and A. J. Heinrich, *Interplay of conductance, force, and structural change in metallic point contacts*, Physical Review Letters **106**, 016802 (2011).

[156] P. Jelínek, M. Ondráček, and F. Flores, *Relation between the chemical force and the tunnelling current in atomic point contacts: a simple model*, Journal of Physics: Condensed Matter **24**, 084001 (2012).

[157] S. Nordholm and G. B. Bacskay, *The basics of covalent bonding in terms of energy and dynamics*, Molecules **25**, 2667 (2020).

[158] A. Gustafsson, N. Okabayashi, A. Peronio, F. J. Giessibl, and M. Paulsson, *Analysis of STM images with pure and CO-functionalized tips: a first-principles and experimental study*, Physical Review B **96**, 085415 (2017).

[159] J. Tersoff and D. R. Hamann, *Theory of the scanning tunneling microscope*, Physical Review B **31**, 805 (1985).

[160] A. Bereczuk, *Universal HOM-type S-matrix correlations in chaotic (non-)trivial topological insulators and an improved model for the AFM and STM characteristics in Cu-based quantum corrals*, PhD thesis, University of Regensburg (2023).

[161] P. M. Morse, *Diatomic molecules according to the wave mechanics. II. Vibrational levels*, Physical Review **34**, 57 (1929).

[162] A. Mirzanejad and S. A. Varganov, *Derivation of Morse potential*, Molecular Physics **123**, e2360542 (2025).

[163] G. Rubio-Bollinger, P. Joyez, and N. Agraït, *Metallic adhesion in atomic-size junctions*, Physical Review Letters **93**, 116803 (2004).

[164] H. Inouye and S. Kita, *Experimental determination of the repulsive potentials between K^+ ions and rare-gas atoms*, The Journal of Chemical Physics **56**, 4877 (1972).

[165] H. Inouye and S. Kita, *Elastic scattering of Li^+ ions in helium*, The Journal of Chemical Physics **57**, 1301 (1972).

[166] H. Inouye and S. Kita, *Experimental determination of repulsive potentials between alkali ions (Li^+, K^+, and Cs^+) and hydrogen molecules (H_2 and D_2)*, The Journal of Chemical Physics **59**, 6656 (1973).

[167] S. Kita, K. Noda, and H. Inouye, *Experimental determination of repulsive potentials between alkali ions (Li^+, Na^+, and K^+) and N_2 and CO molecules*, Chemical Physics **7**, 156 (1975).

[168] S. Kita, K. Noda, and H. Inouye, *Repulsive potentials for Cl–R and Br–R (R=He, Ne, and Ar) derived from beam experiments*, The Journal of Chemical Physics **64**, 3446 (1976).

[169] H. Inouye, K. Noda, and S. Kita, *Repulsive potentials derived from beam scattering of Rb^+ and Cs^+ ions by rare gas atoms*, The Journal of Chemical Physics **71**, 2135 (1979).

[170] X. Guo, Z. Fang, A. S. Kheifets, S. A. Canney, M. Vos, I. E. McCarthy, and E. Weigold, *Spectral momentum density of electrons in copper*, Physical Review B **57**, 6333 (1998).

[171] D.-H. Lim, J. H. Jo, D. Y. Shin, J. Wilcox, H. C. Ham, and S. W. Nam, *Carbon dioxide conversion into hydrocarbon fuels on defective graphene-supported Cu nanoparticles from first principles*, Nanoscale **6**, 5087 (2014).

[172] A. Jedidi, S. Rasul, D. Masih, L. Cavallo, and K. Takanabe, *Generation of Cu–In alloy surfaces from $CuInO_2$ as selective catalytic sites for CO_2 electroreduction*, Journal of Materials Chemistry A **3**, 19085 (2015).

[173] O. Gretz, A. J. Weymouth, and F. J. Giessibl, *Identifying the atomic configuration of the tip apex using STM and frequency-modulation AFM with CO on Pt(111)*, Physical Review Research **2**, 033094 (2020).

[174] C. Nordling, E. Sokolowski, and K. Siegbahn, *Precision method for obtaining absolute values of atomic binding energies*, Physical Review **105**, 1676 (1957).

[175] M. Li, J.-Y. Zhang, Y. Zhang, and T.-M. Wang, *A density functional theory study on the adsorption of CO and O_2 on Cu-terminated $Cu_2O(111)$ surface*, Chinese Physics B **21**, 067302 (2012).

[176] S. Saini, J. Halldin Stenlid, and F. Abild-Pedersen, *Electronic structure factors and the importance of adsorbate effects in chemisorption on surface alloys*, npj Computational Materials **8**, 163 (2022).

[177] X. Wang, L. Andrews, S. Riedel, and M. Kaupp, *Mercury is a transition metal: the first experimental evidence for HgF_4*, Angewandte Chemie International Edition **46**, 8371 (2007).

[178] A. Y. Rogachev, M. Miao, G. Merino, and R. Hoffmann, *Molecular CsF_5 and CsF_2^+*, Angewandte Chemie **127**, 8393 (2015).

[179] P. F. Walch and D. E. Ellis, *Effects of secondary ligands on the electronic structure of uranyls*, Journal of Chemical Physics **65**, 2387 (1976).

[180] K. Tatsumi and R. Hoffmann, *Bent cis d^0 MoO_2^{2+} vs. linear trans d^0f^0 UO_2^{2+}: a significant role for nonvalence 6p orbitals in uranyl*, Inorganic Chemistry **19**, 2656 (1980).

[181] P. Pyykkö, N. Runeberg, M. Straka, and K. G. Dyall, *Could uranium(XII)hexoxide, UO_6 (O_h) exist?*, Chemical Physics Letters **328**, 415 (2000).

[182] V. G. Orlov and G. S. Sergeev, *Electronic band structure and chemical bonding in trigonal Se and Te*, AIP Advances **12**, 055110 (2022).

[183] H. B. Michaelson, *The work function of the elements and its periodicity*, Journal of Applied Physics **48**, 4729 (1977).

[184] F. Reinert, G. Nicolay, S. Schmidt, D. Ehm, and S. Hüfner, *Direct measurements of the L-gap surface states on the (111) face of noble metals by photoelectron spectroscopy*, Physical Review B **63**, 115415 (2001).

[185] P. T. Sprunger, L. Petersen, E. W. Plummer, E. Lægsgaard, and F. Besenbacher, *Giant Friedel oscillations on the beryllium(0001) surface*, Science **275**, 1764 (1997).

[186] U. O. Karlsson, S. A. Flodström, R. Engelhardt, W. Gädeke, and E. E. Koch, *Intrinsic surface state on Be(0001)*, Solid State Communications **49**, 711 (1984).

[187] J. Lee, D. Wong, J. Velasco, J. F. Rodriguez-Nieva, S. Kahn, H. Z. Tsai, T. Taniguchi, K. Watanabe, A. Zettl, F. Wang, L. S. Levitov, and M. F. Crommie, *Imaging electrostatically confined Dirac fermions in graphene quantum dots*, Nature Physics **12**, 1032 (2016).

[188] M. Chen, Y.-P. Jiang, J. Peng, H. Zhang, C.-Z. Chang, X. Feng, Z. Fu, F. Zheng, P. Zhang, L. Wang, K. He, X.-C. Ma, and Q.-K. Xue, *Selective trapping of hexagonally warped topological surface states in a triangular quantum corral*, Science Advances **5**, eaaw3988 (2019).

[189] H. Mönig, D. R. Hermoso, O. Díaz Arado, M. Todorović, A. Timmer, S. Schüer, G. Langewisch, R. Pérez, and H. Fuchs, *Submolecular imaging by noncontact atomic force microscopy with an oxygen atom rigidly connected to a metallic probe*, ACS Nano **10**, 1201 (2016).

[190] H. Mönig, S. Amirjalayer, A. Timmer, Z. Hu, L. Liu, O. Díaz Arado, M. Cnudde, C. A. Strassert, W. Ji, M. Rohlfing, and H. Fuchs, *Quantitative assessment of intermolecular interactions by atomic force microscopy imaging using copper oxide tips*, Nature Nanotechnology **13**, 371 (2018).

[191] D. M. Eigler, C. P. Lutz, and W. E. Rudge, *An atomic switch realized with the scanning tunnelling microscope*, Nature **352**, 600 (1991).

[192] B. Neu, G. Meyer, and K.-H. Rieder, *Controlled vertical and lateral manipulation of single atoms and molecules with the scanning tunneling microscope*, Modern Physics Letters B **9**, 963 (1995).

[193] B. Verlhac, N. Bachellier, L. Garnier, M. Ormaza, P. Abufager, R. Robles, M.-L. Bocquet, M. Ternes, N. Lorente, and L. Limot, *Atomic-scale spin sensing with a single molecule at the apex of a scanning tunneling microscope*, Science **366**, 623 (2019).

[194] R. Wiesendanger, H.-J. Güntherodt, G. Güntherodt, R. J. Gambino, and R. Ruf, *Observation of vacuum tunneling of spin-polarized electrons with the scanning tunneling microscope*, Physical Review Letters **65**, 247 (1990).

[195] M. Bode, *Spin-polarized scanning tunnelling microscopy*, Reports on Progress in Physics **66**, 523 (2003).

Acknowledgments

First of all, I would like to thank my supervisor Prof. Dr. Franz J. Giessibl for giving me the opportunity to carry out my PhD in his group and to work on fundamental research in scanning probe microscopy. I am grateful for the scientific freedom I had in pursuing my projects and for the discussions and support I received throughout my time in the group.
I would especially like to thank Alfred J. Weymouth. His support throughout my PhD was invaluable. Whenever questions, problems, or new ideas came up, he was always approachable and willing to help. I benefited greatly from his experience, his advice, and his readiness to discuss both scientific and practical issues at any time.
I am equally grateful to Fabian Stilp. Over the course of my PhD, he was an exceptionally important colleague and discussion partner. Our close collaboration, the many scientific discussions, and the fact that we often approached problems from different angles contributed greatly to the quality of my work. Working with him shaped my scientific thinking in many ways.
I would also like to thank my fellow PhD students Adrian Weindl, Christoph Setescak, Shinjae Nam, Sophia Schweiss, and Furkan Özyigit for many helpful discussions, useful suggestions, and valuable feedback on my research.
Very special thanks go to Michael Schelchshorn. He accompanied my work over many years, from his first research project through his bachelor's thesis, another research project, and finally his master's thesis. His work laid much of the foundation for Chapter 5 of this thesis. At the same time, supervising him and discussing quantum corrals and his results with him significantly deepened my own understanding of the subject.
I am also very grateful to the students Jakob Fuchs, Michael Rössner, and Max Reinhart, whom I had the pleasure of supervising during my PhD. Their work on quantum corrals formed an important foundation on which my own research was built. Without their contributions, several of the results presented in this thesis would not have been possible.
Likewise, I would like to thank Maximilian Krüger, Hendrik Weinert, Nicolas Wirth, Mia Fürst, Luis Vendolsky, and Michelle Wölfinger. Through their work on single-

atom measurements and many discussions, my understanding of this field grew substantially. Their contributions were important for developing the ideas that later led to my work on the electrostatic interaction of individual Gd, Ho, and Fe adatoms.
I would also like to thank Ferdinand Huber, Julian Berwanger, Korbinian Pürckhauer, and Alexander Liebig. I benefited enormously from their experience, especially during the early phase of my PhD. Their support made it much easier for me to get started in the lab and in scientific work. I am also grateful to Andrea Auer, whose advice was particularly valuable to me, especially when it came to structuring and writing a scientific paper.
Finally, I would like to thank the people outside academia who supported me throughout these years, especially my family and those who have, over time, become like family to me: Katharina Wagner, Andreas Liebl, Katrin Eichinger, Liane Weiß, Günter Weiß, Astrid Weiß, Michael Weiß, Brigitte Weiß, Herta Langhammer, and Lukas Bombik. Their encouragement, patience, and steady support helped me through the many ups and downs of the PhD years. For that, I am deeply grateful.

In this spirit, I would like to end with the words of Sir Isaac Newton:[1]

"If I have seen further, it is by standing on the shoulders of giants."

[1] H. W. Turnbull (ed.), *The Correspondence of Isaac Newton: 1661–1675*, Vol. 1 (London: Published for the Royal Society at the University Press, 1959), p. 416